THE UNIVERSITY *of* EDINBURGH

Transport, selectivity and antifouling in nanoscale membranes

Sritay Mistry

Doctor of Philosophy

THE UNIVERSITY OF EDINBURGH

2022

Abstract

Desalination of seawater has been pursued since ancient times, first being recorded around 300 BC, largely to provide drinking water in ocean-going vessels. The primitive means used then depended on distilling seawater, which is an energy intensive process. In the late 1950s, reverse osmosis (RO) was demonstrated to be capable of desalinating seawater without vaporizing it. RO accounts for nearly 60% of all major desalination plants in operation today due to its lower energy consumption. The need for freshwater, however, has increased significantly in the last few decades, in towns and cities where populations have grown and water bodies diminished. Despite lower energy consumption, RO remains too energy-intensive to supply fresh water at city-scale cheaply, driving research into new RO membranes that can reduce energy consumption. A large number of new nanomaterials have emerged as a result, including carbon nanotubes (CNTs), boron nitride nanotubes (BNNTs), metal-organic framework (MOF) and zeolite membranes. These materials promise very high water permeance and salt rejection, which is expected to drive down desalination costs.

Among these materials, CNTs have been considered the forerunner, promising orders of magnitude higher water permeance compared to traditional membranes. Simulations showed BNNTs could potentially provide higher permeance, but manufacturing difficulties prevented much experimental research on BNNTs. These have been recently overcome, and BNNTs once again appear as a promising membrane candidate. Molecular dynamics (MD) based simulation studies of BNNTs, however, present a few discrepancies. While some earlier studies showed permeance higher than CNTs, later studies showed CNTs had higher permeance than BNNTs. In this thesis, the analysis of the membrane transport resistance allowed the resolution of this discrepancy. Simulations studies were found to be largely conducted by modelling membranes having short nanotube lengths, where the flow resistance due to effects at the entrance and exit of the nanotubes dominates, hiding the behaviour inside the nanotubes. As the nanotube lengths are increased, the transport resistance within the nanotubes starts to increase, and in this regime, CNTs are found to have a lower transport resistance compared to BNNTs. The transport resistance within BNNTs is also found to be largely dependent on the partial charge chosen for the BN atoms in the simulation. Experimental evidence concurred with the higher resistance for BNNTs, supporting the hypothesis of a high partial charge on BN atoms, which is known to retard water flow.

The high partial charge of BNNTs, while reducing water flow, provides BNNT membranes with the advantage of high selectivity. Traditional RO membranes are already operating near the thermodynamic limit of energy utilisation, indicating massive increases in permeability is unlikely to drive down energy use, and therefore costs. Instead, high selectivity is one avenue

that could reduce the cost of post-treatment, where clean water from the RO membrane needs to undergo additional steps due to the inability of the membrane to selectively remove solutes. These include boron removal from desalinated seawater, and remineralization of drinking water to make up for essential minerals removed by the membrane. BNNT membranes in water have a charged surface, allowing the membrane to discriminate between cations and anions and repel anions. In this thesis, using both simulations and experiments, this charge-based rejection was shown to work alongside the size-based rejection of traditional membranes where particles are only rejected because they are too large for the membrane pores. As a result, BNNT membranes could be manufactured with larger pores, allowing up to 70% higher water flow rates for comparable rejection with reference to CNTs.

The second avenue where cost reductions may be found lie in membrane cleaning. Membrane fouling and cleaning costs could nearly equal the energy costs and also result in reduced membrane life. The dominant method of membrane cleaning is through the use of chemicals, which requires the desalination plant to be put offline and creates a chemical-laden wastewater disposal problem. Chemical cleaning is therefore done infrequently, while foulant build-up on membranes is a continuous process. Physical methods of cleaning, such as by heating the membrane, appear promising and can be applied frequently without stopping the desalination process. Heating has been shown to act through biological means (by denaturing proteins) and physical means (causing shear flows and vapour expansion within pores), promising cleaning ability against a wide range of foulants. In this thesis, direct heating of membranes was found to be capable of removing nanoparticles from the membrane surface. Heating was shown to work through a mixture of bubble formation and increased Brownian motion of the nanoparticle to displace it away from the membrane surface. The large role played by Brownian forces, however, prevents a deterministic prediction of whether a particle will be removed or not when heat is applied to the surface.

This work therefore deals with the three avenues of improvement in filtration and desalination membranes, i.e., permeability, selectivity and antifouling. This work resolves the question of permeability in BNNT membranes, established charge based rejection in BNNTs as the basis of a membrane capable of high selectivity and finally explores membrane heating as a promising candidate mechanism for the cleaning of membranes.

Lay Summary

Climate change, pollution and population explosion are now leading to a freshwater crisis. Freshwater is necessary for drinking, agriculture and industry, and accounts for only 2.5% of the total water on Earth. Seawater accounts for the remaining 97%, but contains large quantities of dissolved salts. Removing the salts through desalination can convert seawater to freshwater, but desalination is a very energy-intensive process. The most energy-efficient way of desalinating seawater is by forcing it under pressure through membranes that contain very small pores. These small pores block the salt molecules from passing through, producing freshwater in the process.

Forcing water through such membranes with very small pores requires a large amount of energy. Nearly half of the operating costs of a desalination plant go into supplying the energy for pressurising water to force it through the membrane. New membrane materials, such as carbon and boron nitride nanotubes (CNTs and BNNTs, respectively) provide very little friction to the flow of water and are predicted to bring down energy costs. BNNTs have been difficult to fabricate in a laboratory setting and little was known about their real properties. Simulation-based studies have been contradictory, with some showing BNNTs providing lower friction than CNTs, and others the opposite. Using a combination of simulations and experiments, this study shows that the contradictory results arise due to the very short membranes simulated in the previous studies. BNNTs also differ from CNTs in one important aspect - the atoms which make up the BNNT carry electric charges. This makes BNNTs able to repel particles carrying a similar electrical charge. The advantage the charges provides is that the water no longer needs to be forced through very small pores to desalinate it. Larger pores can be used in membranes, and salt particles can be removed with the aid of the electrical repulsion provided by BNNTs. This was shown in this study, again using both simulations and experiments. BNNTs were found to provide up to 70% higher water flow compared to CNTs for the same amount of salt rejection, due to the 30% larger pore size made possible by the use of electrical repulsion.

Forcing saltwater through membranes deposits the salts on it, particularly if there is insufficient flow near the surface. This deposition of salts and other particles reduces membrane performance and may block the whole membrane. Cleaning of membranes is usually done using harsh chemicals, which need the desalination process to be stopped. This cannot be done frequently, while deposition of particles on the membrane is continuous. This study explores the feasibility of heating the membrane to remove nanoscale particles stuck to the membrane surface. Heating as a cleaning mechanism can be applied frequently without the need to stop the desalination process. It is shown to be able to remove stuck particles, but not in a very predictable manner, therefore requiring further study.

Acknowledgements

I would like to thank my supervisors, Matthew and Rohit, for the continuous support throughout my PhD. I am grateful for the weekly meetings, which provided a ground to sound out new research ideas big and small and give course correction when things got too ambitious. I am thankful for the structure they provided to my PhD, which turned it into an immensely beneficial learning experience in conducting scientific research.

I am indebted to Jason, for inviting me to join this group, and for his help with my application. I am grateful to the Commonwealth Scholarship Commission in the UK for granting me a scholarship to pursue this PhD. I am grateful to Livio for the help and discussions on the topic of fluid slip, which proved very useful across a majority of the works in this thesis. I am also grateful to Serena and Davide from the University of Bath, who provided the experimental data to back up the findings from simulations. This helped greatly in improving the thoroughness of my research.

Finally, I would like to thank my family and close friends for their support through my years of study. Much of this work was carried out during the COVID-19 pandemic, and their help and support was essential to maintain my mental health and finish this work.

List of publications

The work presented in this thesis was disseminated in the following journal articles and conferences:

- Mistry, S., Pillai, R., Mattia, D., and Borg, M. K. "Untangling the physics of water transport in boron nitride nanotubes". *Nanoscale*, 13(43):18096-18102, 2021. **[Chapter 4]**
- Mistry, S., Pillai, R., Mattia, D., and Borg, M. K. "Water transport in boron nitride nanotube membranes". *Proceedings of Micro and Nano Flows 2021*, Imperial College, London. **[Chapter 4]**
- Casanova S., Mistry, S., Mazinani, S., Borg, M. K., Chew, Y. M., and Mattia, D. "Enhanced nanoparticle rejection in aligned boron nitride nanotube membranes". *Nanoscale*, 12(41):21138-21145, 2020. **[Chapter 5]**

Declaration

I declare that this thesis was composed by myself, that the work contained herein is my own except where explicitly stated otherwise in the text, and that this work has not been submitted for any other degree or professional qualification except as specified.

Sritay Mistry

Contents

Figures and Tables

Figures

Tables

Chapter 1

Introduction

Recorded history shows that humans have pursued desalination, the process of obtaining freshwater from seawater, for more than a millennium. Initially noted by the likes of Aristotle (∼300 BC) as a curiosity (Kalogirou (2005)), small-scale desalination has been reported repeatedly since then. The advent of intercontinental trade saw an increased need for freshwater in ocean-going vessels, resulting in desalination no longer remaining a curiosity and instead having a practical utility. The birth of the steam engine, which needed fresh water for its boilers, and the rapid expansion of new colonies in the 1800s provided the next necessary impetus for the sustained interest in and development of desalination technologies. This era, up to the early 1900s, gave rise to multiple desalination technologies, such as solar distillation, multi-effect distillation, vacuum distillation and vapour-compression distillation. These technologies primarily evaporated seawater for desalination, and great efforts were put into finding ways to reduce the energy needed for vapourising seawater. Water has a high latent heat of evaporation, at 2500 kJ/kg. Distillation processes requiring vapourising seawater are therefore quite energy-intensive unless the waste heat can be recovered efficiently. However, the advent of membrane-based desalination, especially reverse osmosis (RO) in the 1950s and 60s (Loeb (1981)) effectively did away with the need to turn water to vapour to remove salts. RO processes, therefore, dominate the desalination landscape today, making up 60–65% of all installed desalination facilities (Burn *et al.* (2015); Darre and Toor (2018)). Solar distillation might prove to be competitive from an energy standpoint, though made unappealing for large scale applications by the extremely low flow rates produced (Manchanda and Kumar (2015)).

With the turn of the 21st century, as the challenges of climate change, pollution and over-population effectively squeeze the scarce freshwater resources, the need for freshwater has never been higher. The dominance of RO for desalination has led to a multifaceted effort at increasing the energy efficiency of RO membranes, using both novel, high permeability membrane materials and attempts to recover the energy spent in the desalination process (Lee *et al.* (2011); Shenvi *et al.* (2015); Subramani *et al.* (2011)). Several new membrane materials have emerged, including nanotube and nanoporous membranes, membranes that mimic aquaporins and metal-organic framework (MOF) based membranes, among others (Subramani and Jacangelo (2015); Teow and Mohammad (2019); Werber *et al.* (2016a); Yang *et al.* (2018)), which promise high permeability, selectivity and antifouling properties. Chief among them are

carbon nanotube (CNT) membranes, which have appeared as the leading candidate for the next generation of desalination membranes since their discovery in 1991 (Iijima (1991)). Despite their hydrophobicity, water permeation through small-diameter CNTs was found to be much higher than that predicted by classical theory (Corry (2008); Holt *et al.* (2006); Majumder *et al.* (2005)). This opened up the possibility of forming membranes with aligned CNTs (Hinds *et al.* (2004)) which have high water permeation rates (due to their low surface friction) while maintaining high rates of salt rejection (due to the comparable size ratio between contaminants and nanotube diameter). Alongside CNTs, Boron nitride nanotubes (BNNTs) have also been found to provide similar properties of water permeation as CNTs (Suk *et al.* (2008); Won and Aluru (2007)). Manufacturing difficulties that hindered research on BNNTs have been recently overcome in this research, opening up a further promising material for desalination membranes (Casanova *et al.* (2020b)).

Ostensibly, the focus on increasing permeability by using materials like CNTs was largely to minimize energy usage, thereby reducing operating costs. High permeability may even result in a reduction of the initial capital cost due to a reduction in the size and number of pressure vessels required. High permeability alone, however, does not significantly reduce the running energy costs of the membrane, which forms a principal part of the total costs of desalinating seawater (Cohen-Tanugi *et al.* (2014); Subramani *et al.* (2011)). A review from 2011 (Elimelech and Phillip (2011)) showed that current membrane technology using thin-film composites (TFCs) had already brought the energy consumption down to 1.8 kWh/m^3, close to the theoretical thermodynamic limit of 1.06 kWh/m^3 for seawater desalination at 50% recovery. These two observations, i.e., the current energy requirements are close to the theoretical limit, and very high improvements in permeability produce only a slight decrease in energy requirements, indicate that while efforts to reduce the energy consumption of RO membranes through new high permeability membranes might yet be valuable, significant energy (and therefore cost) reductions are unlikely to be achieved through new membranes alone.

The process of desalination using RO involves multiple steps, starting with the intake of water from a water body, followed by pre-treatment, filtration through the RO membrane, post-treatment and any number of energy recovery devices that might interconnect these stages in parallel. As the RO filtration part of this desalination process nears theoretical limits on energy consumption, further energy reduction may be found in the pre and post-treatment stages. The need for pre-and post-treatment arises largely due to the novelty of foulants found in different water bodies, and the inability of general RO membranes to deal with all of them. Certain foulants, such as chlorine, might chemically attack the membrane (Gohil and Suresh (2017)), requiring pre-treatment to extend the membrane life, while other foulants such as boron might pass through the membrane, requiring post-treatment (Werber *et al.* (2016a)). This brings forward two mitigation strategies to reduce the pre-and post-treatment stages: through antifouling mechanisms and enhanced particle selectivity, respectively.

To this end of reducing desalination costs, Werber *et al.* (2016a) specifically recommends a focus on species selectivity, and not increased permeability as the means to reduce costs of producing desalinated water. High species selectivity could allow essential minerals to pass through filtration membranes used for producing drinking water, avoiding re-mineralization (Epsztein *et al.* (2020)). The poor performance of TFC membranes in removing boron and small disinfectant particles from water are examples where high species selectivity could mitigate the need for expensive post-treatment technologies (Werber *et al.* (2016a)). Methods to improve the selectivity of membranes include modifying the charges on the membrane (Cheng *et al.* (2018); De Grooth *et al.* (2014); Rana *et al.* (2014)), fine-tuning the membrane pore size (Azamat and Khataee (2016)), and modifying the membrane with functional groups (Chogani *et al.* (2020); Gupta *et al.* (2015); Roy *et al.* (2014)). BNNTs acquire special importance when high selectivity becomes a desirable characteristic, primarily due to the presence of partial charges on the atoms of the nanotube (Casanova *et al.* (2020a)). This opens up an additional mechanism for the rejection of charged particles and allows species selectivity based on particle charges. The charged nature of BNNTs also improves their antifouling capabilities (Low *et al.* (2018)), the implications of which are discussed in this work. The combination of high permeability, selectivity and antifouling properties make BNNTs a very promising membrane candidate. However, despite more than a decade since their recognition as a viable candidate for desalination membranes, many fundamental questions about BNNTs remained unanswered. These range from the very basic questions such as whether BNNTs can allow a higher water flux compared to CNTs, to more complex ones, such as about rejection characteristics and mechanisms of a BNNT membrane. In this study, therefore, the focus is brought onto BNNT membranes to answer the following questions: How much resistance, and in what form, does the BNNT membrane pose to the flow of water? Second, how do the charged surface of the BNNT membrane helps in the rejection of charged particles?

While BNNTs may yet prove to be a solution to the selectivity problem, a second strategy for cost reduction in desalination focusses on fouling of membranes, i.e. the build-up of salts and organic matter on the membrane surface with continued usage, which tends to reduce the water flux down to 3-4% of the initial flux (Mulder (1995)). Such fouling requires extensive pre-treatment steps, and in extreme cases, might require the membrane to be replaced completely. Despite the advanced understanding of the mechanisms of membrane fouling, not much literature exists on the cleaning of membranes (Blanpain-Avet *et al.* (2009)). The preferred method for cleaning fouled membranes remains chemical cleaning, despite their negative effects on the active layer of the membrane (Kang *et al.* (2007)) and the need to completely shut down desalination plants. Much focus is devoted to understanding the mechanisms and improving the efficiency of chemical cleaning (Blanpain-Avet *et al.* (2009); Zsirai *et al.* (2018)). This is despite the possibility of physical methods of cleaning being more efficient (Dana *et al.* (2019); Ebrahim (1994)). A common mechanical cleaning technique is backflushing (Sagiv and Semiat (2010)), either as a stand-alone or in combination with chemical cleaning (Zsirai *et al.* (2018)).

A certain amount of interest also exists in the possibility of using heat as a means of antifouling (Aumeier *et al.* (2018, 2021); Lohaus *et al.* (2020)). Heating as an antifouling mechanism has the distinct advantage of not requiring the filtration process to be stopped, unlike backflushing or chemical cleaning, although the use of heating combined with backflushing has also been shown to be advantageous (Aumeier *et al.* (2018); Peng and Tremblay (2008)). The cleaning of nanoscale particles using membrane heating is a topic that remains largely absent from the literature, despite the promise of uninterrupted filtration. In this work, an investigation is therefore carried out to explore the possibilities and mechanisms of nanoscale cleaning through membrane heating.

To summarise, this work looks into the three most prominent aspects of RO based desalination - *high permeability* through CNTs and BNNTs, *high selectivity* using charged BNNT membranes, and a possible candidate for a nanoscale *antifouling* mechanism using heated membranes. Attempts are made to determine which of BNNT or CNT provide higher permeability, how the charged nature of BNNTs may provide higher species selectivity and finally, how simply heating the filtration membrane may prove to be an effective antifouling technique applicable without the need to stop the desalination process.

1.1 Thesis outline

The remainder of this thesis will cover the following:

Chapter 2 – Background is divided into three parts. The first part looks at previous research on flows through CNT and BNNTs, followed by an overview of particle selection and rejection in membranes, and finally, the state of current membrane antifouling technologies.

Chapter 3 – Methodology introduces molecular dynamics, the primary simulation technique used in this work. The various setups used for the studies of flows through nanotubes, particle selectivity and antifouling studies are presented. The potentials used to model nanoscale systems will also be discussed.

Chapter 4 – Untangling the physics of water transport in boron nitride nanotubes investigates how the use of short membranes, along with the challenges in the modelling of pore entrances of BNNTs in MD simulation studies have led to inconclusive results about the efficiency of BNNTs compared to CNTs. A new framework for making these comparisons, and comparisons across simulations and experiments are presented to resolve the conflicting results.

Chapter 5 – Enhanced nanoparticle rejection in aligned boron nitride nanotube membranes examines how the high zeta potential of BNNTs can be exploited to improve the rejection characteristics of BNNT membranes. The mechanism of particle rejection is discussed,

followed by the implications of improved membrane permeance due to the presence of multiple rejection mechanisms, allowing larger membrane pores than the equivalent CNTs.

Chapter 6 – Nanoscale antifouling using direct membrane heating investigates the aspects of cleaning membranes through an active, mechanical method, namely heating. The feasibility of direct membrane heating as a cleaning method is explored, with a focus on the mechanisms of the foulant-membrane interactions.

Chapter 7 – Summary and Concluding Remarks concludes the main findings of this work, with discussions on the prospect of BNNT membranes in desalination plants and the possible impact of nanoscale cleaning methods in desalination systems. Promising directions for future work are also discussed.

Chapter 2

Background

2.1 Nanotubes

Nanotube structure

Carbon nanotubes (shown in Figure 2.1) were first discovered by Sumio Iijima in 1991 (Iijima (1991)), while he was working on the synthesis of fullerenes. The first nanotubes created ranged between 4 and 30 nm in diameter, with lengths of up to 1 μm, and were multi-walled carbon nanotubes. Single-walled nanotubes were synthesized soon after in 1993 (Bethune *et al.* (1993); Iijima and Ichihashi (1993)). Boron Nitride nanotubes were theorized to exist as stable structures in 1993-94 (Hamilton *et al.* (1993); Rubio *et al.* (1994)) and synthesized a year later in 1995 (Chopra *et al.* (1995)).

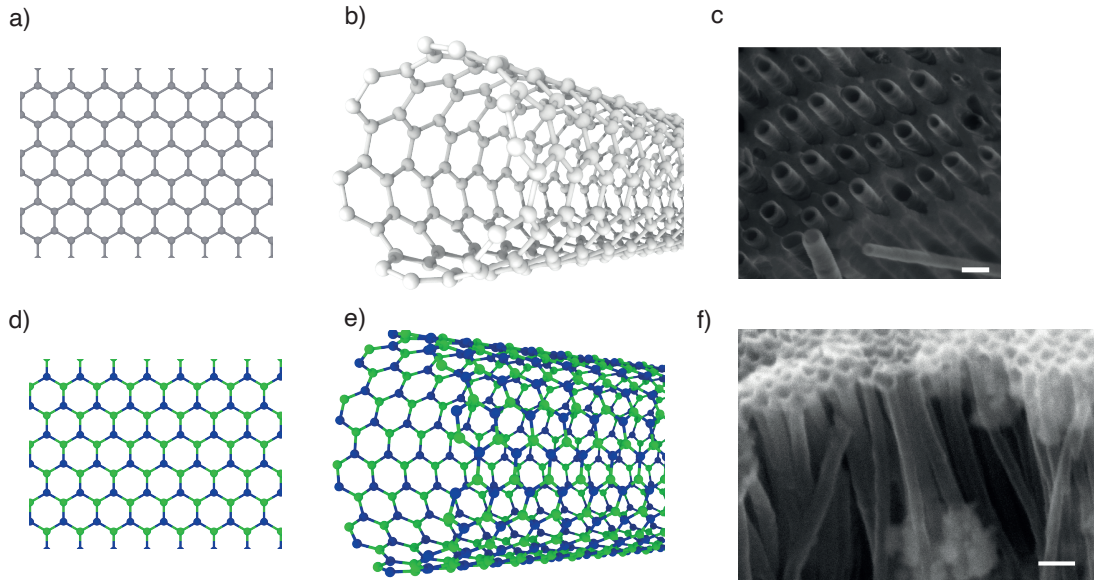

Figure 2.1: (a) Molecular structure of graphene. (b) Molecular structure of a single walled CNT. (c) SEM image of CNTs stacked in a membrane. The white bar represents 20 nm. Image taken from Mattia *et al.* (2015). (d) Molecular structure of boron nitride. (e) Molecular structure of a single walled BNNT. (f) SEM image of BNNTs stacked in a membrane. Image taken from Casanova *et al.* (2020b). The white bar represents 100 nm.

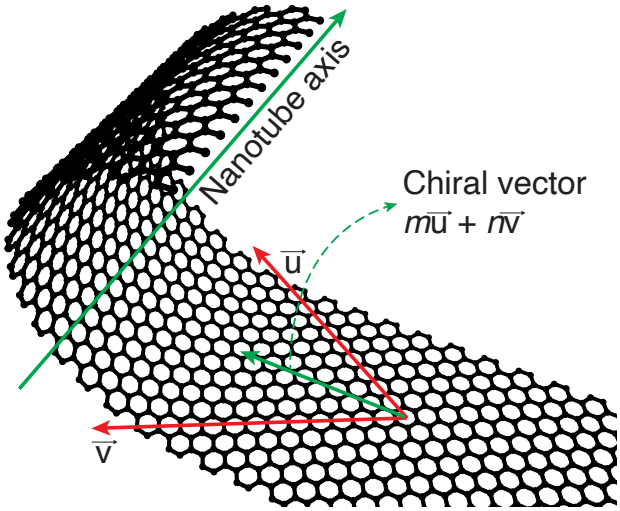

Figure 2.2: Chirality of a nanotube. Shown here is an armchair nanotube with $m = n$.

Carbon nanotubes can be represented as 2-D sheets of graphene, which are rolled up to form a tubular needle-like structure. Nanotubes can be classified based on several parameters such as diameter, chirality and length. The chirality of the nanotube is the angle that the lattice unit of the nanotube makes with the tube axis, and can be thought of as the angle at which rolling a hypothetical graphene sheet would create the given nanotube. The chirality of the nanotube also fixes the diameter of the nanotube, as the lattice unit of graphene has a fixed bond length and does not change much when rolled. The angle at which the sheet is rolled therefore determines the number of lattice units that can fit in the circumference, and therefore, uniquely determines the diameter at each chirality. The chirality of the nanotube is often expressed using the notation (m,n), where m and n stand for the magnitude of the basis vectors $(\vec{u},\vec{v})$ depicted in Figure 2.2. The diameter of the nanotube can be linked to the chiral vectors using the formula :

$$D = \frac{a}{\pi}\sqrt{m^2+n^2+mn} \tag{2.1}$$

where a is the C-C or B-N bond lengths for CNTs and BNNTs, respectively.

Differing nanotube bond lengths

The C-C bond length is kept constant at 1.421 Å, independent of the nanotube diameter. The B-N bond length, however, appears to vary by $\mathcal{O}(10^{-2})$ Å, from 1.43 to 1.46 Å depending on nanotube diameter. This variation was discovered using ab-initio Density Functional Theory (DFT) simulations performed by Ju *et al.* (2011).

Differing nanotube partial charges

Using DFT simulations, Won *et al.* (2006) showed that carbon atoms in CNTs mostly carry a negligible partial charge. They found that for a finite length CNT, the unsaturated C atoms at

the ends had some partial charge up to 2 Å from the ends, but this fell rapidly to zero beyond 2 Å. CNTs, therefore, have been considered and modelled as carrying no partial charges. BNNTs, on the other hand, carry a partial charge due to the covalent bond between B and N with both having different electronegativities. The magnitude of this partial charge, however, remains disputed and depends on environmental factors, such as whether or not the nanotube is hydrated. The partial charges obtained from different ab-initio studies for BNNTs are presented in Table 2.1.

Table 2.1: B-N partial charges in literature. ($*$ = used in this study)

References	Partial charge ($\pm$e)
Won and Aluru (2008)	0.4–1.05
Hilder *et al.* (2009a), Ritos *et al.* (2014), Wei and Luo (2018)	1.05
Casanova *et al.* (2020b)	0.96*
Hilder *et al.* (2010)	0.98
Hilder *et al.* (2009a)	0.4
Sam *et al.* (2018)	0.35
Wu *et al.* (2016), Liang *et al.* (2017), Zhang *et al.* (2019a)	0.3

The partial charges on B-N atoms fall into two narrow bands — one around $\pm$1.0e, and another around $\pm$0.3e. The reason for this discrepancy may be traced back to Won and Aluru (2007), who found, using DFT, partial charges of $\pm$1.05e when the nanotube was filled with water and $\pm$0.4e when the nanotube was empty. Nevertheless, both values of partial charges have been used to simulate BNNTs in contact with water.

2.2 Flow through nanotube membranes

The very first experiments with wetting on CNTs were concerned with finding which liquids could fill up a CNT. By 1995, it was established that CNTs could be filled by water, along with other liquids that have surface tension $\leq$ 200 mN/m, such as liquid sulphur, selenium and cesium (Dujardin *et al.* (1994); Ebbesen (1996)). The high transport rate of liquids through CNTs was first discovered around the early 2000s (Hummer *et al.* (2001); Kalra *et al.* (2003); Skoulidas *et al.* (2002)) using molecular dynamics simulations. Around the same time, graphite capillaries were also shown to have high slip lengths (Sokhan *et al.* (2001)), and it was established that transport within nanotubes was quasi-frictionless for these fluids (Kalra *et al.* (2003); Sokhan *et al.* (2002)). Fast transport of water through nanotubes was experimentally established by Majumder *et al.* (2005) and Holt *et al.* (2006), who found water flows through CNTs four to five orders of magnitude faster than predicted by conventional flow theory. The prospect of using CNTs for separation had already been proposed for hydrocarbons (Mao and Sinnott (2001); Srivastava *et al.* (2004)), and the benefits of utilising CNTs for salt separation

from seawater was also quickly realised. Closely on the heels of this discovery, Won and Aluru (2007) found that BNNTs could also conduct water, perhaps even faster and at narrower diameters than CNTs.

The discovery of large slip lengths, or equally, large flow enhancement in CNTs set off a concerted effort into quantifying, and understanding, the magnitude and nature of this phenomenon. This produced a large body of work that looks into various aspects of flows through CNT membranes, and their utility as desalination membranes. The initial experimental predictions of up to 5 orders of magnitude higher flow rate than the no-slip case by Majumder *et al.* (2005) and Holt *et al.* (2006) could not be replicated in the later experiments (Lee *et al.* (2015); Mattia *et al.* (2015); Qin *et al.* (2011); Secchi *et al.* (2016)), which found enhancements below three orders of magnitude. MD studies (Falk *et al.* (2010); Suk *et al.* (2008); Thomas and McGaughey (2008)) also failed to find the extremely high flow rates of the earlier experiments. Certain explanations were put forward for this seeming discrepancy by Thomas and McGaughey (2008) and Walther *et al.* (2013) among others, and the consensus view appears to have settled at a diameter dependent flow enhancement of only up to three orders of magnitude for CNTs with $D > 2$ nm (Borg *et al.* (2018); Kannam *et al.* (2013); Ritos *et al.* (2015)). Thinner CNTs that have not yet been studied experimentally could potentially show enhancements of up to five orders of magnitude (Borg *et al.* (2018)).

From a theoretical perspective, flows through cylindrical tubes and channels can be modelled using the Hagen-Poiseuille-Weissberg (HPW) equations. The full pressure loss across one nanotube, considering Navier slip (defined below) in a membrane can be shown to be:

$$\Delta P = \underbrace{\frac{8\mu C^3}{D^{*3}}}_{\text{Weissberg end loss term}} + \underbrace{\frac{128\mu LQ}{\pi (D^*)^4 (1 + 8L_s/D^*)}}_{\text{HP term}}, \tag{2.2}$$

where C is the Weissberg's constant (~ 3.0), μ is the viscosity of the liquid, D^* is the hydrodynamic diameter of the nanotube, L is the length of the nanotube, Q the volumetric flow rate and L_s is the slip length. The Weissberg end loss term (Weissberg (1962)) in equation 2.2 accounts for the pressure drop due to the entrance and exit effects, while the HP term accounts for pressure loss within the channel. The HP term in equation 2.2 needs to account for boundary slip because the no-slip assumption, i.e., the assumption that fluid velocity at the wall boundary would equal the wall velocity, breaks down at nanometre length scales. The slip length, therefore, is the distance from the wall in the cross-flow direction at which the fluid velocity would virtually become equal to the wall velocity if the fluid velocity kept decreasing with the same gradient which it had at the wall location, shown in Figure 2.3. The slip length L_s relates to the slip velocity V_s as $V_s = L_s \partial u/\partial y$, where u and y are as shown in Figure 2.3, and L_s as defined is known as the Navier slip. The slip length differs from material to material, depending on various atomic parameters. Bocquet and Charlaix (2010) provide a

relation between L_s and fluid-material parameters:

$$L_s \sim \frac{kT\mu D_f}{C_\perp \rho \sigma \varepsilon^2}, \tag{2.3}$$

where μ is the fluid viscosity, D_f the diffusivity coefficient of the fluid, $C_\perp$ is the geometric factor corresponding to atom roughness of the solid surface, ρ is the fluid density, and σ and ε are a measure of the interaction strength (defined in section 3.2.1) between the fluid and solid atoms. The Weissberg end loss term accounts for the losses arising due to the fluid bending at the pore entrance.

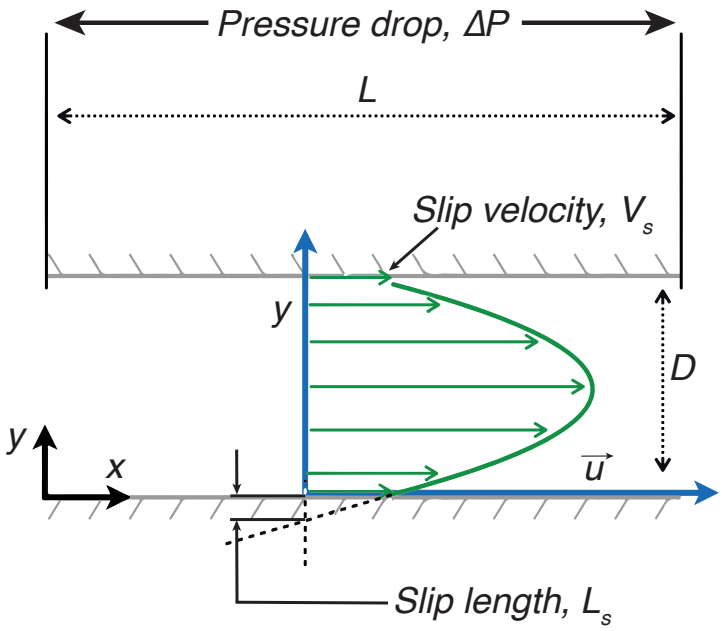

Figure 2.3: HP flow velocity profile with slip

Why do nanotubes have high slip?

The reason why nanotubes conduct water almost without friction can be explained using the theory of slip derived from the Molecular Kinetic Theory (MKT), first proposed by Eyring (1936)). The original MKT theory attempts to set the relationship between the rate at which a reaction proceeds, and the activation energy barrier, which is needed to be overcome for the reaction to proceed. The phenomenon of slip can also be modelled similarly, as shown in Figure 2.4. The surfaces of nanochannels are made up of atoms, and a spherical region of influence is generated due to the van der Waals force extending around each atom, where depending on the distance from the atom, it might attract or repel other atoms. In certain cases where the atoms are arranged in lattices, like in a graphene sheet or CNTs and BNNTs, these regions of influence intersect with each other to create hills and valleys such that it becomes favourable for a fluid particle to remain stuck within a valley, shown in Figure 2.4. The phenomenon of

slip can then be thought of as the rate at which fluid molecules can escape the valleys, in the direction of the fluid flow, assisted by the shear force of the fluid. The energy required to climb out of the valley can then be interpreted as activation energy. With slight modifications to the original equations, Ruckenstein and Rajora (1983) showed that the slip velocity V_s relates to the potential energy barrier E_{diff}, atom spacing δ and shear force τ as:

$$V_s \propto \exp\left(-E_{\text{diff}}/kT\right)\sinh\left(\tau/\tau_0\right), \tag{2.4}$$

where k is the Boltzmann constant, T is the temperature and τ_0 is a constant equal to $2kT/\delta$. Several reformulations of equation 2.4 have since appeared, notably in Hu *et al.* (2017); Shu *et al.* (2016); Wang and Zhao (2011); Yang (2010) and Wang and Hadjiconstantinou (2019), largely due to differences in the choice of fitting parameters. The proportionality relation has been shown to hold in all the above studies, given a proper selection of the fitting parameters. Since equation 2.4 is a proportional equation, it cannot be used to directly calculate V_s (or L_s).

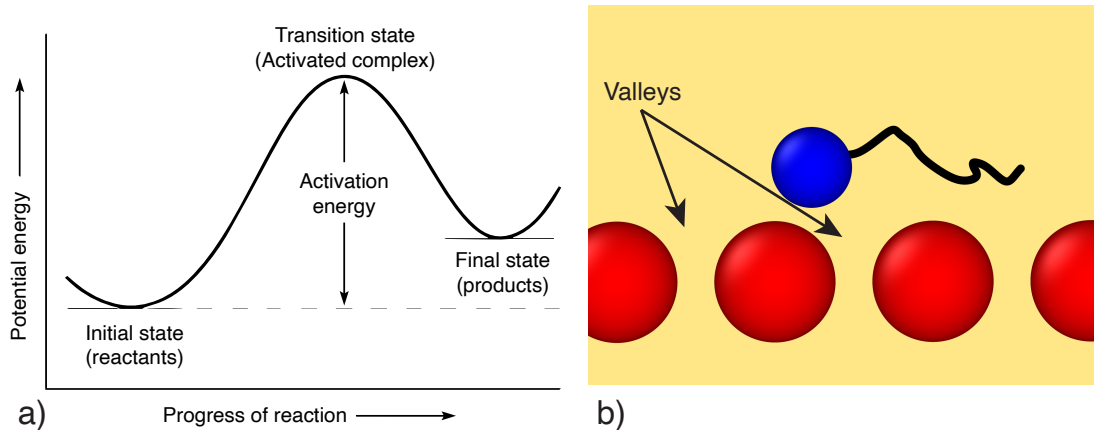

Figure 2.4: (a) Activation energy in chemical reactions. (b) A fluid atom (blue) jumping over wall atoms (red)

Falk *et al.* (2010) showed that when graphene sheets are rolled to form CNTs, the potential energy barrier reduces as the atoms on the graphene lattice are squished together in a cylindrical arc, overlapping each other more and reducing the extremes of potential energy which a fluid molecule near the surface would have to overcome to jump out of the wells (Figure 2.5). This also means that the narrower the nanotube, the higher the slip, or the lack of friction from the nanotube surface. They found the friction coefficient reduces from 8.14×10^3 Ns/m^3 for a nanotube with $D = 5.4$ nm to 0.47×10^3 Ns/m^3 for a nanotube with $D = 1.0$ nm.

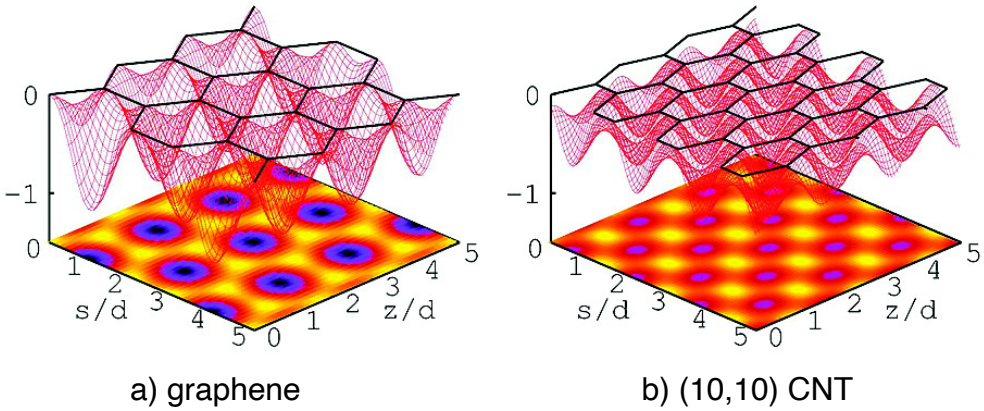

Figure 2.5: Variation of potential energy surface between flat graphene sheets and rolled CNT. Image taken from Falk *et al.* (2010).

Comparing BNNTs and CNTs

BNNTs were shown to continuously conduct water down to diameters of 0.69 nm due to their higher wettability, at which diameters CNTs filled only intermittently (Won and Aluru (2007)). Suk *et al.* (2008) and Hilder *et al.* (2009a) compared BNNTs to CNTs, and showed flow rates in BNNTs were equal, or higher than CNTs. Hilder *et al.* (2009a) claimed BNNT membranes could provide up to 5.2 times higher flow rates compared to commercially available membranes, against the 2.4 times higher flow rate provided by CNT membranes. Despite this early promise in small diameter BNNTs, research into BNNTs lagged due to manufacturing difficulties. The few experiments and simulations on BNNTs show contrasting results when it comes to water transport performance: more recent work tends to show that BNNTs offer more flow resistance and therefore lower flow rates compared to CNTs (Casanova *et al.* (2020b); Ritos *et al.* (2014); Secchi *et al.* (2016); Wei and Luo (2018)), especially for wide BNNTs ($D >$ 1 nm, where $D =$ nanotube diameter), while the earlier works show BNNTs outperforming CNTs, especially for the narrow ($D < 1$ nm) cases (Hilder *et al.* (2009a); Suk *et al.* (2008); Won and Aluru (2008)). That BNNTs might be better than a comparable CNT for water permeation was first shown by Won and Aluru (2007), who found that the (5,5) BNNT ($D = 0.69$ nm) could conduct water continuously unlike comparable CNTs, and the water inside had a higher axial diffusion coefficient. Hilder *et al.* (2009a) found the (5,5) BNNTs offering nearly 2.17 times the permeability of CNTs. Similarly, Suk *et al.* (2008) show that (6,6) BNNTs ($D = 0.83$ nm) offer marginally higher flows than CNTs, with 26% higher water flow at 24 molecules/ns for BNNTs, compared to 19 molecules/ns for CNTs at 200 MPa of applied pressure. BNNTs were also found to have lower energy barriers to the entry and transport of water inside the nanotube, at 5.15 kT and 0.23 kT respectively, compared to the 5.27 kT and 0.47 kT for CNTs. Liang *et al.* (2017) and Azamat *et al.* (2016) both show BNNTs (for $0.66 < D < 1.09$ nm) permit higher flow rates of water when compared with CNTs. Ritos *et al.* (2014), on the other hand, show BNNTs with $D = 1.036$ nm permit a lower flux of pure water compared to CNTs.

They found a flow rate of only 15 $\mu m^3/s$ through very long BNNTs, compared to the nearly 4.2 times higher flow rates through CNTs at 64 $\mu m^3/s$. Studies of the friction coefficient from Tocci *et al.* (2014) and Wei and Luo (2018) show 2-D BN sheets and BNNTs with $D = 1.1$ nm, respectively, have friction coefficient λ an order of magnitude higher compared to graphene sheets and CNTs. Sam *et al.* (2018) find that BNNTs (for $D = 4.98$ nm) have a slip length of an order of magnitude lower ($L_s \sim 8$ nm) compared to CNTs ($L_s \sim 60$ nm). Experimental evidence from Secchi *et al.* (2016) for $D > 7$ nm shows that BNNTs had no slip length, compared to hundreds of nanometres for CNTs. The literature, therefore, seems to indicate BNNTs outperform CNTs at small diameters.

While the contradictions in the flow enhancement, or conversely, the slip length, and therefore the flow rate of water through CNTs was largely resolved using a mix of experimental and simulation studies conducted for over more than a decade, a similar concerted effort appears to be missing for BNNTs. This is largely due to the perceived unfavourability of manufacturing BNNT membranes when high permeance is the only desired characteristic of the membrane. This unfavourability changes with a focus on high selectivity alongside high permeability and recent advances in the fabrication of BNNT membranes (Casanova *et al.* (2020a); Kim *et al.* (2016)). As BNNT membranes emerge as a frontrunner for desalination systems, the basic question remains unanswered — how fast does water flow through BNNTs?

2.3 Particle rejection and selectivity in nanotube membranes

The selectivity of a membrane is its ability to allow only desired molecules to pass through it. It may be expressed as a ratio of permeabilities of desired and undesired molecules through the membrane. A common measure used for comparison of the selectivity of desalination membranes is the inverse salt permeability or the inverse of the volume of salt passing through a unit area of the membrane face within a unit time. Historically, high membrane selectivity has been desirable for *niche applications*, such as in biological molecular sensing devices (Bayley and Cremer (2001); Woodhouse *et al.* (1999)), in chemical and pharmaceutical industries to obtain desired purity levels (Marchetti *et al.* (2014)), in the food industry to produce concentrates (Howell *et al.* (1993)) and in the biotech industry (Saxena *et al.* (2009)) among others. High selectivity is generally crucial when human consumption or biological devices for human use are involved, or when the chemical to be selected is expensive in an industrial sense. With the growing realization that RO membranes were reaching the thermodynamic limit of energy usage (Elimelech and Phillip (2011)) for desalination purposes, new research was needed to explore other avenues for cost reductions in the operation of desalination membranes. While RO membranes are operating near the thermodynamic limit, the cost of desalinating seawater ($\sim$ 0.4–0.7 \$/m^3 Guo *et al.* (2014); Hoslett *et al.* (2018); Karagiannis and Soldatos (2008)) at the thermodynamic limit remains an order of magnitude higher than current methods involving

filtering freshwater ($\sim$ 0.02 \$/m^3 Hoslett *et al.* (2018)). Werber *et al.* (2016a), Werber *et al.* (2016b) and Park *et al.* (2017) therefore advise to improve the selectivity of membranes, instead of attempting further energy reductions by improving permeance.

High selectivity is typically achieved through tailoring the membrane pore size (Azamat *et al.* (2016); Mehta and Zydney (2005)), the membrane charge (Cheng *et al.* (2018); De Grooth *et al.* (2014); Van Reis (2001)) and adding functional groups to the membrane surface (Chan *et al.* (2016); Chogani *et al.* (2020); Gupta *et al.* (2015); Roy *et al.* (2014); Vatanpour *et al.* (2017); Zhao *et al.* (2014)). Substances going through a membrane need to have sufficient energy to overcome the resistance posed by the membrane. The essence of increasing the selectivity is to increase the relative difference of this energy barrier for crossing the membrane faced by the unwanted solute and the desired components of the solution. This is usually achieved by increasing the energy barrier for the unwanted ions. The increase in energy barrier, especially when done by reducing the membrane pore size to reject unwanted solutes, results in an increase in energy barrier for all other constituents of the solution too. This results in a permeability-selectivity trade-off, where any increase in selectivity of a given membrane results in a decrease in permeability of that membrane. This trade-off between permeability and selectivity was first observed for gas separation membranes (Robeson (1991)) and later theorized and extended to all membranes (Freeman (1999); Mehta and Zydney (2005); Werber *et al.* (2016b)). The rejection of a membrane R can be expressed as

$$R = 1 - \frac{c_{\text{permeate}}}{c_{\text{feed}}}, \tag{2.5}$$

where c_{permeate} is the concentration of the unwanted solute in the permeate coming out of the membrane. c_{feed} is the concentration of unwanted solute in the feed solution coming into the membrane. The permeability-selectivity curve is depicted in Figure 2.6, taken from Werber *et al.* (2016b).

Increasing selectivity using electric fields, either through charged membranes or externally applied, represents a unique way of increasing selectivity, especially for charged solutes, without sacrificing permeability. This is due to a water molecule being a dipole, which results in electric fields producing a torque on the molecule instead of a directional force produced on an ion. Electric fields have been shown to increase water permeability through nanotube membranes due to the resulting re-alignment of water molecules (Ritos *et al.* (2016); Su and Guo (2011); Suk and Aluru (2010)). A common way of applying an electric field is by charging the membrane — either by having charged atoms within the membrane structure, adding charged functional groups to the membrane surface, or creating the membrane using materials that can hold an intrinsic charge. Selective exchange of ions through a membrane with some of the ions immobilized was theorized by J.W. Gibbs in 1878 (Gibbs and Smith (1878)) and developed experimentally by F.G. Donnan in 1911 (Donnan (1911)). While Donnan studied the exclusion of ions of the same charge when they were separated by a semi-permeable

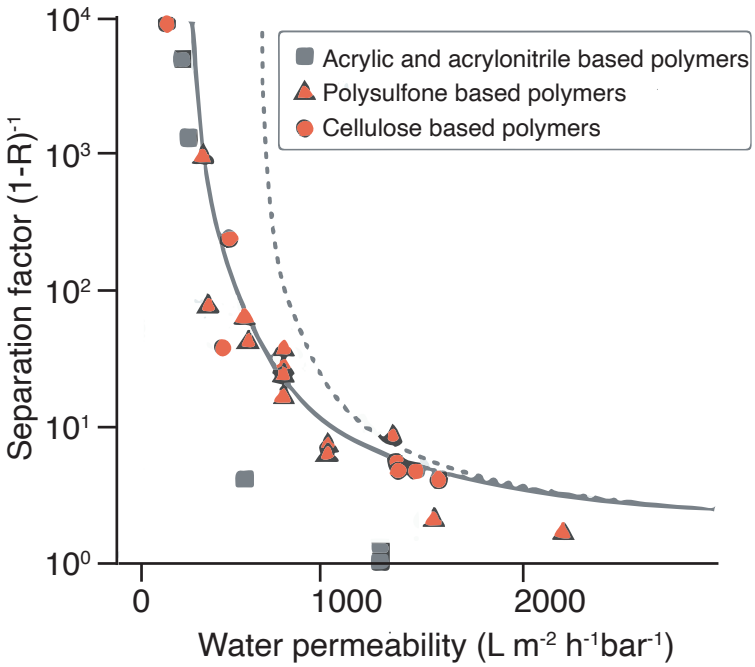

Figure 2.6: Rejection vs permeability in polymeric membranes. The solid grey line represents theoretical results using a log-normal distribution of membrane pore sizes with standard deviation of 0.2, while the dashed line represents theoretical results with uniform pore size. Data points are from experiments. Figure taken from Werber *et al.* (2016b).

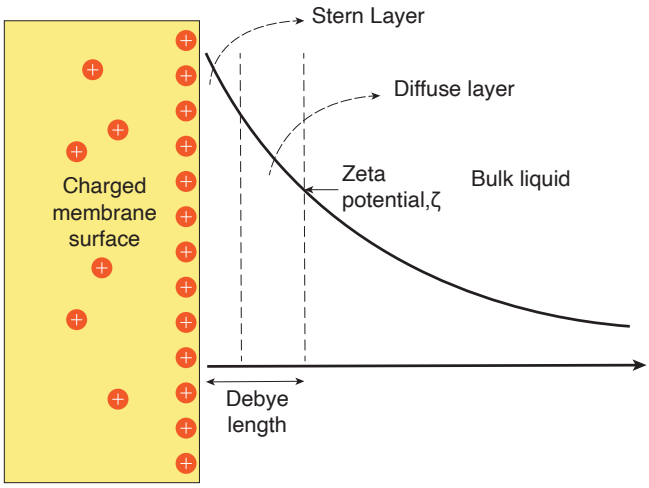

Figure 2.7: Variation of electric potential in an electric double layer.

membrane, the same phenomenon holds when there are charges locked in the body and surface of the membrane. This keeps ions with the same charge as the membrane away from the pores while attracting oppositely charged ions, and this phenomenon is termed the Donnan exclusion. Donnan exclusion has been actively investigated as a mechanism for the selective filtration of charged species (Sarkar *et al.* (2010); Seidel *et al.* (2001); Tran *et al.* (2019); Xu *et al.* (2006)).

Characterizing the extent of the Donnan exclusion requires knowledge of the surface charge on the membranes, in addition to the valency and concentration of the ions in the feed solution. When a charged membrane is brought into contact with a solution containing ions, the ions with the opposite charge as the membrane (counter-ions) form a layer adjacent to it. This attracts some ions which have the same charge as the membrane (co-ions). This arrangement is known as the electric double layer and gives rise to a decreasing electric potential with increasing distance from the membrane surface, shown in Figure 2.7. Since the surface charge on a membrane cannot be directly measured in experiments, the zeta potential at a certain distance from the surface, known as the Debye length, can be measured. The distance from the surface at which the zeta potential is measured is such that it falls outside of the Stern layer, which is a layer of ions with opposite charge to that of the membrane surface. Ions in the Stern layer are assumed to be immobile, and therefore, it is the zeta potential that plays a larger role in the dynamics of the ions in the feed solution moving towards the membrane (Peeters *et al.* (1999)). The surface charge density σ_{sc} can be estimated from the zeta potential using

$$\sigma_{sc} = \varepsilon_e \zeta \kappa^{-1}, \tag{2.6}$$

where ε_e is the electrical permittivity of the medium, ζ is the zeta potential and κ^{-1} is the Debye length.

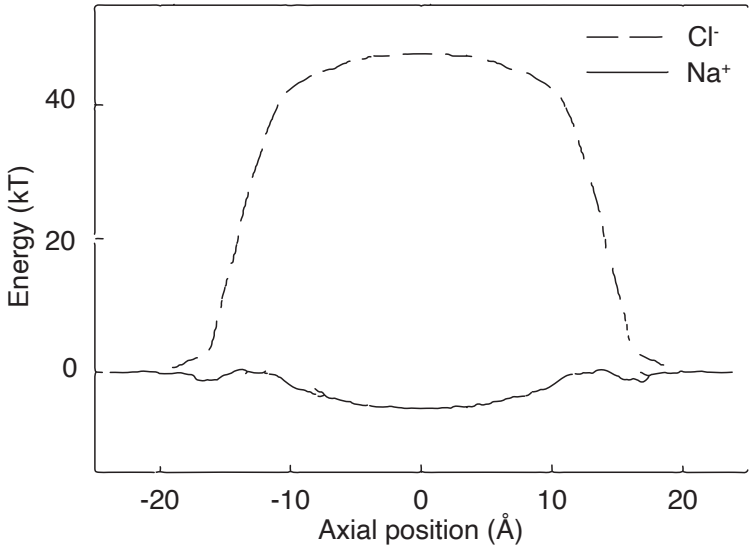

Figure 2.8: Free energy profile across a (7,7) cation-selective BNNT. Figure taken from Hilder *et al.* (2009b).

Richard Bowen *et al.* (1999) investigated the dynamics of a single charged particle in front of a charged membrane surface, and showed that particles had an equilibrium position above the membrane surface. At this equilibrium position, the drag force from the water driving the particle towards the pore equalled the electrostatic repulsion from the membrane surface. The particle could therefore be removed by a tangential flow. However, Bowen and Sharif (2002) showed that incorporating the role of Brownian forces allows the particle to sometimes cross into the pore even with strong repulsion and weak drag force from the water. Moritz *et al.* (2001) investigated the role of surface charges on filtration by like- and oppositely-charged particles on the membrane surface, and found a much higher flux of the permeate when both the membranes and ions in solution had high negative charges. They attributed this to electrostatic repulsion from the membrane surface that made it harder for a cake layer (a layer of compressed foulants) to form, allowing high permeation rates. Therefore, despite some particles escaping, electrostatic repulsion through charged membrane surfaces was shown to be capable of providing higher rejection rates.

BNNTs are known to have a charged structure due to the nature of the covalent bond between the boron and nitrogen atoms. In addition to having a charged structure, which might contribute to anti-fouling and selectivity, BNNTs also offer advantages of being non-toxic (Chen *et al.* (2009)) unlike CNTs, making them a very promising candidate for desalination. Early MD studies by Hilder *et al.* (2009b) showed that BNNTs could selectively allow cations or anions based on their diameter, due to the interactions of the ions with the charged structure of the nanotube. In addition, the free-energy profile across the length of the BNNT showed large differences for cations and anions, shown in Figure 2.8.

The high zeta potential of BNNTs was experimentally verified by Siria *et al.* (2013), who used it to effect high osmotic currents by creating a salinity gradient across a BNNT. Therefore BNNTs may prove to be an ideal membrane for separating negatively charged ions due to their high negative surface zeta potential and their high slip lengths. The high zeta potential arises due to the formation of B-O-H and N-O-H bonds when BN is in contact with water (Crimp *et al.* (1999); Joni *et al.* (2011)). The high zeta potential allows BNNTs to offer both charge-based and size-based steric rejection, in contrast to CNTs, which offers only size-based steric rejection (Thomas and Corry (2016)).

While Hilder *et al.* (2009b) performed some initial studies on selectivity in BNNTs, this selectivity was largely studied by varying the diameter of the BNNT, which reintroduces the selectivity vs permeance trade-off. An investigation into charged particle rejection due to the zeta potential of BNNTs is needed, since this would be less constrained by the pore diameters. This removes the need to create precise diameter nanotubes, and would provide a membrane candidate with high selectivity, as is the need of the future.

2.4 Membrane cleaning

Membrane fouling is typically observed as an increase in the transmembrane pressure required to maintain a desired flow rate through the membrane. This is caused by the deposition of foulants from the feedwater onto the membrane surface and pores (see Figure 2.9), causing an increase in the energy input required to maintain the same flux, a drop in the permeate flux, and/or a decrease in the quality of the permeate. Foulant buildup over time may render the membrane unusable until sufficient cleaning procedures are used, further increasing the cost associated with membrane-based filtration systems. Measures such as the decline in flux and transmembrane pressures are, however, inadequate for predicting a fouling situation developing. This is because by the time a noticeable decline in the flux has occurred, the membrane might be irreversibly fouled (Saad (2004)). This necessitates continuous monitoring and cleaning of the membrane. Flemming (1994) estimate that fouling accounts for 30% of the operating costs of a membrane-based desalination plant and reduces the membrane life by up to 66%. Abdul Azis *et al.* (2001) estimate that biofouling in desalination plants alone costs about US$15 billion yearly.

Types of foulants

Broadly, foulants for RO membranes can be classified into scaling, biological fouling, organic fouling and chemical fouling (Goh and Ismail (2018); Rezakazemi *et al.* (2018)). The mechanism of membrane fouling depends on the particular interactions between the combination and type of foulants and membrane. Depending on the kind of membrane, the fouling may occur largely on the surface of the membrane, as in the case of polyamide RO membranes, or both

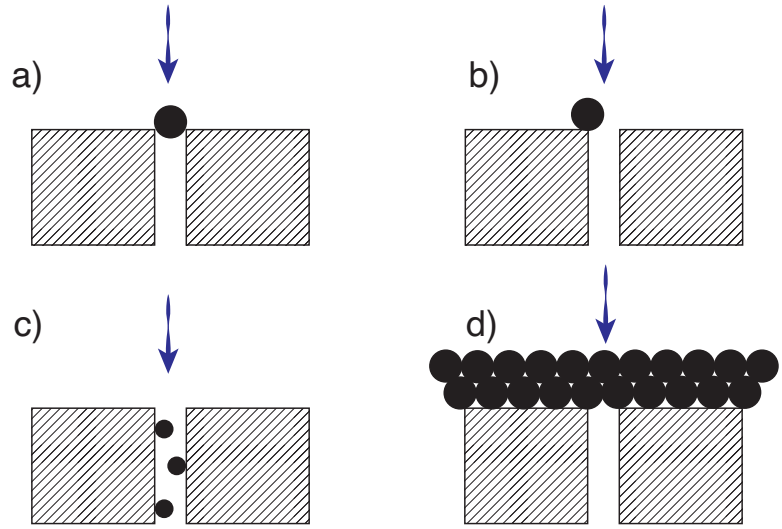

Figure 2.9: Types of fouling: a) Pore blocking; b) Partial pore blocking; c) Internal pore blocking; d) Cake formation. Blue arrows represent flow direction.

on the surface and within the pore, as in the case of porous membranes. The types of fouling can be largely classified into: (a) deposition of particles on the membrane surface and pores, (b) formation of a cake layer on the membrane surface, (c) pore blockage by foulants and (d) biofilm formation on the membrane surface and pores (Rezakazemi *et al.* (2018)).

2.4.1 Membrane fouling mechanisms

Colloidal fouling

Colloidal fouling occurs with particles of diameters between 1 nm and 1 μm. Particles accumulate on the membrane surface and pores initially through direct capture on the membrane, and then aggregate as the directly captured particles bind with more colloidal particles in the fluid (Dersoir *et al.* (2019)). Cake formation occurs when the pore is completely blocked, effectively taking over the role of the active layer of the membrane (Guo *et al.* (2012)) (see Figure 2.9d). The application of higher pressures to compensate for the blocking leads to cake compression, where a skin is formed near the membrane surface accounting for 10-20% of the cake thickness, but 90% of the cake resistance to the flow (Shirazi *et al.* (2010)).

Concentration Polarization

Concentration polarization occurs due to the concentration of the solute or foulant increasing on the feed water side (inlet) of the membrane as it is being rejected by the membrane, and keeps increasing if there is inadequate crossflow to take the solute away from the membrane inlet. Cake formation also results in an increase in the concentration polarization due to the absence of cross-flow within the cake. The high concentration of solute in front of the membrane results in the apparent reduction of the rejection ability of the membrane. This phenomenon is

known as cake-enhanced concentration polarization. (Chong *et al.* (2008); Hoek and Elimelech (2003)).

Organic fouling

Organic fouling is caused by organic matter such as humic substances, proteins, polysaccharides, lipids, nucleic acids, amino acids, organic acids, and cell components (Jiang *et al.* (2017)). Of these, the most commonly occurring mix of substances is classified as natural organic matter (NOM), composed of humic substances (Zhao *et al.* (2021)). For RO membranes, these organic matter have been found to foul the membrane first through direct deposition on the membrane due to membrane-foulant interactions, followed by foulant-foulant interactions (Ang and Elimelech (2007)). Fouling by humic substances was found to result from hydrophobic interactions between the membrane and foulants (Yu *et al.* (2010)), while fouling by alginates was aggravated by decreasing pH and increasing ionic strength (Lee and Elimelech (2006)). The initial stages of the fouling were dominated by organic compounds of low molecular weight, followed by the majority of the fouling by high molecular weight compounds (Lee *et al.* (2008)). High molecular weight compounds were also found to be easier to remove from the membrane surface compared to lighter molecules (Fabris *et al.* (2007)). This indicates that lighter particles may remain after cleaning and act as seeding locations for further fouling.

Inorganic fouling

Inorganic fouling or scaling is caused by ions that have limited solubility in water. Once the liquid near a membrane becomes locally saturated with ions (say due to rejection of the ions), they precipitate out of the solution and deposit on the membrane (Jiang *et al.* (2017)). The growth of these inorganic crystals on the membrane is first through the nucleation stage followed by either homogenous or heterogeneous crystal growth until a cake layer is formed in the membrane (Al-Amoudi and Lovitt (2007)). The main inorganic foulants studied by researchers were calcium sulfates and carbonates, which are also the most common (Ochando-Pulido *et al.* (2015)).

Biological fouling

Biological fouling is typically caused by bacteria or algae, forming a biofilm over the membrane surface and pores. Like other forms of fouling, biofouling also follows the growth stages of initial attachment of bacteria, followed by growth through reproduction as they consume other matter present in the feedwater (Zhao *et al.* (2021)). As the bacterial colonies grow, they secrete extracellular polymeric substances which help bind the bacteria in the film together and protect the bacteria from pre-treatment methods such as the use of biocides. The presence of transparent exopolymers in the feedwater also helps in the bio-adhesion and growth of the biofilm (Kennedy *et al.* (2009)). This is followed by an additional stage where the bacteria leave the mature biofilm (either due to lack of nutrients or overcrowding) and attach themselves to

new surfaces, repeating the cycle (Creber *et al.* (2010)). Biofouling, therefore, has been noted as one of the more severe forms of membrane fouling due to the ability of the microorganism to replicate and relocate to different parts of the membrane (Hibbs *et al.* (2016); Ni *et al.* (2014); Zhao *et al.* (2021)).

The varied types of fouling indicates that a universal cleaning technique is unlikely to apply to all kinds of fouling, and anti-fouling and membrane cleaning technologies must be tailored for the membrane-foulant combination. However, the stages of fouling remain similar irrespective of the kind of fouling, with a few particles initially depositing onto the membrane and acting as seeds to catch other particles and turn into a growing agglomerate. The common types of membrane cleaning methods include physical, chemical, biological and enzymatic cleaning (Jiang *et al.* (2017); Wang *et al.* (2014)). Chemical cleaning refers to the washing of membranes with various chemicals, often tailored to the kinds of foulants on the membrane. Physical cleaning refers to the use of mechanical action to remove the foulants from the surface. Biological and enzymatic cleaning use chemicals which specifically target micro-organisms and organic matter.

2.4.2 Membrane cleaning mechanisms

Chemical cleaning

Chemical cleaning remains the most popular method of membrane cleaning. Chemical cleaning also remains the focus of numerous studies to tailor their cleaning efficacies to different kinds of foulants. It is primarily used when simple physical cleaning, such as rinsing or backflushing, is not strong enough to remove the foulants from the membrane surface. Chemicals are used in two different ways: to weaken the adhesive force between the foulants and the surface, and to increase the interaction between the foulant and water such that the foulant can be flushed away with the water. Chemical cleaning may be divided into three main categories: (a) acids, which are used to clean inorganic foulants, (b) alkalis, which are used to clean organic foulants, and (c) biocides, which are used to treat biological fouling (Gao *et al.* (2011)).

Chemical cleaning of inorganic matter

Inorganic matter such as salts of calcium and silicates, which may result in the scaling of the membrane, is cleared using anti-scaling agents based on acids, such as carboxylic, citric, sulphuric or polyacrylic acid (Lyster *et al.* (2010); Zsirai *et al.* (2018)). Citric acid is found to be particularly effective against iron oxides. In addition, chelating agents such as EDTA (Ethylenediaminetetraacetic acid) may be used to remove salts of divalent cations, such as calcium (Hong and Elimelech (1997)).

Chemical cleaning of organic matter

Alkaline solutions like NaOH are effective against organic foulants by dissociating organic molecules which have acids or phenolic groups as their functional group and increasing the

negative charge on the molecules, which increases their solubility (Thurman and Malcolm (1983)). However, residual proteins might remain stuck due to strong foulant-membrane interactions, potentially acting as seeds for future fouling (Blanpain-Avet *et al.* (2009)).

Chemical cleaning of biological films

The preferred method for the cleaning of biological films is the use of biocides, despite microbial organisms being highly resistant to them (Gilbert *et al.* (2003)). Biomass on the membrane surface is retained, acting as feed for the future growth of microbes (Flemming (2011)). Flemming also notes that most biocidal treatments are often carried out as *arbitrary mixtures of complexing substances, enzymes, shock dosages of oxidizing and non-oxidizing biocides and pH shocks*. Biocides do not address the twin challenges of residual biomass still on the membrane surfaces, and the ability of microbes to quickly establish themselves in large numbers soon after the microbial treatment.

Drawbacks of chemical cleaning

Despite their ability to be tailored to a wide range of foulants and fouling conditions, the chemical cleaning of membranes suffers from a few important drawbacks. Most chemical cleaning procedures require a complete shutdown of the filtration or desalination plant to avoid any cross-contamination with clean water. Removal of residual organic and biological materials often necessitates the use of strong oxidizing or reducing agents, which interferes with the structure of the membrane and may corrode the active layer of the membrane, severely reducing its life (Cheryan (1998); D'Souza and Mawson (2005)). Cleaning of industrial-scale desalination and filtration plants require large volumes of chemicals to be used, and then the membrane is subsequently flushed to remove the chemicals from the surfaces. This poses a waste disposal problem, as the introduction of this wastewater to aquatic bodies would disrupt not only living organisms but also population centres dependent on the water body. In the case of biofilms, where the effects of fouling are most severe and its control most difficult, chemical cleaning alone fails to effectively remove all microbes and biofilms, and physical cleaning is recommended to properly clean the membrane (Flemming (2011)).

Physical cleaning

Physical cleaning of membranes involves imparting energy directly to the foulants to break free of the membrane-foulant interaction, unlike chemical methods which seek to decrease the strength of the foulant-membrane interaction. Physical methods range from simple mechanical techniques, such as rinsing or backflushing of the membrane, to the use of ultrasonic vibrations to break up the foulants. Physical methods may be used in conjunction with chemical methods to carry away the broken down foulants from the membrane surface.

Backflushing

Backflushing is carried out by reversing the applied transmembrane pressure, causing the foulants to be carried back into the flow away from the feed side of the membrane. An increase of flow velocity and shear rate at the membrane surface improves the efficacy of the cleaning (Baker *et al.* (1985); Riesmeier *et al.* (1989)). It has been reported to be effective even against biological films, as unlike biocides it physically removes the films from the membranes. (Kroner *et al.* (1987); Matsumoto *et al.* (1987, 1988); Nipkow *et al.* (1989)). Osmotic backwashing is done by increasing the salt concentration and reducing the pressure on the feed side, and/or increasing pressure on the permeate side, such that the osmotic pressure itself drives a flow from the permeate side to the feed side (Avraham *et al.* (2006)). An additional benefit of this type of backwashing is the introduction of high salinity feedwater, which acts as an environmental shock to microbes on the membrane surface, and can even dissolve microcrystals of calcium salts (Qin *et al.* (2009)). Backwashing is not favourable where inorganic scaling has been developing for some time (Jiang *et al.* (2017)).

Vibrations

Ultrasonic vibrations have been investigated as a cleaning mechanism for a considerable time, with articles appearing as far back as 1970 (Fairbanks and Chen (1970)). Tarleton and Wakeman (1992) presented experimental evidence of ultrasonic vibrations at 23 kHz being able to reduce the fouling of membranes in 1992. A number of studies have since followed on the ultrasonic cleaning of membranes (Chai *et al.* (1998); Chen *et al.* (2006); Kobayashi *et al.* (1999); Kokugan *et al.* (1995); Li *et al.* (2002); Lim and Bai (2003); Masselin *et al.* (2001); Matsumoto *et al.* (1996)). In-situ vibrations have been favoured for cleaning membrane bioreactors, which are used for the harvesting of algae. Low frequency linear and cyclic vibrations of ~ 5 Hz have been found to significantly reduce the incidence of biofouling due to algae (Bilad *et al.* (2013); Zhao *et al.* (2018)).

Heating

Heating the feed flow has been considered as a method for increasing the membrane permeance by reducing the fluid viscosity (Zhao and Zou (2011)). Membrane bioreactors are known to foul more at lower temperatures, implying heating can reduce biofouling (Miyoshi *et al.* (2009)). Peng and Tremblay (2008) showed that cleaning membranes by backflushing them with hot water or steam was more effective in recovering the flux than chemical cleaning when the membrane was fouled by oily wastewater. Aumeier *et al.* (2018) investigated the cleaning of membranes using water heated to 140 °C, and injected into the membrane at elevated pressures to keep it liquid. The evaporation of water into vapour inside the pores of the membrane provided shear force to knock the foulants off the membrane. Lohaus *et al.* (2020) found a 30% reduction in fouling when heating is used in conjunction with backflushing at temperatures of 50 °C. They credit the possibility of induced shear flow at the membrane surface due to the heating as the reason for cleaning. Nguyen *et al.* (2020) recently studied heating the membrane directly to temperatures of 180 °C to remove bacteria from the membrane

surface. Typically, target temperatures for heating should be high enough to generate bubbles at the given operating pressures. Lohaus *et al.* (2020) cite energy consumptions of 7 W for 300 seconds of backwashing, for a setup capable of producing 0.09 L/h of permeate. This amounted to a claimed 40% reduction due to heating only the membrane and not the oncoming stream. Backwashing was carried out for every 70 minutes of filtration. Direct heating of the membrane, however, is a mostly unexplored area, with only a few published studies but with promising results, especially for biofouling. There is currently no fundamental understanding of the mechanisms of foulant removal using direct membrane heating, and this necessitates a molecular level treatment, which currently is missing in the literature.

Summary

Membrane fouling is one of the biggest challenges, behind high energy consumption, which makes desalination on a large scale an expensive process. Membranes usually foul in stages, irrespective of the kind of foulant, starting from small seed attachments to the membrane surface which then keep agglomerating more particles. The dominant method of cleaning is through the use of chemicals, which not only corrode the membrane itself but also need the desalination process to be stopped while cleaning is ongoing. Furthermore, chemical cleaning requires flushing the membrane to ensure the cleaning chemicals do not enter the water supply, creating a wastewater disposal issue. Chemical cleaning is therefore impractical to use frequently, while membranes remain prone to fouling quickly, especially with aggressive biological fouling. The prevention of fouling requires not only the modification of membrane surfaces to dissuade the seed particles or organisms from depositing on the membrane in the first place but also an investigation into other methods of cleaning which may be applied continuously or frequently. One such promising method is membrane heating, which is effective against biological foulants among others, either directly killing the micro-organisms or removing them through shear flows formed due to the heated water near the membrane surface. However, not much is known about the physical mechanisms at the nanoscale through which heating a membrane might remove a nanoparticle stuck to the membrane.

2.5 Conclusion

The investigation into the literature on the future of desalination reveals multiple significant knowledge gaps at the fundamental, molecular scale. The focus on increasing the permeability of membranes as a means of drawing down the costs of desalination appears to have hit an asymptote, where further increases in permeability result in diminishing reductions in energy usage. This necessitated a shift away from high permeability to high selectivity, bringing BNNTs to the fore as a prime membrane candidate due to their inherent charged structure which had already been shown to have high diameter dependent cation-anion selectivity. As

BNNTs come to the fore, a necessary question remains unclear in literature — how fast does water flow through them? Is it faster than CNTs or slower? The literature presents contradictory answers to this simple question. Furthermore, no studies exist which demonstrate the selectivity of BNNTs based on their high zeta potential, less so on the mechanisms through which the BNNTs might reject charged particles due to the formation of the high zeta potential. While the use of BNNTs, given the above questions are satisfactorily answered, may address the need for increased selectivity, membrane fouling remains a pervasive challenge. The use of chemicals to clean membranes is harmful to the membrane and the environment, is impractical to be used frequently or continuously and may not remove the foulants completely, leaving residues to seed future foulant growth. Dealing with fouling through periodic chemical cleaning, therefore, surrenders the membrane to sub-par desalination performance on average, as the foulant builds up and is cleaned in intermittent intervals. The use of physical cleaning methods, especially membrane heating, appear to be promising since they do not require the membrane operation to be halted. However, not much is known about the mechanisms through which heating might remove particles from the membrane at the nanoscale, therefore requiring further studies in this area.

Chapter 3

Methodology

3.1 Introduction

At very small length scales of a few nanometres, generalisations within classical fluid dynamics becomes more untenable, and other methods more suitable for this length scale are necessitated. The Monte-Carlo method was initially developed to study phenomena at this purpose. Particle-particle collisions were accounted for, but inter-atomic attraction was ignored. A need to step down further to the molecular level, where intermolecular forces are the primary forces governing the behaviour of the system under study gave rise to the method known as Molecular Dynamics (MD) (Alder and Wainwright (1959)).

Research into emerging desalination technologies is largely conducted at the nanoscale as it involves the separation of dissolved molecules from water. Constituent ions of salts, even when considered along with their hydration shells in liquid water, are barely a nanometre in diameter. At the nanoscale, the filtration of the salt particles is governed by the inter-particle electrostatic and van der Waals interactions between the salt, water and membrane atoms. These phenomena cannot be modelled using classical Computational Fluid Dynamics (CFD) or other macroscale methods, and needs the governing inter-particle forces to be accurately accounted for. Molecular dynamics, therefore, becomes the default choice for the study of such phenomena.

3.1.1 Molecular Dynamics (MD)

Similar to the use of CFD to study fluid dynamics at macroscales by making certain assumptions about physics emerging from the lower scales, classical MD seeks to study molecular systems by making certain assumptions about the nature of molecules and their constituent elements. In MD, atoms are represented as point particles, with well-defined positions and momenta. Molecules may be built from a collection of these point particles, or may be represented as a single point particle if the physics to be captured can be simulated while ignoring the multi-atom makeup of the molecule. This generalisation removes the need to simulate individual electrons which would involve solving the Schrödinger equation to obtain the probability distribution of the electron cloud as the system evolved in time. Instead, only the general effect

of such electronic interactions on the nucleus of the atom is considered and, for the simplest cases, the interaction is simplified to a spherically uniform force field that radiates outwards from the point in space where the atom exists. Classical MD also makes use of the Born-Oppenheimer approximation, i.e., that since electrons are much smaller and faster compared to the nucleus, they move instantaneously in accordance with the motion of the nucleus and therefore the forcefield can remain uniform around the nucleus in motion.

With these assumptions, the force between atoms is now dependent on only the inter-atomic distance, and therefore one-dimensional. Such a force can only be attractive or repulsive. When the atoms are closer to each other than a particular distance (which is roughly the radius of the atom), this force is strongly repulsive, but when the interatomic distance is greater than this cutoff, the force is attractive with a decreasing magnitude as the interatomic distance increases, falling to zero beyond a few nanometres. Some directionality may be introduced in multi-atom molecules, especially during the formation of chemical bonds. Numerous models have been developed to accurately replicate these forces between atoms such that the collection of atoms or molecules is able to represent a macroscopic observable - such as the contact angle of a water droplet on a given surface, or the equations of state of a given substance. This also indicates one of the limitations of MD - while it is accurate for modelling interactions between groups of atoms, since the interactions have been benchmarked on properties as a group, it does not actually represent the real interactions between individual atoms, for which quantum simulation techniques such as the Hartree-Fock (HF) and density functional theory (DFT) are better suited.

Once the force on each particle in the MD simulation has been calculated, the next steps involve updating the position and velocity of the particle, using Newton's laws of motion, under the action of that force. The force is assumed to be acting on the particle for a suitably small timestep, with the timestep usually being a few orders of magnitude lower than the timescale of the phenomenon to be studied. With the particles at their new position, the forces are calculated again and the process repeated. Smaller timesteps give more accurate dynamics of the particles but increase the computational time for the simulation. More accurate dynamics of the particles, however, does not necessarily translate to a more realistic simulation of the system - MD tries to replicate the state a group of atoms would be in, given certain starting and runtime conditions, not the exact dynamics of individual atoms. Most conditions imposed upon MD systems are drawn from macroscopic quantities - such as temperature, pressure and energy. These conditions do not uniquely define a state in the phase space of the system (i.e., the set of all possible positions and velocities which the atoms of the system might assume), instead provide a range within which the atoms can explore every state in the phase space which corresponds to the conditions imposed. A collection of all these possible states of the system, corresponding to a given set of constraints is known as an ensemble, detailed in section 3.4. The flowchart of the steps involved in an MD simulation is shown in Figure 3.1.

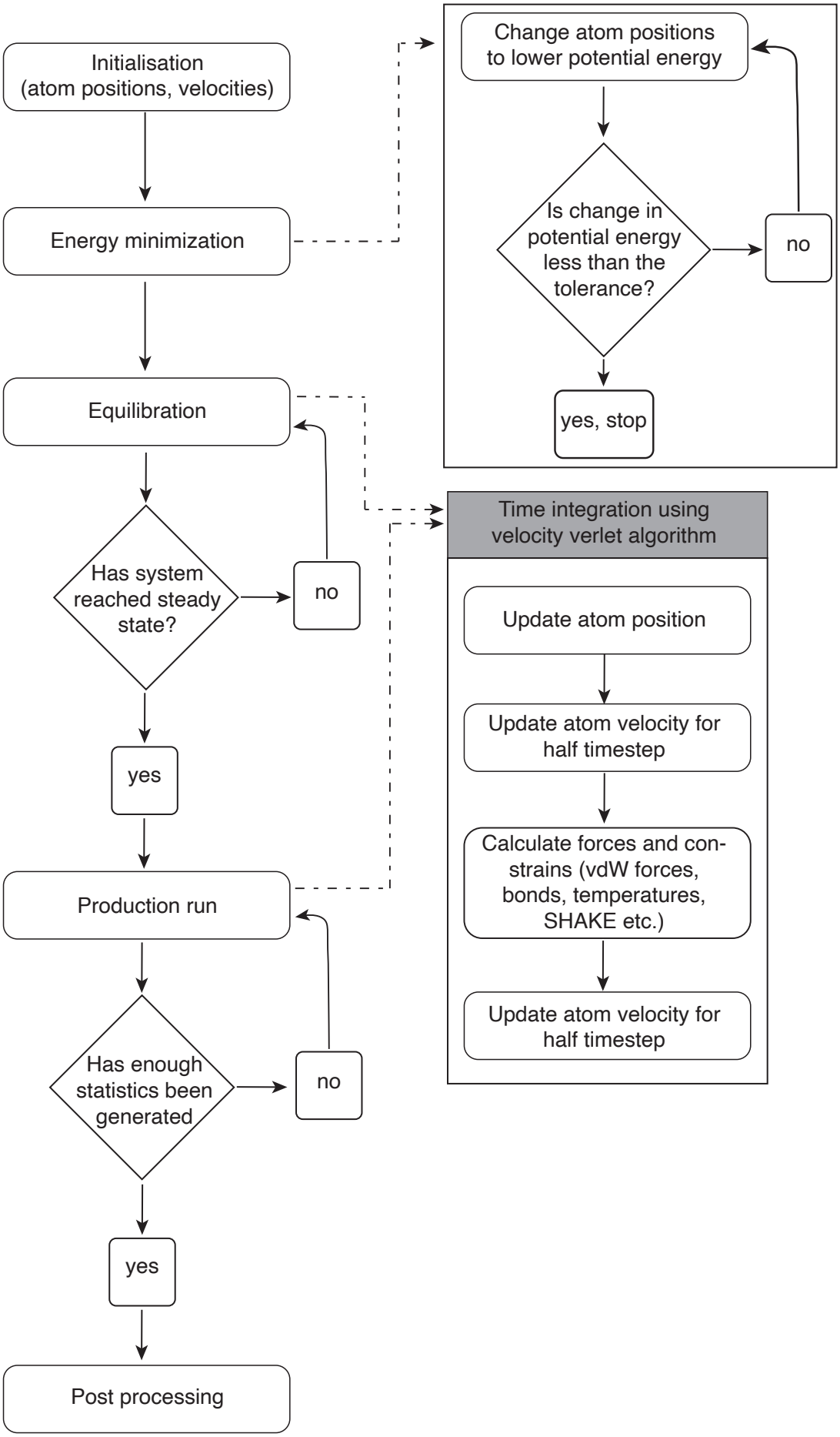

Figure 3.1: Flowchart showing the steps involved in an MD simulation.

3.2 Interatomic interactions

In MD, interatomic interactions are handled using potential models. Potential models are mathematical models to define the potential energy of a system of particles, given the location of the particles relative to each other. The gradient of the potential energy at the location of every atom then provides a measure of the net force acting on the atom, which can be used to evolve the position and velocity of the atoms in the system. Potentials can be broadly classified into pair potentials and many-body potentials. Pair potentials define the potential energy only between a pair of atoms. These potentials depend on the distance between a pair of participating atoms, instead of considering collective interaction with all the nearby atoms in the system. The total force on the atom is found by summing over the potential energy due to its interaction with all the nearby atoms, pairwise. Pair potentials are therefore unable to model properties which depend on the relative positions of multiple atoms in the neighbourhood, such as the elasticity of materials (Daw *et al.* (1993)). This is in contrast to many-body potentials, which considers the relative position of an atom with respect to the nearby atoms to estimate the force on the atom.

3.2.1 Lennard Jones potential

The Lennard Jones (LJ) potential is one of the simplest pair potentials, consisting of an attractive and repulsive term. The magnitude of the potential energy U_{LJ} depends only on the value of the distance between atoms of the interacting pair. It is formulated as follows:

$$U_{LJ}(r) = 4\varepsilon\left[\left(\frac{\sigma}{r}\right)^{12} - \left(\frac{\sigma}{r}\right)^{6}\right], \tag{3.1}$$

where r is the distance between the pair of atoms, σ is the interatomic distance at which the interatomic force turns repulsive, and ε is a measure of the strength of the interaction. The first term on the right-hand side of equation 3.1 denotes the repulsive term. When the interatomic distance is less than $2^{1/6}\sigma$, this term starts to dominate. As the ratio of σ to r is positive in Equation 3.1, its gradient is negative, implying the force imparted on the atoms is repulsive when the first term dominates. As the interatomic distance increases, the first term in Equation 3.1 goes to zero faster than the second, attractive term as it is raised to a higher power. This results in the second term dominating the potential energy at interatomic distances greater than $2^{1/6}\sigma$, and gradually going to zero at a distance of about 2σ. The choice of 12 as the exponent for the first term arises from the ease of calculation as it is simply the square of the second term. The form of the potential and the force has been plotted in Figure 3.2.

σ and ε serve as the two adjustable parameters for this model, and their values are calculated such that a collection of atoms using the determined values of σ and ε replicate some desired real-world macroscale observable.

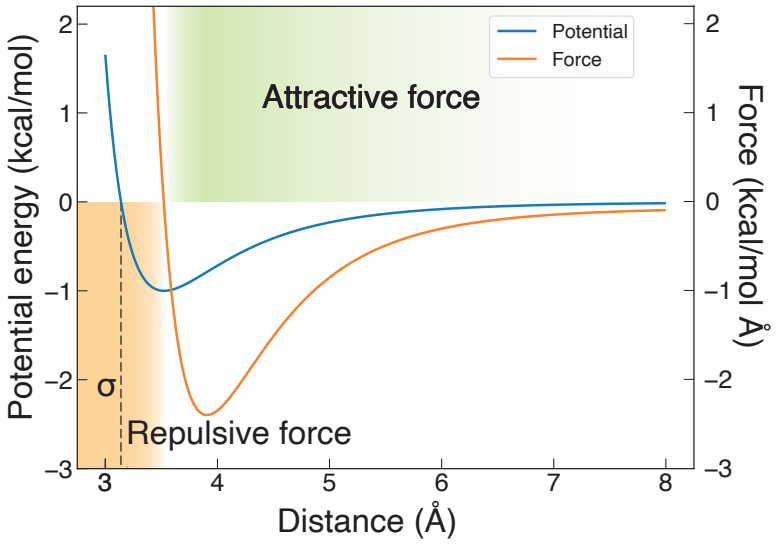

Figure 3.2: Lennard-Jones potential and forces plotted as a function of interatomic distance.

3.2.2 Harmonic potential

Harmonic potentials are used to model static chemical bonds between atoms, to constrain the position or angle between two or more atoms of a molecule. It takes the simple form of a 1-D harmonic oscillator. For bonds, it is formulated as:

$$U_{bond} = K(r - r_0)^2, \tag{3.2}$$

while for angular constraints it takes the form:

$$U_{angle} = K(\theta - \theta_0)^2, \tag{3.3}$$

where K is the spring constant set equal to the strength of the bond or angular constraint, r is the actual distance between the bond atoms, r_0 is the equilibrium distance between bond atoms, θ is the actual angle made by three non-linear atoms, and θ_0 is the equilibrium value of the angle which should be made by the atoms. Harmonic potentials are used in this study to model the O-H bonds of water molecules.

3.2.3 Spring potential

A spring potential is used to constrain an atom around a particular position with a 1-D spring. Its formulation is similar to the harmonic potential, with

$$U_{spring} = K(r - r_0)^2, \tag{3.4}$$

where K is the spring constant, r is the position of the atom at ant time t, and r_0 is the equilibrium position, i.e., point to which the atom is constrained to.

3.2.4 Electrostatic interactions

The charge which develops on atoms due to excess or lack of electrons in their valence shells is accounted for by placing the equivalent charge on the point particle representing the atom. Potential energy due to the interaction of charged atoms are accounted for using Coulomb's law. Unlike the van der Waals force which decays proportionally to $1/r^6$ and drops to zero within a few angstroms, the Coulomb force decays as with $1/r^2$ and therefore the distance over which it is non-negligible is much larger. As the radius of the sphere within which electrostatic interactions must be considered (the zone of influence) increases, the number of particles within this sphere increases $\sim r^3$, and a much larger number of interactions need to be calculated — once for each pair of atoms within the zone of influence. One of the popular ways of resolving this is to split the interactions based on distance. Interaction with charges within a small cutoff distance are computed directly, but for distances larger than the cutoff, the effect of all the charged atoms are mapped to uniform grid points and the resulting electric field is solved for. The interaction with charges outside the cutoff region is then simplified as interaction with this resultant electric field (Hockney and Eastwood (1988)). This technique of calculating electrostatic interactions is known as the Particle-Particle, Particle-Mesh (PPPM) method.

The total Coulombic energy of a system of N charged particles is given by:

$$U_{Coulomb} = \frac{1}{2}\sum_{i=1}^{N}\sum_{j\neq i}^{N}\frac{q_i q_j}{r_{ij}}, \tag{3.5}$$

where r_{ij} denotes the distance between atoms i and j and q_i, q_j the charge on atoms i and j respectively. This equation is recast (Eq. 3.6) by adding and subtracting a term from $U_{Coulomb}$ such that it consists of a short-range term (the first term), a long-range term (the second term) and a constant, self-interaction term (the third term):

$$U_{Coulomb} = \frac{1}{2}\sum_{i=1}^{N}\sum_{j\neq i}^{N}\left[\frac{q_i q_j}{r_{ij}} - \int\int\frac{\hat{\rho}_i(r)\hat{\rho}_j(r')}{|r-r'|}drdr'\right] + \frac{1}{2}\sum_{i=1}^{N}\sum_{j=1}^{N}\int\int\frac{\hat{\rho}_i(r)\hat{\rho}_j(r')}{|r-r'|} - \frac{1}{2}\sum_{i=1}^{N}\int\int\frac{\hat{\rho}_i(r)\hat{\rho}_i(r')}{|r-r'|}, \tag{3.6}$$

where $\hat{\rho}_i$ is the charge distribution around particle i. It is important to note that for interactions over small distances, the point charge assumption no longer holds, and the charge distribution around the atoms need to be considered. Assuming charge density $\hat{\rho}_i$ around the ith particle is

in the form of a Gaussian distribution centred around r_i:

$$\hat{\rho}_i(r) = q_i(G^2/\pi^3)^{3/2}\exp -G^2(r-r_i)^2, \tag{3.7}$$

where G is a parameter which determines the spread of the charge cloud and can be optimised to increase computational speed. Using the identity

$$\hat{\rho}(r) = \sum_i^N \hat{\rho}_i(r), \tag{3.8}$$

results in the final form of Equation 3.6:

$$U_{Coulomb} = \frac{1}{2}\sum_{i=1}^{N}\sum_{j\neq i}^{N}\frac{q_i q_j}{r_{ij}}\mathrm{erfc}(Gr_{ij}/\sqrt{2}) + \frac{1}{2}\int\int\frac{\hat{\rho}(r)\hat{\rho}(r')}{|r-r'|}drdr' - \frac{G}{\sqrt{2}}\sum_{i=1}^{N}q_i^2. \tag{3.9}$$

This first term accounts for short range interactions, and is computed first for the neighbouring atoms.

For the second term in Equation 3.9, the charges on particles are mapped to grid points on a 3D mesh, with $\hat{\rho}(r_p)$ representing the charge density at individual grid points. $\hat{\rho}(r_p)$ is computed for all the mesh points r_p using the equation:

$$\hat{\rho}(r_p) = \frac{1}{H}\sum_{i=1}^{N} q_i W(r_i - r_p), \tag{3.10}$$

where $W(r_i - r_p)$ is any suitable function to interpolate the charges from atom locations r_i to the mesh points r_p. Examples of such functions are presented in Hockney and Eastwood (1988). The next step is the calculation of the electric potential ϕ due to the charged grid, and this is done by solving the Poisson equation:

$$\nabla^2\phi = \hat{\rho}(r) \tag{3.11}$$

The solution to the Poisson equation is found by employing a suitable Green's function for the mesh, and is sped up by solving for ϕ in k-space using discrete Fourier transformation. Once ϕ has been calculated, the electric field E is evaluated using the relation $E = -\nabla\phi$. The resultant force on the ith particle is then

$$F_{\text{Coulomb, mesh}} = \int \hat{\rho}_i(r)E(r)dr. \tag{3.12}$$

The PPPM method is preferred over other methods such as the Ewald summation and the Coulomb cutoff method in this thesis since it scales as $\mathscr{O}(NlogN)$, compared to $\mathscr{O}(N^2)$ for Ewald summation for large systems, while also accounting for long range interactions ignored by the Coulomb cutoff method (Pollock and Glosli (1996)).

3.2.5 ReaxFF potential

While bond formation and breakage cannot be directly simulated in MD due to the lack of actual electrons, chemical reactions can be simulated by formulating the effects of the bond formation and breakage on the energy of the participating atoms. This is achieved through the assumption that the bond type and strength could be expressed as a function of the interatomic distance between the participating atoms, allowing for bond formation and creation to be expressed by energy constraints calculated using the positions of the participating atoms. The potential energy contribution from the ReaxFF potential is as follows:

$$U_{ReaxFF} = U_{bond} + U_{over} + U_{under} + U_{val} + U_{pen} + U_{tors} + U_{conj} + U_{vdW} + U_{Coulomb} \tag{3.13}$$

U_{bond} refers to the bond energy and is obtained by calculating the bond order, or the number of chemical bonds between a pair of atoms. A higher bond order indicates higher bond strength. The ReaxFF formulations assume that the bond order can be directly calculated from the interatomic distance between the pair of atoms. Bond order BO between a pair of atoms i and j is calculated using the equation:

$$BO_{ij} = exp\left[p_{bo,1}\left(\frac{r_{ij}^{\sigma}}{r_0}\right)^{p_{bo,2}}\right] + exp\left[p_{bo,3}\left(\frac{r_{ij}^{\pi}}{r_0}\right)^{p_{bo,4}}\right] + exp\left[p_{bo,5}\left(\frac{r_{ij}^{\pi\pi}}{r_0}\right)^{p_{bo,6}}\right], \tag{3.14}$$

where r_{ij} is the interatomic distance, p_{xx} represent fitting parameters and σ, π and $\pi\pi$ denote the sigma, pi and double pi bonds respectively. The parameters of the first term ($p_{bo,1}, p_{bo,2}$) account for the sigma bond, $p_{bo,3}$ and $p_{bo,4}$ account for the first π bond and $p_{bo,5}$ and $p_{bo,6}$ account for the double π bond. Adding certain corrections to the bond order detailed in Van Duin *et al.* (2001), the bond order BO_{ij} is used to calculate the bond energy as follows:

$$U_{bond} = -D_e BO_{ij} exp[p_{be,1}(1 - BO_{ij}^{p_{be,1}})], \tag{3.15}$$

where D_e represents the equilibrium potential energy of the bond and $p_{be,1}$ is a fitting parameter. U_{over} is an energy term added to ensure that the number of bonds formed for a particular atom remains at or below the valency of the atom. U_{under} takes into account the resonance effects of π electrons when the coordination number is less than the valency of the given atom. U_{val} and U_{pen} account for energy contributions due to the deviation of the three bonded atoms from the equilibrium valence angle. The equilibrium angle itself depends on the sum of π bond orders around the central atom. U_{pen} adds a penalty to the valence energy in under or over-coordinated atoms to increase the relative stability of certain kinds of double bonds. U_{tors} accounts for the energy contribution due to the torsional angle between four bonded atoms.

U_{conj} addresses the effect of conjugated bonds on the total energy. U_{vdW} is the non-bonding van der Waals interaction and replicates the effects of repulsion and attraction similar to the Lennard Jones potential. It helps smoothen sudden jumps in the system energy during bond dissociation. The ReaxFF potential uses more than 90 fitting parameters to accurately model the chemical reaction. These parameters are usually obtained using quantum methods such as those using density functional theory. A complete description of the potential terms is provided in Van Duin *et al.* (2001).

Finally, $U_{Coulomb}$ accounts for the Coulombic forces using a shielded Coulomb potential. The charges on the atoms are first calculated using the Electron Equilibration Method (EEM) which is functionally similar to the Charge Equilibration (QEq) scheme described in the next section. The ReaxFF potential was used to perform charge equilibration for boron nitride surfaces in this thesis.

3.2.6 Charge Equilibration

Charge equilibration is carried out to determine the magnitude of the partial charge on an atom in the presence of atoms of the same or different species surrounding it. This gains particular significance during bond formation and breakage, as the partial charge on the atoms change when electrons are exchanged. Charge equilibration methods can also be used to determine the partial charges of atoms for a system where these are unknown initially. In this work, the charge equilibration scheme (QEq) is used to determine the partial charges on the B, N and H atoms of hydrogenated BNNTs.

The underlying principle used in charge equilibration is the minimization of $U_{Coulomb}$, the electrostatic energy of the system, subject to the constraint that the net system charge remains zero. To this end, the energy of one atom $U_{Coulomb,i}$ due to its own charge q_i can be expressed as a Taylor series expansion:

$$U_{Coulomb,i}(q_i) = U_{Coulomb,0} + q_i\left(\frac{\partial U_{Coulomb}}{\partial q}\right) + \frac{1}{2}q_i^2\left(\frac{\partial^2 U_{Coulomb}}{\partial q^2}\right) + ... \tag{3.16}$$

The first derivative is more commonly referred to as the electronegativity χ of atom i, while the second derivative is the self-Coulomb repulsion J. Ignoring the higher-order terms, the electrostatic energy of one atom can therefore be written as:

$$U_{Coulomb,i}(q_i) = U_{Coulomb,0} + \chi_i q_i + \frac{1}{2}J_i q_i^2. \tag{3.17}$$

The energy of the entire system of charged atoms would consist of the summation of $U_{Coulomb,i}$ for all atoms along with the energy due to their interactions with each other:

$$U_{Coulomb} = \sum_i U_{Coulomb,i} + \frac{1}{2}\sum_{i\neq j} V_{ij}(r_{ij}, q_i, q_j), \tag{3.18}$$

where V_{ij} is the electrostatic energy due to the inter-atomic electrostatic interactions. Assuming the charge on atom i is distributed around the location of the atom r_i and this charge distribution of given by the function $\hat{\rho}_i(r_i, q_i)$, then V_{ij} can be expressed as:

$$V_{ij} = \int\int \frac{\hat{\rho}_i(r_1, q_i)\rho_j(r_2, q_j)}{r_{12}} dr_1 dr_2. \tag{3.19}$$

The electrostatic energy of a system of charged atoms can be expressed as

$$U_{Coulomb} = \sum_i \chi_i q_i + \frac{1}{2}\sum_i J_i q_i^2 + \sum_{(i,j)} \int\int \frac{\hat{\rho}_i(r_1, q_i)\hat{\rho}_j(r_2, q_j)}{r_{12}} dr_1 dr_2. \tag{3.20}$$

$\hat{\rho}_i$ can be modelled by using slater-type orbitals, which are spherical and without any radial lobes, as was done previously in section 3.2.4. $\hat{\rho}_i$ is defined as:

$$\hat{\rho}_i(r, q_i) = (q_i \zeta_i^3/\pi) \exp(-2\zeta_i |r - r_i|). \tag{3.21}$$

At every timestep, the partial charges (q_is) are determined by minimizing $U_{Coulomb}$ while ensuring that the system as a whole remains charge neutral, i.e. $\sum_i q_i = 0$. Using the same operations as outlined in section 3.2.4, equation 3.20 is recast into short and long-range components. The determination of q_i's turns into a constrained minimization problem which is solved using a Conjugate Gradient method. Therefore, given the initial inputs of the atoms positions, electronegativities, self-Coulomb repulsions and valencies, the partial charge for the system of atoms can be evolved alongside the evolution of the atomic trajectories. The complete set of equations describing the charge equilibration process can be found in Rappé and Goddard (1991).

3.3 Time integration

Once the interatomic forces have been defined for an MD setup, the atoms are then moved under the influence of these forces. As the atoms move, the interatomic distance-dependent forces change, requiring a recalculation of the forces, followed by a subsequent update of the atom velocities and finally atom positions, based on the new velocities. While a real system would have the forces, positions and velocities changing continuously and simultaneously, this is not possible in a numerical method like MD. MD uses finite difference methods (FDM) to solve for the atom positions and velocities with time, and the use of FDM for MD necessitates discretization of time. This discretization allows for the forces to be calculated at a given timestep. Atom positions are then updated under the influence of the calculated force with the assumption that the force remains constant for the duration of the timestep. Smaller timesteps, therefore, result in a faithful representation of the Newtonian trajectory of the atoms, but at the cost of increased computational time.

The exact algorithm used for the integration of the equations of motion is known as the velocity-Verlet algorithm, first described in Verlet (1967). As outlined in section 3.1.1, atoms in an MD simulation are modelled as point particles following Newton's equations of motion, therefore,

$$m\ddot{r}(t) = f(t), \tag{3.22}$$

where m is the atom mass, r is atom position, f is the force on the atom and t is the current time. Representing the timestep with Δt, the velocity-Verlet algorithm updates position and velocities as follows:

$$\dot{r}(t+0.5\Delta t) = \dot{r}(t) + 0.5\ddot{r}(t)\Delta t, \tag{3.23}$$

$$r(t+\Delta t) = r(t) + \dot{r}(t+0.5\Delta t)\Delta t, \tag{3.24}$$

$$m\ddot{r}(t+\Delta t) = -\frac{\partial U}{\partial r}\bigg|_{r(t+\Delta t)} = f(t+\Delta t), \tag{3.25}$$

$$\dot{r}(t+\Delta t) = \dot{r}(t+0.5\Delta t) + 0.5\ddot{r}(t+\Delta t)\Delta t. \tag{3.26}$$

The velocity-Verlet algorithm updates the atom position for the full time step, but the velocities are incremented in half timesteps. The half step allows this algorithm to have a global error of the order of Δt^2. A typical timestep used in this thesis is 2 femtoseconds (fs), or 2×10^{-15} seconds.

3.4 Thermodynamic ensembles

As mentioned in section 3.1.1, when simulating real systems, only the macroscopic state of the system is usually known, quantified using parameters such as temperature, pressure, volume and energy. These macroscopic parameters alone are insufficient to provide the velocity and position of every atom in the system to uniquely determine the system. Many different, unique combinations of atom positions and velocities can correspond to the same value of the macroscopic parameters. Any unique combination of velocities and positions of a system of particles is known as a microstate. A collection of microstates which corresponds to some given values of the macroscopic parameters is known as an ensemble. The macroscopic parameters are commonly grouped together to represent various kinds of experimental conditions. Some of these are:

Microcanonical ensemble:

The microcanonical ensemble refers to a system that is completely isolated from the outside environment. It cannot exchange any energy or particles with the outside environment, and therefore the number of particles and the total energy of the system remains constant. This is also known as the NVE ensemble, referring to the constant values of the number of particles (N), the volume of the system (V), and the energy of the system (E). The probability of each

microstate is given $P = 1/W$, where W is the total number of microstates for the given energy. The LAMMPS implementation of the NVE ensemble using the command 'fix nve' does not ensure the conservation of these values irrespective of other constraints applied. Instead, it simply evolves the particle trajectories following Newton's laws of motion, which implicitly results in the conservation of energy in the absence of other constraints and energy inputs.

Canonical ensemble:

The canonical ensemble refers to a system where the number of particles (N), volume (V) and temperature (T) remains constant, akin to a closed system connected to a heat bath. The energy of the system, however, is not kept constant, with energy added or subtracted in a manner to ensure that the microstate of the system i.e., the combinations of particle positions and velocities, corresponds to the distribution expected in a heat bath at the given temperature. The probability of each of the microstates corresponding to an energy E is given by:

$$P = e^{\frac{F-E}{kT}}, \tag{3.27}$$

where F is the Helmholtz free energy and k is the boltzmann constant. An NVT ensemble, therefore, conserves F and allows E to vary.

Isobaric-Isothermal ensemble:

In this ensemble, alongside the number of particles and temperature, the pressure (P) is also held constant. Also known as the NPT ensemble, simulation of a system in this ensemble is akin to immersing the system in a heat bath held at constant pressure. The pressure of the system is adjusted by varying the system volume and rescaling the particle positions to the new volume.

Other ensembles include the grand canonical ensemble, which maintains the chemical potential (μ) alongside the volume and temperature, and the isoenthalpic-isobaric ensemble, which maintains constant pressure and enthalpy. These ensembles are described in detail in the book by Frenkel and Smit (2002), but are not used in this thesis.

3.4.1 Thermostats

Thermostats are algorithms used to simulate the system under study, or parts of it, being coupled to a very large heat bath such that it maintains a constant temperature. Thermostats vary depending on the kind of physics they try to implement - simple rescaling of the velocities provides numerically constant temperatures, but are unphysical as a real system having a certain temperature would have a distribution of states which conforms to the canonical ensemble. Nose-Hoover thermostats attempt to replicate the canonical ensemble, and are therefore more computationally intensive than simple thermostats such as velocity rescaling or Berendsen thermostats.

Berendsen thermostat

The Berendsen thermostat attempts to control the temperature of a system by adding a friction term and a stochastic term to the equations of motion, such that equation 3.22 is modified to

$$m\ddot{r}(t) = f(t) - \gamma\dot{r}(t) + R(t), \tag{3.28}$$

where γ is an adjustable parameter representing the strength of the coupling with the heat bath, and $R(t)$ is the random force component. This can be simplified to obtain atom velocity in the subsequent timestep based on the current velocity as

$$\dot{r}(t+\Delta t) = \lambda\dot{r}(t), \tag{3.29}$$

with λ defined as:

$$\lambda = 1 + \frac{\Delta t}{2\tau_T}\left(\frac{T_0}{T} - 1\right). \tag{3.30}$$

Here, T_0 is the temperature of the heat bath (the target temperature) and T is the current temperature of the system. τ_T is the time constant of the coupling, provided as an input to the simulation. The atom velocities are therefore scaled proportionally to their deviation from the target temperature. Details of the transformation from equation 3.28 to 3.29 are provided in Berendsen *et al.* (1984). While this simple rescaling scheme is computationally cheap, it does not represent any particular ensemble, as noted by its authors (Berendsen *et al.* (1984)).

Nosé-Hoover thermostat

The Nosé-Hoover thermostat attempts to recreate the canonical ensemble with the group of atoms on which it is applied. It modifies the equations of motion by adding an extra degree of freedom to the particles which represents the thermostat. The equations of motion are modified as follows:

$$m\frac{d^2r'(t)}{dt'^2} = f(t) - sp'_s\frac{m}{Q}\frac{dr'}{dt'} \tag{3.31}$$

where r' and t' represent position and time scaled by the variable s which represents the extra degree of freedom accorded by the thermostat. p'_s represents the scaled momentum of the thermostat, and Q represents the mass of the thermostat. Nosé (1984) has shown how this formulation leads to the creation of a canonical ensemble. The exact formulation used in LAMMPS can be found in Shinoda *et al.* (2004).

3.5 Periodic boundary conditions

When a portion of a large system is replicated within a finite domain, as is often the case in MD, boundary conditions must account for the interactions of this finite-sized system with the larger entity. Periodic boundary conditions is one such method of accounting for these interactions. It follows from the simple assumption that the larger entity is formed by infinite repeated images of the portion under study. This allows for small systems to represent infinitely large systems without explicitly accounting for an infinite number of particles.

The method of periodic boundary conditions is illustrated in Figure 3.3. As a particle i begins to cross the periodic boundary to leave the finite domain, the assumption of images implies that the periodic image of i, i.e. i', also starts crossing the periodic boundary on the other side to leave the image domain and enter the finite domain. In practice, the particle leaving the periodic boundary is simply wrapped around to the opposite periodic boundary and re-introduced into the finite domain. This also implies that periodic boundary conditions have to be implemented over the entire dimension, unlike other boundary conditions such as reflective walls which can be implemented on only one side of the system. Since the number of particles entering the finite domain is equal to the number of particles leaving, the number of particles in the simulation is conserved. This is helpful in the simulation of flowing fluids, as particles need not be explicitly added and removed to maintain upstream and downstream densities. The particle velocities are also preserved when a particle crosses the periodic boundary, conserving linear momentum. Since the relative positions of the particles are conserved across the periodic boundary, the potential energy of the system is also conserved.

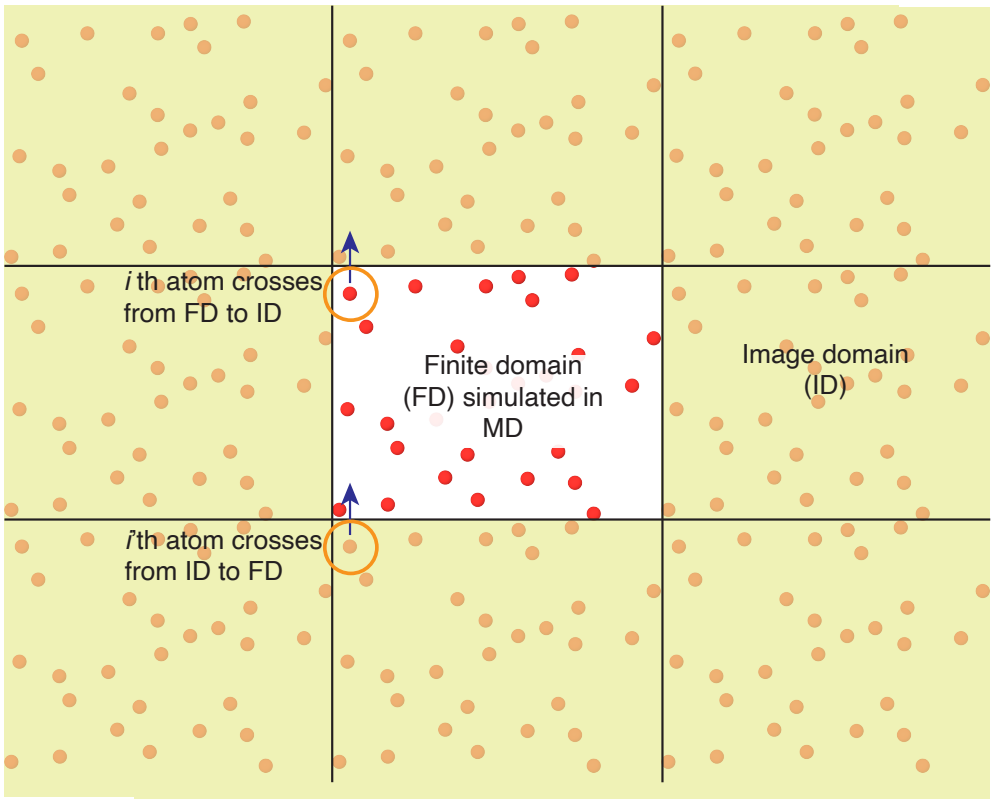

Figure 3.3: Periodic boundary conditions to replicate a large system using images of the system under study.

3.6 Atomic models

3.6.1 TIP4P/2005 water

Water models are a set of relative atom positions and interaction parameters that have been optimized such that simulating water molecules using these models will replicate the properties of water for which the model has been optimized. TIP4P is one such widely used water model, first introduced in 1933 (Bernal and Fowler (1933)), parametrized in 1983 (Jorgensen *et al.* (1983)) and re-parametrised in 2005 (Abascal and Vega (2005)).

The TIP4P/2005 model consists of two hydrogen atoms attached to an oxygen atom at a fixed angle. Positive partial charges which arise on the hydrogen atoms are placed on the location of the hydrogen atoms, but the negative partial charge attributable to the oxygen atom is placed some distance away from the oxygen atom on the angular bisector of the angle formed by the two hydrogen and oxygen atoms. This massless, negative charge site makes TIP4P/2005 a four-site model. The shifting of the negative charge closer to the hydrogen atoms was carried out to improve the phase diagram of the water model (Abascal and Vega (2005)). The model is depicted in Figure 3.4, while the model parameters are presented in Table 3.1.

Parameter	Value
ε/K	93.2 K
σ	3.1589 Å
q_H	0.5564e
q_M	-1.1128e
d_{OM}	0.1546 Å
d_{OH}	0.9572 Å
$\angle$ HOH	104.52°

Table 3.1: TIP4P/2005 parameters. q_H and q_M stand for the charge on hydrogen and the massless charge, respectively. d_{OM} and d_{OH} stand for the oxygen-massless charge and oxygen-hydrogen distance respectively. $\angle$ HOH is the H-O-H bond angle.

3.6.2 SHAKE

The hydrogen atoms of a water molecule have a natural frequency such that direct simulation of dynamics would require timesteps of 0.5 fs, in contrast to the 2 fs used widely in this thesis. This would severely increase the computational time any simulation would need to run, with the resulting gains in accuracy being inconsequential for the parameters under study, largely the flow rate of water through small channels. To overcome this, the hydrogen-oxygen covalent bond is treated as rigid, with the bond length and bond angles fixed. This constraint on the bonds is applied using the SHAKE algorithm (Ryckaert *et al.* (1977)).

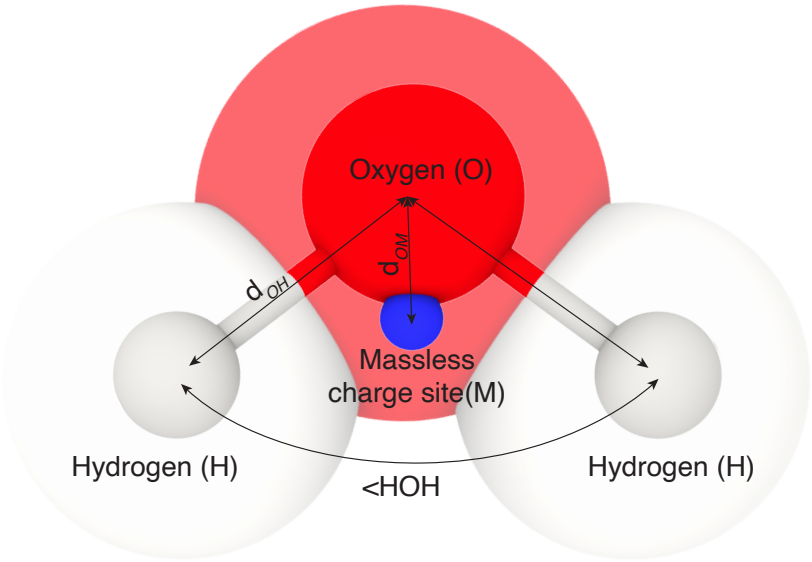

Figure 3.4: TIP4P/2005 water model

The constraint is applied as an extra force on the H atoms during the time integration step such that the position of the H atoms satisfy the bond constraint at the next timestep to a given degree of tolerance. The equations of motion is modified to this end as:

$$m\ddot{r} = f[r(t)] + g[r(t)], \tag{3.32}$$

$$g[r(t)] = -\sum_{k=1}^{l} \lambda_k \nabla \sigma_k, \tag{3.33}$$

$$\sigma_k = (r_j(t) - r_i(t))^2 - d_{ij}^2 = 0, \tag{3.34}$$

where r_i, r_j is the positions of the ith and jth constrained atoms, f is the force due to the interatomic interactions and g is the force from the l different constraints, σ_k. λ_k are the time-dependant Lagrange multipliers of the constraints. d_{ij} is the equilibrium bond length. The constraint force g is found using an iterative procedure, where an initial value for g is chosen, following which the atom position is updated. If the updated position differs by the length or angular constraints by more than the tolerance, then the value of g is updated proportionally to the square of the difference between the actual bond length and the constraint, and the atom position recalculated. Detailed equations for the calculation of g are provided in Andersen (1983).

3.7 Runtime controls

3.7.1 Pressure control

For all simulations in this study that had water reservoirs, the flow was simulated by controlling the pressure on the upstream and downstream reservoirs. This pressure control was achieved using two distinct methods depending on the needs of the specific system: by adding a fixed force to a specified region within the reservoirs, and by modelling a piston at the end of the reservoir which exerted a force on the water molecules to reproduce the desired pressure. The linearity of the relation between the pressure drop and the mass flow rate is ensured for all simulations.

Periodic pumping:

Force is applied on the oxygen atoms in the regions of the reservoir depicted by Figure 3.5. This force is in addition to the force felt by the oxygen atoms due to interatomic interactions. The magnitude of the applied force is calculated using

$$F = \frac{1}{\rho_n}\frac{\Delta P}{L}, \tag{3.35}$$

where F is the per-particle force, ρ_n is the number density of the water molecules, ΔP is the desired pressure drop, and L is the length over which the pressure drop is to be applied. The choice of the forcing area creates a sharp pressure rise in the reservoirs across the periodic boundary, which is used to sustain the pressure drop in the section of the system under study, creating a closed system. Since both reservoirs are connected through the tube and the periodic boundary, using this form of pressure control does not impose any constraint on the duration of the simulation run, as the reservoirs are filled and depleted simultaneously. Periodic pumping is therefore preferred for simulations which need to be run for a long time, and the chemical composition of both the reservoirs are the same.

Piston based pressure control:

Pistons are used on the free ends of the reservoirs to impose the desired pressure, as shown in

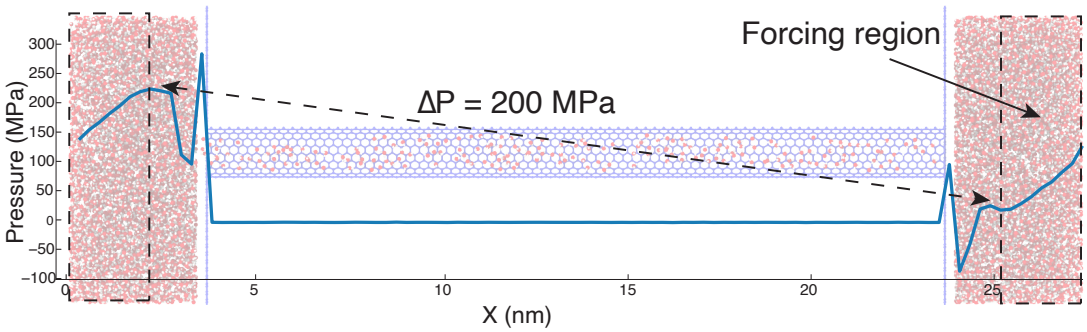

Figure 3.5: Pressure control using direct addition of force to water.

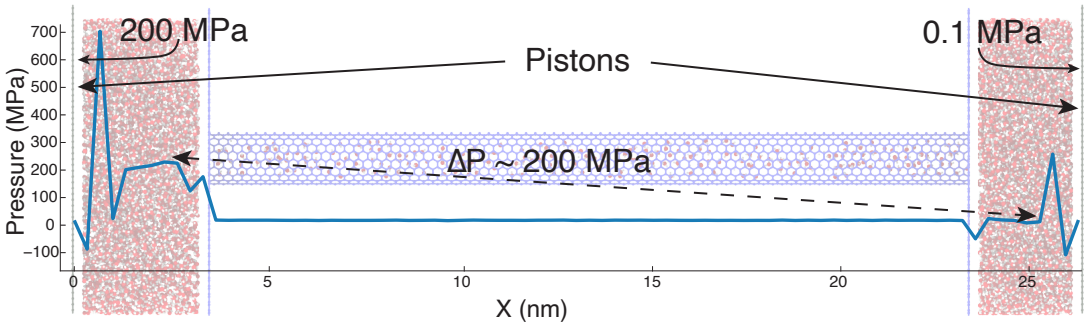

Figure 3.6: Pressure control using pistons. Simulation domain and pressure chart has some misalignment as the pistons move during the course of the simulation.

Figure 3.6. The pistons are treated as rigid bodies. The force felt by the atoms of the piston due to interatomic interactions is averaged and reapplied uniformly to all the atoms in the piston, in addition to the extra force which sets up the pressure. The force to be added to each piston atom for setting the pressure is

$$F = \frac{PA}{N}, \tag{3.36}$$

where P is the magnitude of the pressure to be applied, A is the cross-sectional area of the piston and N is the number of atoms on the piston. Pressure differences to create flow is set up by applying two different pressures on the upstream and downstream pistons. Using pistons allows better control of the absolute pressure within the reservoirs. This method is particularly useful when the upstream and downstream reservoirs need to maintain differences other than the pressure, such as for temperatures, or dissolved salts on one side, which are difficult to ensure if the reservoirs are attached through the periodic boundary. This, however, limits the duration for which simulations may be run since the upstream reservoir is depleted within a finite time. Piston based pressure control is preferred where both reservoirs need to maintain different properties, such as different ionic strengths.

3.7.2 Parallel optimisation

MD uses many particles largely interacting with each other through short-range interactions, a technique that easily lends itself to scaling up using multiple processors. Atoms of the system are distributed to each of the processors based on some predetermined scheme, usually by dividing the simulation domain into bins and assigning all atoms within a bin to a processor. Where the number of atoms within the simulation varies with time and/or space, this might lead to conditions where a few processors handle a large number of atoms, while the remaining processors stay idle. This would lead to a slowdown of the simulation and a wastage of computational resources. To avoid this, the volumetric domain assigned to each processor was optimized after every 50000 timesteps in all the simulations using the ‘fix balance’ inbuilt within LAMMPS. The binning of space is dependent on two quantities - the average number

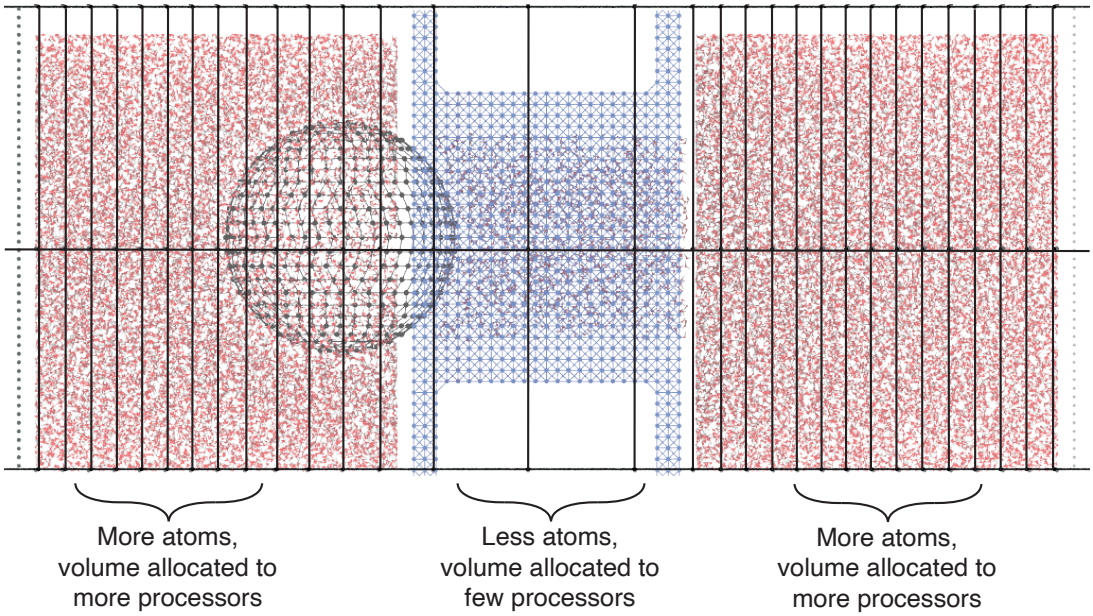

Figure 3.7: Sample domain decomposition to optimize the number of atoms in each processor. Shown here is a simulation setup of a particle stuck in a membrane pore, described in section 6.3.

of atoms per processor, and the ratio of the number of atoms held by one processor to the average. The ratio is known as the imbalance ratio, and it was set to not exceed 1.05 in the simulations. A sample binning scheme is shown in Figure 3.7, which shows smaller bins where atom concentration is high, and larger bins where atom concentration is low.

3.7.3 Energy minimization

The configuration in which the MD simulation is started on the first timestep might not necessarily be close to any physical setup. This is likely if atoms are initialized very close to each other, which would result in very high forces, leading to atoms crossing the domain bins of multiple processors within one timestep and the algorithm losing track of such atoms. To a lesser extent, it might also lead to bond breakage, and use up computational time till the system relaxes to a more physical state. To avoid this, simulations are energy minimized before the start of the actual MD itself. Typically, this is done by changing the atom positions and velocities using certain algorithms such that the system can sample an amount of the available phase space and determine a configuration that results in a local minimum of energy. A local minimum is assumed to have been achieved when further changes in the atom positions and velocities results in a change of the total system energy less than a specified tolerance. The algorithm used in this work is the 'FIRE' style of minimization, described in Bitzek *et al.* (2006).

3.8 Post processing

3.8.1 Mass flow rate measurement

Mass flow measurements can be carried out using several methods, including measuring the velocity of the fluid atoms in the direction of interest at every timestep, tracking the number of atoms that cross from one side to another and recording the changes in the number of atoms between locations upstream and downstream of some desired section.

While measuring the average velocity of atoms in the flow direction is the most straightforward way of calculating the mass flow rate - requiring the least number of computational steps, atomic velocities are inherently very noisy. The thermal velocities of water molecules is much larger than the flow velocity expected inside the nanotube. This introduces a large error in the mass flow measurement, even when averaged over long times. One way to improve the accuracy of methods depending on the atom velocities is to use block averaging, where the entire time series velocity data is divided into several blocks whose averages are calculated. The standard deviation is then measured from the deviation of the block averages from the mean value averaged from all the block averages (see Figure 3.8).

Methods of measuring flow rates which depend on counting the number of molecules are also affected by the presence of thermal velocities, depending on the expected mass flow rate. A mass flow rate of the order of 10^{-15} kg/s, commonly observed in the simulations would produce a flux of 0.03 water molecules in 1000 fs, compared to the fluctuations of a few molecules every 1000 fs. Two types of mass flow measurement methods which depend on counting the number of water molecules were used for this study. The first method was applied to a system that had a non-periodic reservoir. The mass flow rate was estimated by calculating the change in the number of molecules in the upstream and downstream reservoirs against time and then taking an average of the two values (see Figure 3.9).

The second method involves counting the number of times a water molecule crossed a fixed plane at the centre of the simulation setup. For this method, the water molecules are first arranged in ascending order from the LAMMPS dump files. A virtual plane, for this case the centre of the simulation box in the axial direction is selected. For the first timestep, water molecules are tagged as being either on the left or the right of this virtual plane. For the subsequent timesteps, the value of the flux is incremented by 1 for every molecule crossing from the upstream to the downstream direction, and decremented by 1 when the molecule travels in the opposite direction. This flux data, computed at every timestep present in the dump file, is then divided into a minimum of three blocks, and then the average and standard deviation are calculated between the blocks to estimate the standard deviation in the mass flow rate (see Figure 3.10).

Block averaging is used to determine a more accurate estimate of the error from the mass flow measurements. This is done by dividing the time series data into several blocks, then calculating

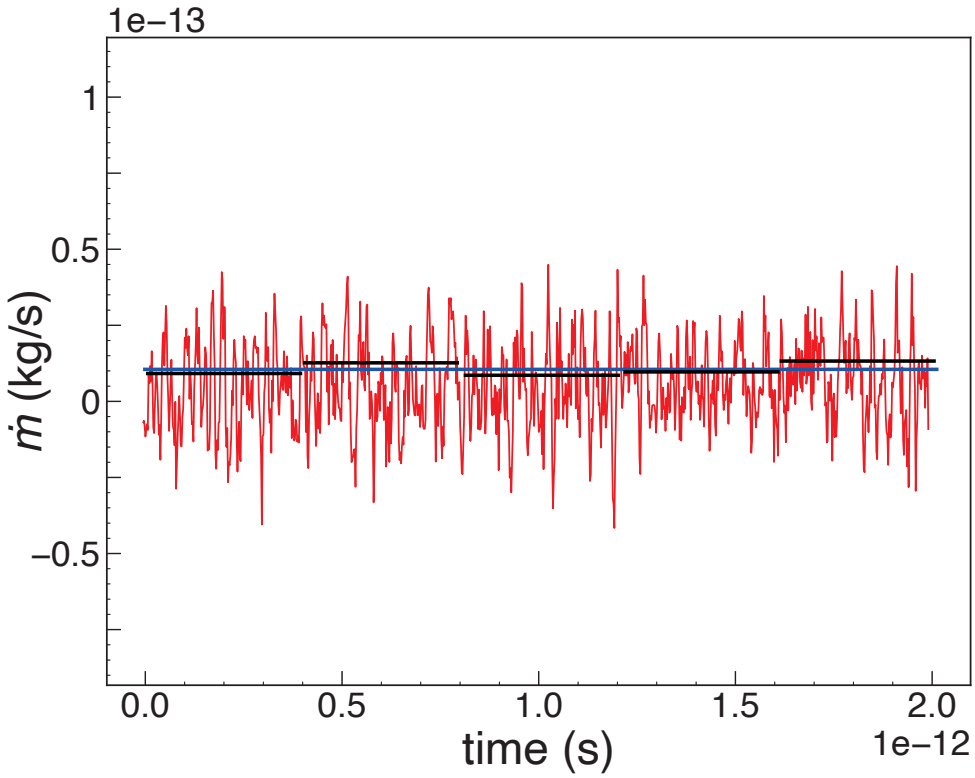

Figure 3.8: Mass flow rate determined using atom velocities. Black lines represent block averages

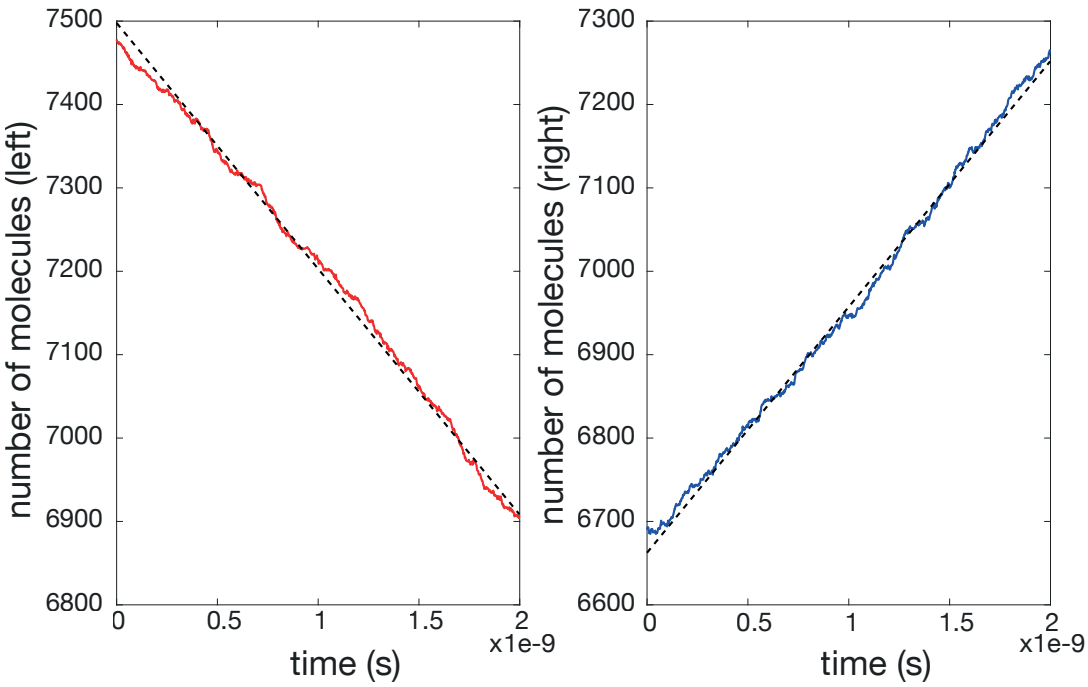

Figure 3.9: Change in the number of atoms in each reservoir used to estimate the mass flow rate. Dashed line shows linear fit to data.

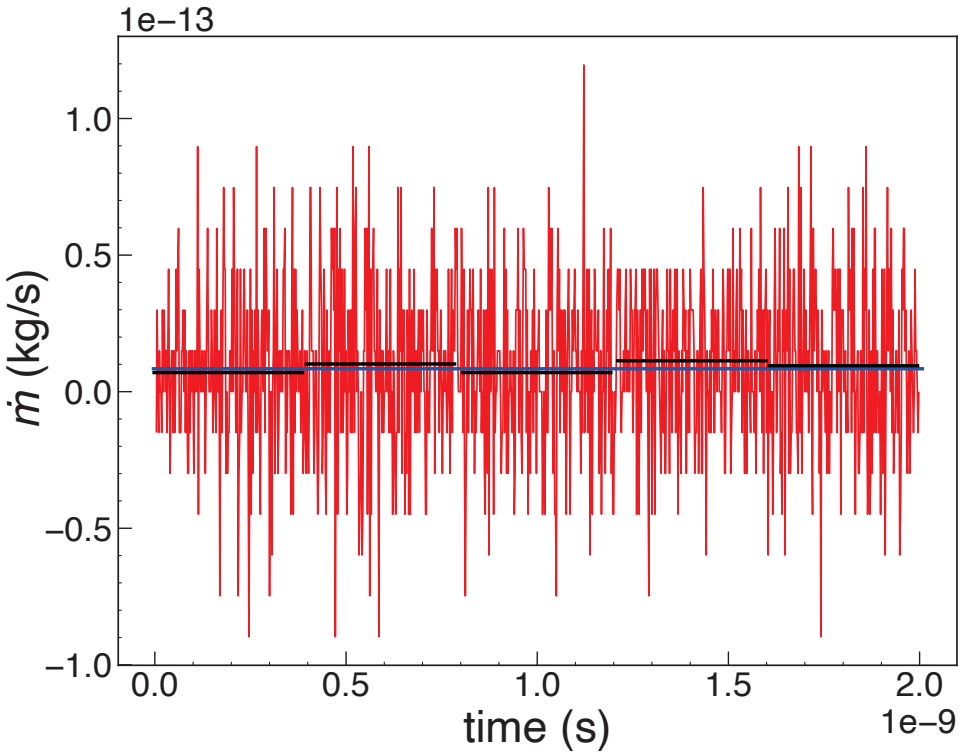

Figure 3.10: Estimation of mass flow rate by counting the number of atoms crossing a central plane. Black lines represent block averages.

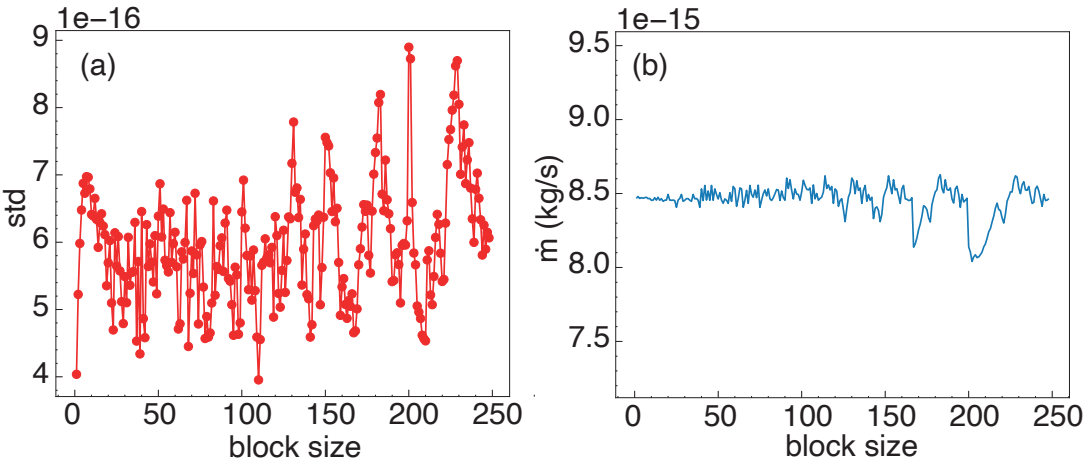

Figure 3.11: (a) Change in standard deviation with block size. (b) Change in mean with block size.

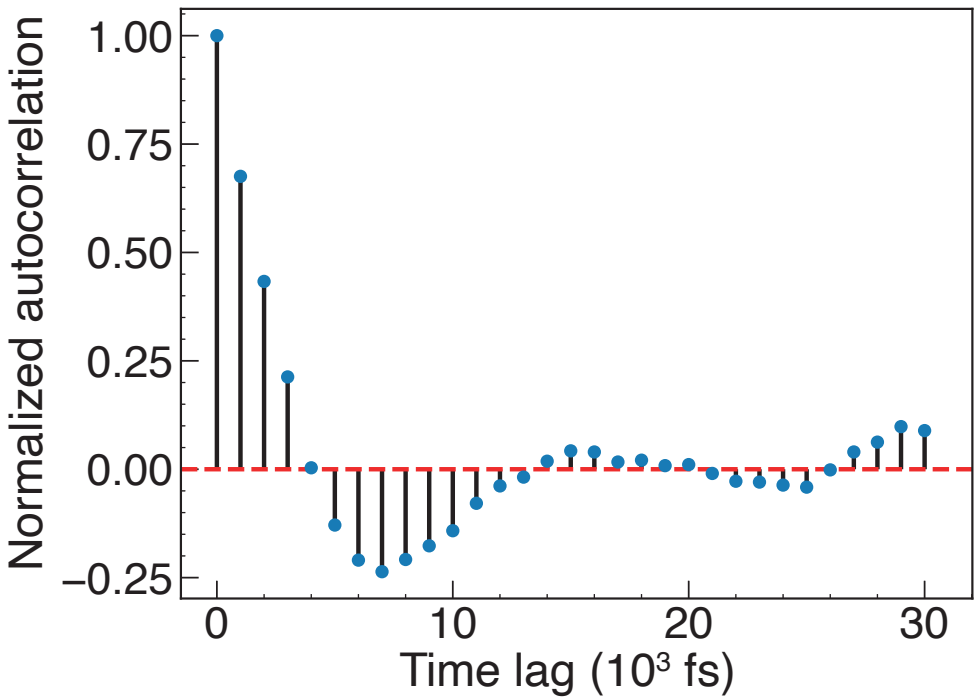

Figure 3.12: Autocorrelation function of the mass flow rate.

the average of each of the blocks, similar to resampling techniques to estimate the error. Block averaging is particularly useful when the time series data is correlated and the effects of this correlation need to be removed from the error calculations. To do this, the minimum block size must be greater than the correlation length. On the upper end, a larger block size reduces the total number of blocks, and the mean value starts fluctuating as the block size approaches the length of the time-series data. In Figure 3.11, the change in the mean and standard deviation of the mass flow rate from the velocity method is presented against the block size. Figure 3.12 shows the correlation length of the mass flow rate data, indicating, for this particular case, a minimum block size of greater than 20 would be ideal to remove noise from correlations.

3.8.2 Measurement of fluid properties

This section describes the methods used to determine the pressure, temperature, density and stress in the simulated fluids. All the aforementioned quantities are evaluated within bins formed by the spatial division of the simulation domain.

Pressure: Pressure was measured by summing up the principal terms of the per-atom stress tensor, then averaging it over all the atoms present in the bin. The per-atomic stress tensor is defined as:

$$s_{ab} = -m\dot{r}_a\dot{r}_b - w_{ab}, \tag{3.37}$$

where a, b represent the dimensions x, y and z, m is the atom mass and $\dot{r}_a$ is the atom velocity in the a direction. The first term represents the contribution of the kinetic energy to the per-atom stress, while the second term is the virial term, representing the contribution of the interatomic interactions between the atom and other atoms in its vicinity. The virial term is calculated as follows:

$$w_{ab} = \underbrace{\frac{1}{2}\sum_{n=1}^{N_p}(r_{1a}F_{1b} + r_{2a}F_{2b})}_{\text{van der Waals contribution}} + \underbrace{\frac{1}{2}\sum_{n=1}^{N_b}(r_{1a}F_{1b} + r_{2a}F_{2b})}_{\text{Bond contribution}} + \underbrace{\frac{1}{2}\sum_{n=1}^{N_a}(r_{1a}F_{1b} + r_{2a}F_{2b} + r_{3a}F_{3b})}_{\text{angle contribution}} + Kspace + Fixes, \tag{3.38}$$

where r_1 denotes position of an atom, r_2 the position of the other atom interacting with this atom in a pairwise manner and r_3 the third atom which makes up an angle. F_{Ix} represents force on the atom I in the x direction. N_p, N_b and N_a refer to the number of neighbours, bonded neighbours and angles which the atom forms with its neighbours respectively. Kspace interactions include long range forces such as the Coulombic force coming from the PPPM method. Fixes such as SHAKE outlined in section 3.6.2 also contribute to the virial term. The per-atom stress is formulated in the units of energy as the definition of the volume of an atom, necessary to divide the energy to convert it to the units of stress, is ambiguous. The pressure is calculated as:

$$P = -\frac{1}{3V}(S_{xx} + S_{yy} + S_{zz}), \tag{3.39}$$

where $S_{aa} = \sum^N s_{aa}$, the sum of the per-atomic stress tensor for all N atoms within the bin and V is the bin volume.

Temperature: Temperature is measured using the formulation

$$\textit{total kinetic energy} = \frac{1}{2}\sum_{i=0}^{N} m_i \dot{r}_i^2 = \frac{dim}{2}NkT \tag{3.40}$$

where $m_i, \dot{r}_i$ are the mass and velocity of the ith atom, N the total number of atoms in the subset of atoms whose temperature is to be calculated, k the Boltzmann constant and dim the dimensionality of the simulation. When used in a 3-dimensional system in conjunction with the SHAKE algorithm defined in section 3.6.2, the dimensionality is reduced by one since the degrees of freedom available to the atoms are restrained.

Potential energy surface: The potential energy surface is measured in three separate ways depending on whether the energy of interest is the interaction energy with a single atom or a large molecule constituted of several atoms.

For interactions with one atom, a virtual, 3-dimensional grid with a spacing of 0.1 Å is created over the solid surface of interest, extending to the short-range interaction cutoff distance.

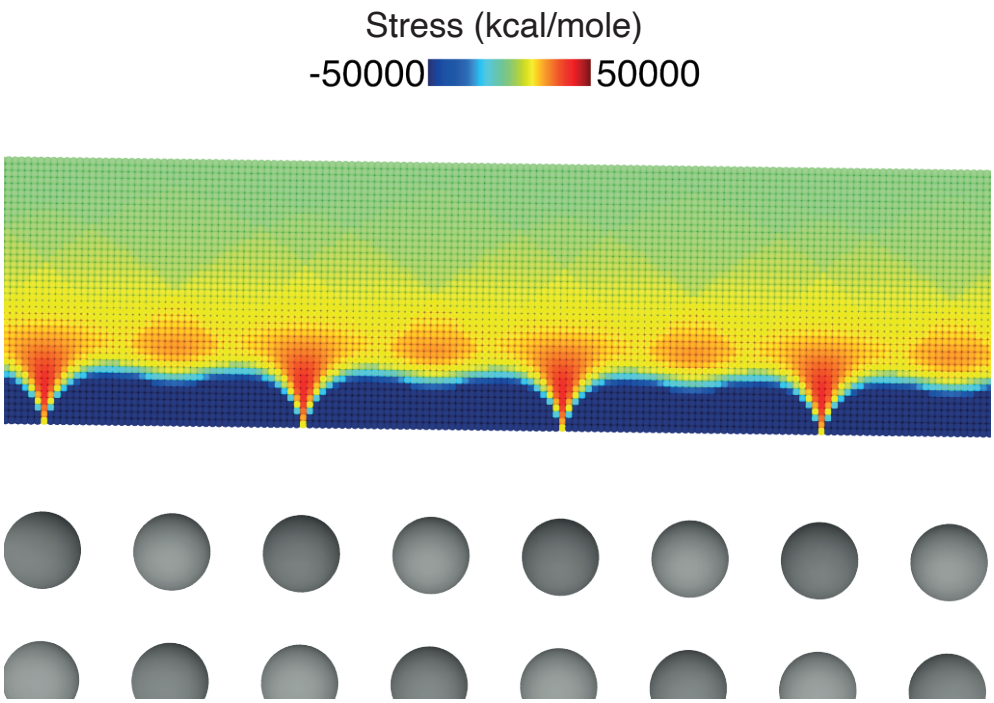

Figure 3.13: Measurement of potential energy surface using grid of atoms placed over the solid surface. The grey atoms represent the solid surface whose potential energy as a function of position above it is being measured. The coloured points represent the interaction strength at their respective positions.

This grid is then populated with atoms of the type whose interaction with the surface is to be calculated, as shown in Figure 3.13. Self-interactions between the atoms on the grid and those constituting the solid surface are turned off, and only the grid-surface atom interactions are retained. Per-atom energy and forces from this setup is then calculated using LAMMPS, and then linearly interpolated in post-processing to generate the potential energy distribution within the given space above the solid surface. For liquid-solid interactions, the potential energy surface is usually calculated at the first density peak of the liquid layer next to the surface, and this is extracted from the volume in which the potential energy was calculated.

A second method is used when a long simulation run modelling the atom-surface interaction already exists. The rerun command within LAMMPS is used to recalculate the interaction energy in the space over the surface, with self-interactions ignored.

In the third method, where the interaction is with a large molecule, the molecule is artificially moved in the 3-dimensional grid of points over the surface of interest and the total energy and force arising from the surface-molecule interaction are summed over all atoms in the molecule. This method is only applicable when the particle is a large spherical particle such that its interaction with the surface is invariant with its orientation.

3.9 Summary

This chapter presents the varying length and timescales of physical phenomena and establishes the unique position of the molecular dynamics method in simulating these phenomena. It lays out the necessity and applicability of MD in the study of the physics of nanoscale membranes. The inner workings of the MD method are described, starting from the assumption of atoms as point particles. The various potentials used to model the short-range interactions between the atoms are described, as are the long-range Coulombic interactions. The algorithm used to evolve the atoms under the action of interatomic and other forces is presented. A discussion is provided on the link between real-world experimental constraints and molecular ensembles, and the implementation of these ensembles in MD through the use of thermostats. Finally, the various techniques used for analysing the results obtained from the MD simulations, primarily the mass flow rate, and methods to reduce noise from the obtained results are discussed.

Chapter 4

Untangling the physics of water transport in boron nitride nanotubes

This chapter has been published in: Mistry, S., Pillai, R., Mattia, D., and Borg, M. K. "Untangling the physics of water transport in boron nitride nanotubes". *Nanoscale*, 13(43):18096–18102, 2021.

This chapter focusses on analysing water flow through boron nitride and carbon nanotubes, comparing simulations against experimental data and other results available in literature. Contradictory claims found in literature of BNNTs being better or worse than CNTs in the transport of water is addressed, and a framework is laid out for more accurate comparisons of studies of flows through nanotubes across both simulations and experiments.

4.1 Introduction

Literature of water flow through BNNT and CNT membranes often report divergent claims, with similar numbers of studies suggesting BNNTs conduct water faster than CNTs and vice-versa. Studies by Hilder *et al.* (2009a); Liang *et al.* (2017); Suk *et al.* (2008); Won and Aluru (2007) and Azamat *et al.* (2016) suggest higher water flows through BNNTs, while other studies by Ritos *et al.* (2014); Sam *et al.* (2018); Wei and Luo (2018) and Secchi *et al.* (2016) suggest higher water flows through CNTs, especially at nanotube diameters $D > 1$ nm. The absence of a universally applicable measure of quantifying flows through nanotubes results in their performance being reported using a variety of measures, such as slip lengths, friction coefficients, flow enhancements and volumetric flow rates. These cannot be directly compared with each other due to the implicit assumptions made when calculating these derived quantities. Most of these measures need the density or viscosity to be defined, which are both ambiguous quantities for confined flows.

The competing claims in the literature indicate there are two fundamental questions that need to be answered: (a) Do BNNTs offer higher water flow rates compared to CNTs? (b) what enabling factors are required for this to occur? To answer these questions, the dependence

of the flow on various membrane parameters was investigated here, including nanotube end configurations, atomic partial charges, bond lengths and nanotube diameters (D = 0.81–4.068 nm). The choice of the diameters is such that they capture both non-continuum and continuum effects at the nanometre and sub-nanometre length scales. The results obtained from the simulations carried out in this chapter are then compared to published experimental results, Mattia *et al.* (2015) for CNTs and Casanova *et al.* (2020b) for BNNTs.

The results are presented in terms of flow resistance k, which can be measured directly from both experiments and simulations. The flow resistance is defined as the ratio of pressure drop ΔP across a membrane to the mass flow rate $\dot{m}$ through the membrane. Both quantities are directly accessible for both simulations and experiments, without the need for underlying assumptions on density and viscosity. The total resistance of the membrane k_t can be further broken down into end resistance k_1 and nanotube flow resistance k_2', with total resistance $k_t = k_1 + k_2' \times L$, where L is the nanotube length. To estimate k_1 and k_2' uniquely for a nanotube of a given material, two different simulations are set up: one with the nanotube connected to reservoirs on both sides to measure end resistance (Figure 4.1(a)), and another with an infinitely long periodic nanotube, to measure nanotube flow resistance (Figure 4.1(b)). This essentially sets up two different equations, which are solved simultaneously to obtain the two unknowns k_1 and k_2'.

While no further theoretical framework is required to define the performance of nanotube membranes here, the Weissberg (Weissberg (1962)) and Hagen-Poiseuille (HP) equations will be used to estimate the values of k_1 and k_2' as an independent prediction to aid in the discussion. The expected value of k_1 is given by the Weissberg term as $k_1 \sim 8\mu C/\rho D_\mathrm{h}^3$, where ρ is the density, μ is the viscosity, D_h is the hydrodynamic diameter ($\sim D$ - σ, where σ is the LJ interaction parameter accounting for the size of the molecule) and C ($\sim$ 3.0) is the Weissberg constant. The expected value of k_2' is given by the HP equation as $k_2' \sim 128\mu/\rho\pi D_\mathrm{h}^4(1 + 8L_s/D_\mathrm{h})$, with L_s as the slip length. When L_s is assumed to be zero, k_2' values for the no-slip case is given by the HP equation. Expected values of k_2' can only be determined through previous experimentation or simulations, since it requires an estimate of the slip length. These estimated values are only used as a guide, to reflect the trends and differences with the actual observed values from the molecular dynamics simulations and experiments.

4.2 Setup

4.2.1 Nanotube creation

For creating the nanotubes, a sheet was initially created by repeating a unit cell of the corresponding 2D material, i.e., graphene sheets for CNTs, and BN sheets for BNNTs. This sheet was then rolled according to the desired chirality, creating the nanotubes. Overlapping atoms, if any, were removed in the final step to create a defect-free, pristine nanotube. The C–C bond length was kept at 0.142 nm. The B–N bond length is reported in literature to be between 0.143 and 0.146 nm (Ju *et al.* (2011); Won and Aluru (2007)). It was first verified that the change of bond lengths from 0.142 to 0.144 nm did not have any significant effect on the flow properties. All simulations were then carried out using the fixed bond length of 0.142 nm for both BNNTs and CNTs to avoid slight discrepancies in diameter between the two and, therefore, remove a possible source of confusion.

4.2.2 Setup 1

The first setup was used to determine the end resistance, and therefore featured a short nanotube connected to reservoirs on both sides, minimizing k_2 (Figure 4.1 (a)). The reservoirs had dimensions of 4 nm, 8.094 nm and 8.116 nm in the x,y and z dimensions, respectively. It was verified, using the velocity profile of water as it flowed through the nanotube under pressure, that these reservoir dimensions were sufficient to simulate bulk fluid connected to the nanotube. The bending of the flow to enter the nanotube from the reservoir was largely limited to a hemispherical region at the end of the nanotube with a diameter slightly larger than the nanotube diameter. Periodic boundary conditions were used in all three dimensions. The nanotube was aligned along the x-direction, and the other dimensions were chosen to ensure sufficient distance to simulate a bulk reservoir and avoid unphysical interactions across the periodic boundary. The nanotube length was kept at 20.045 nm, which serves two purposes: the distance between the reservoirs ensures the physics of the entrance and exit are sufficiently independent such that the flow field is distinct from that of a 2D orifice, and secondly, enough water molecules exist within the nanotube to provide a relatively steady signal of the mass flow rate. The pressure in the upstream reservoir was kept at 200 MPa, while the downstream reservoir was kept at at an absolute pressure close to atmospheric, i.e. 0.1 MPa. The number of water molecules in the reservoirs were set to reflect density data obtained from Lemmon *et al.* (2017).

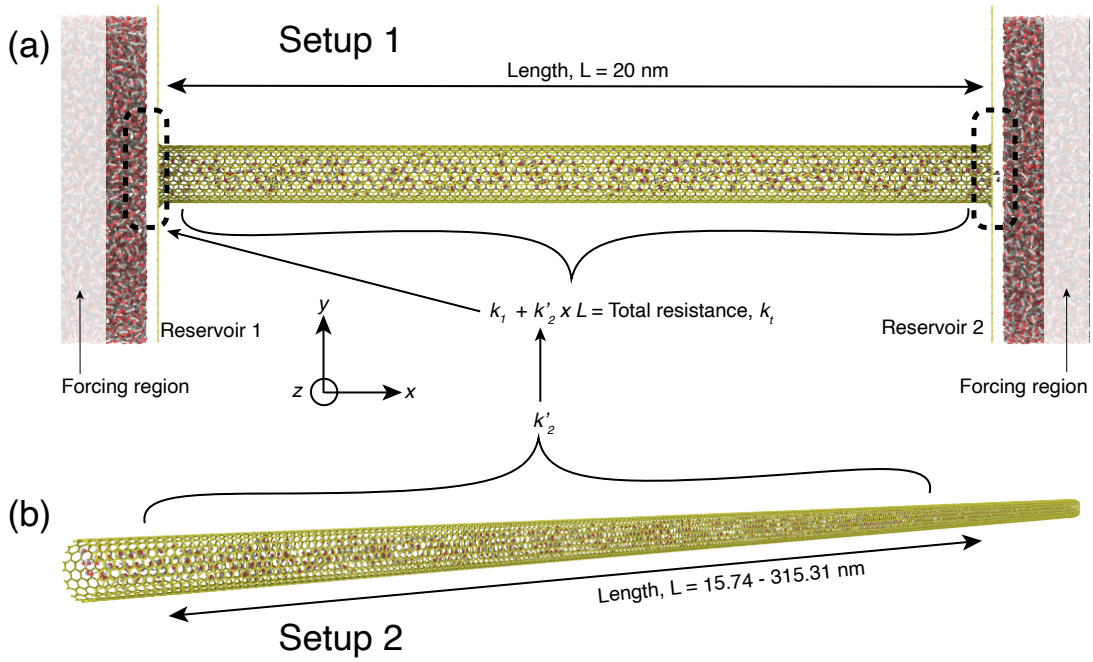

Figure 4.1: MD simulations setup for (a) end resistance (setup 1) and (b) nanotube flow resistance (setup 2). The end resistance is k_1, k'_2 is nanotube flow resistance per unit length and k_t is the total resistance. k'_2 is calculated from periodic simulation, and k_1 is calculated by subtracting $k'_2 \times L$ from k_t.

4.2.3 Setup 2

For the second setup, infinitely long nanotubes were modelled by placing periodic boundaries on the ends of a long nanotube (Figure 4.1 (b)). The lengths of the nanotubes were selected such that an adequate number of water molecules could be accommodated inside for a low noise measurement of the mass flow rate and the temperature used for the thermostat. The lengths of the CNT membranes were replicated from Borg *et al.* (2018). The lengths of the BNNTs were reduced by half as compared to CNTs due to the presence of partial charges on the nanotube atoms. The partial charges are computationally expensive to simulate as long-range interactions involving many more atoms need to be computed. The number of water molecules inside the nanotubes of setup 2 was set to equal the density measured in setup 1 as that nanotube was filled from the reservoir. This was done since the transport in the nanotubes was found to be very sensitive to slight changes in the number of water molecules.

4.2.4 Partial charges

Partial charges used for BN atoms in simulations have large variations between different studies published in the literature. Using ab-initio simulations, Won and Aluru (2008) found charges from ±0.4e to ±1.05e depending on factors such as the nanotube radius, and whether the BN atoms were in contact with water. Hilder *et al.* (2009a) commented on the lack of clarification on which values to use, and used both the values, ±0.4e and ±1.05e for their simulations. Liang *et al.* (2017) used even lower values of ±0.3e, Sam *et al.* (2018) used ±0.35e, while Ritos *et al.* (2014) used ±1.05e. The two most popular values used are ±0.3-0.4e and ±1.05e, with most studies either using one of these values or small deviations of the order of ±0.1e from these values. Contact with water is found to present the higher value of ±1.05e in the studies of both Won and Aluru (2008) and Hilder *et al.* (2010), and the lower values in the absence of water. The more recent parametrization of Wu *et al.* (2016), however, suggests a partial charge of ±0.3e even when the BN atoms are in contact with water. Partial charges used in literature are provided in Table 4.1. For this study, charges on the BN atoms were set using the charge

Table 4.1: B-N partial charges in literature

References	Partial charge (±e)
Won and Aluru (2008)	0.4–1.05
Hilder *et al.* (2009a), Ritos *et al.* (2014), Wei and Luo (2018)	1.05
Casanova *et al.* (2020b), This work	0.96
Hilder *et al.* (2010)	0.98
Hilder *et al.* (2009a)	0.4
Sam *et al.* (2018)	0.35
Wu *et al.* (2016), Liang Liang *et al.* (2017), Zhang *et al.* (2019a)	0.3

equilibration method implemented in LAMMPS (Aktulga *et al.* (2012)). The default parameters of electronegativity, self-Coulomb potential and the valence orbital exponent as presented in the ReaxFF parametrization by Han *et al.* (2005) were used for the charge equilibration on the BNNTs. This produced charges close to ±0.959e on the BN atoms, which was then fixed constant for the simulations. However, since there is uncertainty in literature about what the actual charge on BN atoms is, the charges were varied between 0 and ±0.959e to study the effect of varying the charges. The charge on carbon atoms was set to zero.

4.2.5 Lennard-Jones parameters

The Lennard Jones parameters used in literature for the interactions between oxygen atoms of water with the B and N atoms of BNNTs are presented in Table 4.2. Literature that was published pre-2016 largely used the parametrization presented in Won and Aluru (2008), while studies post-2016 have shifted to using the parametrization provided by Wu *et al.* (2016).

Table 4.2: Lennard-Jones interaction parameters in literature

References	ε_{BO} (kcal/mol)	ε_{NO} (kcal/mol)
Suk *et al.* (2008) , Won and Aluru (2008), Hilder *et al.* (2009a), Wei and Luo (2018)	0.1214	0.1500
Wu *et al.* (2016), Liang *et al.* (2017), Zhang *et al.* (2019a), Casanova *et al.* (2020b)	0.0981	0.1213
Hilder *et al.* (2010)	0.2624	0.1757

The parameters suggested by Wu *et al.* (2016) were used for this study. Water droplet simulations on BNNT sheets using this potential recreated the experimentally observed contact angles closely (see Figure 4.7). This parameter set removes the artificial hydrophilicity observed in earlier parametrizations as noted by Wu *et al.* (2016).

Table 4.3: Lennard-Jones pair-potential parameters used in this study. Pair interactions not mentioned were all set to zero.

Interaction pair	ε (kcal/mol)	σ (Å)
O-O	0.1852	3.159
C-O	0.1020	3.190
B-O	0.0981	3.322
N-O	0.1213	3.278
H-all	0	0

4.2.6 Runtime details

All simulations were first equilibrated for 0.2 ns to allow for the system to reach a steady state. Production runs were then continued for $>$3 ns until the mass flow rate was within a desired level of accuracy. The water molecules were integrated using the 'fix nve' command in LAMMPS. The reservoirs were maintained at a temperature of 300 K using Berendsen thermostats (see section 3.4.1) with a time constant of 100 timesteps. The Berendsen thermostat was chosen due to the need to have regions with and without thermostats in the simulation domain. Other thermostats (such as NVT) as implemented in LAMMPS lead to the creation of discontinuities between such regions due to the thermostat being combined with the time

integrator. For the first setup, a pressure drop of 200 MPa was created across the membrane. This was done by using the equation:

$$F = \frac{1}{\rho_n}\frac{\Delta P}{\Delta L}, \tag{4.1}$$

where F is the force on each molecule, ρ_n is the number density measured in the forcing region (see Figure 4.1a), and ΔL = 4 nm is the length of the forcing region. This resulted in a per-particle force of 0.0208 kcal/mol-Å to be added to all the oxygen atoms in the forcing region. For the second setup, a constant force was applied to all the oxygen atoms such that the flow velocity in the axial direction v_x remained in the region $10 < v_x < 100$ m/s. The applied force varied from 4.91×10^{-5} to 245.5×10^{-5} kcal/mol-Å depending on the estimated resistance of the setup. The linearity of the force-velocity relationship was also tested by halving the force and confirming that the velocity also dropped by half.

4.3 Results

4.3.1 End resistance

The end resistance k_1 for both BNNTs and CNTs are plotted against the nanotube diameter in Figure 4.2. All end resistances closely follow the Weissberg prediction. BNNTs with partial charges of $\pm$0.959e show higher k_1 compared to the other nanotubes, and this likely arises due to the irregularities in the electric field at the pore ends. This is investigated by considering two cases: one with the pore ends of the BNNT hydrogenated (BNNT-H), such that partial charges at the pore entrance are close to zero, and the original setup with no modification to the pore ends (BNNT). Both setups have the same partial charge on the B and N atoms. The molecular residence time (t_{res}) is used to identify the location where the molecules are spending their time within the system, with higher values of t_{res} indicating a bottleneck to the flow of molecules, and therefore locations with high values of t_{res} contribute more to the total resistance of the system. A spike in t_{res} is observed in the entrance and exit regions in Figure 4.3, indicating very high resistance. Low values within the nanotube indicate low nanotube flow resistance. Functionalization of the BNNT pore, as well as setting the charges at the pore end to zero reduces both t_{res} peaks, and therefore k_1.

Both the density profile (Figure 4.4) and the trajectories (Figure 4.5) of a few water molecules in front of the pore indicates that for the original setup with no functionalization of the pore ends, the molecules appear to be stuck in certain regions where the BN nanotube has a discontinuity with the BN sheet. In the density profile, this appears as a region of high particle concentration. Such phenomenon is removed when the BNNT is functionalized with hydrogen, or when partial charges around the pore entrance are reduced. These observations support the hypothesis that

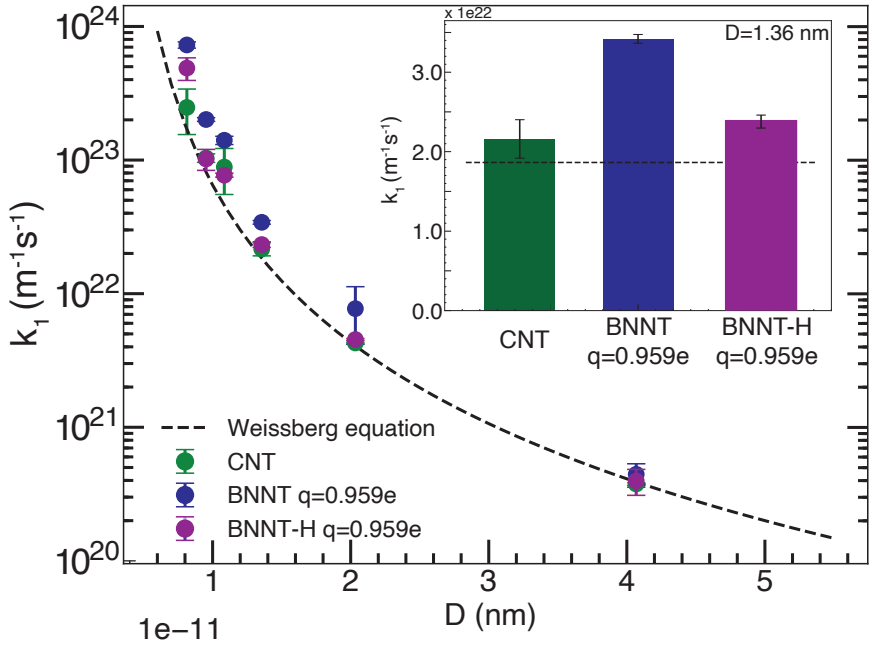

Figure 4.2: Variation of the end resistance k_1 with nanotube diameter. The end resistance mostly follows the Weissberg prediction (black dashed line) for all BNNTs and CNTs. (inset) End resistance for a (10, 10) nanotube (D = 1.36 nm). BNNT-H stands for BNNTs with the ends hydrogenated.

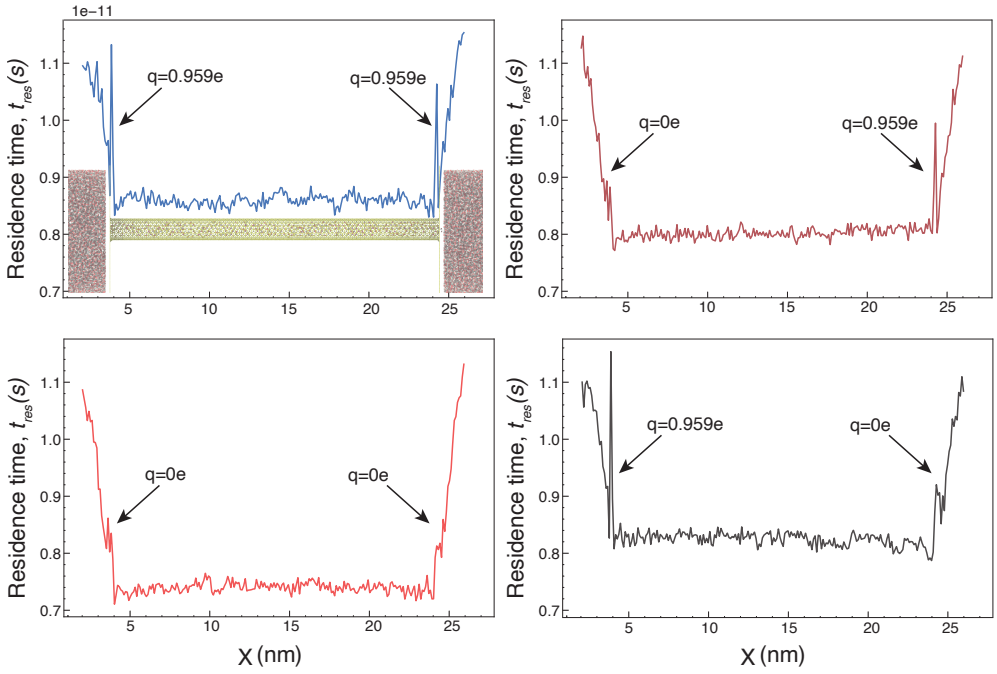

Figure 4.3: Residence time t_{res} for water molecules travelling across a (15, 15) nanotube (D = 2.03 nm), which shows distinct peaks at the ends in the presence of high partial charges. The role of partial charges at the ends is further verified by setting them to zero at only one end, which shows a consistent fall in t_{res} at the corresponding end.

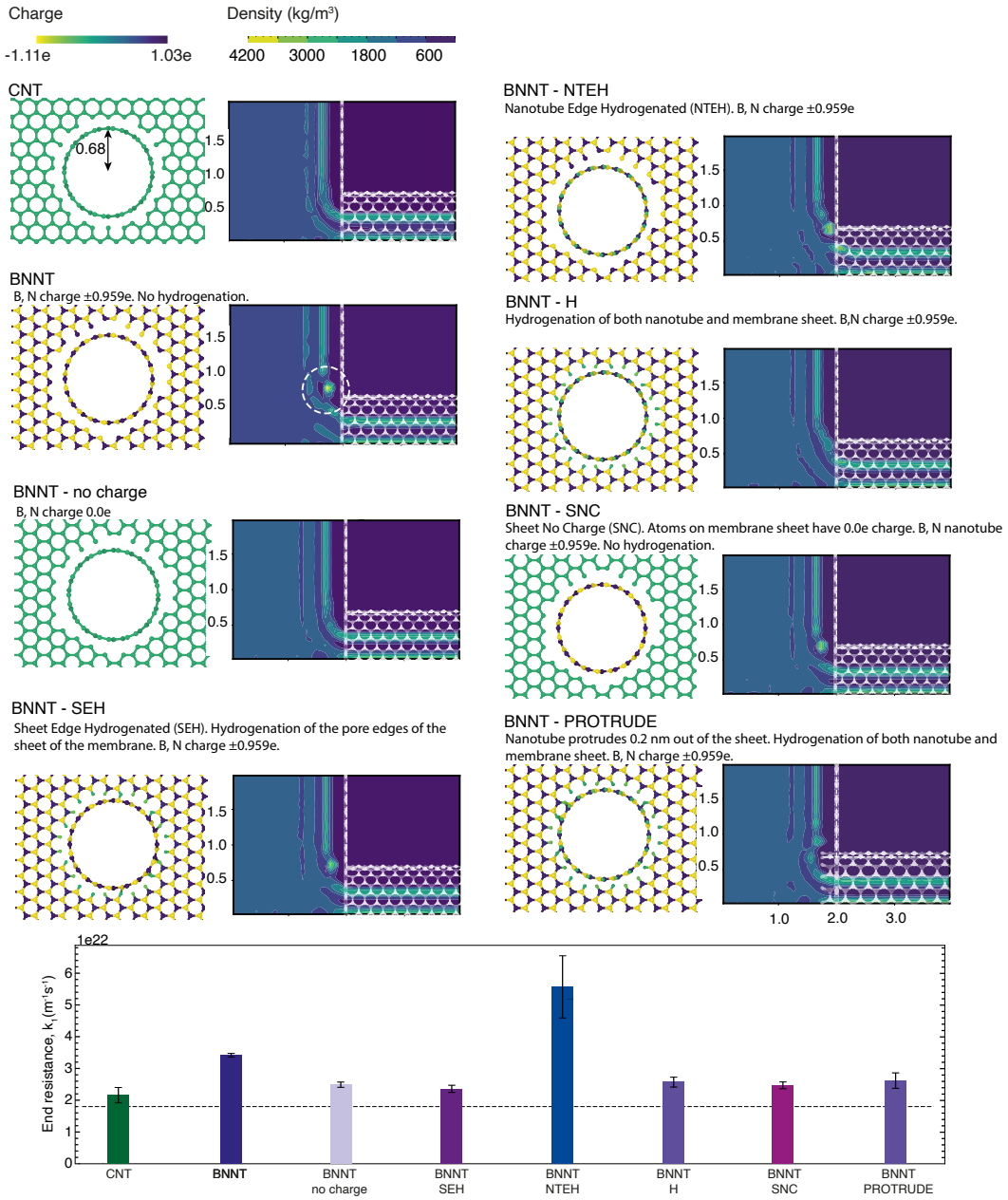

Figure 4.4: Front view of various end configurations alongside their corresponding side view of density profile for a (10,10) nanotube. End resistance of all the configurations are plotted in the bottom figure. Most configurations result in the BNNT end resistance close to the CNT end resistance. Distance units are in nm.

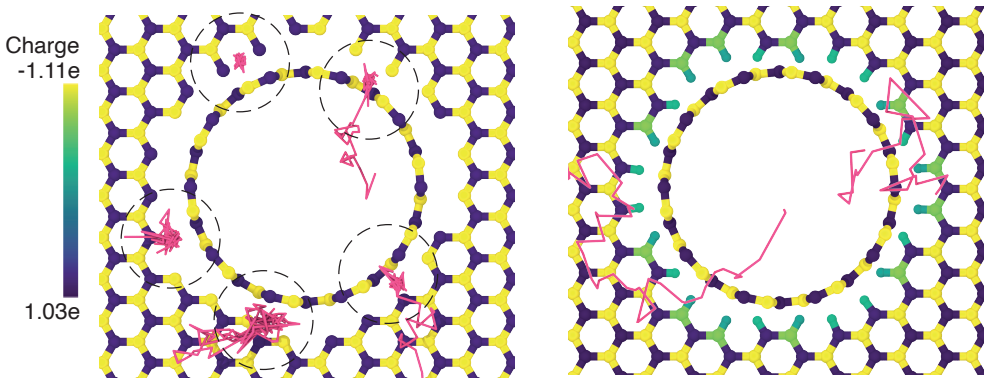

Figure 4.5: (a) Both sheet and nanotube edge atoms carry partial charges of ± 0.959e. Water molecule trajectories show that they are trapped at the edges of the sheet. (b) The pore edges are hydrogenated, with no charges on the hydrogen atoms. Trajectories show no restrictions on the movement of water molecules.

high k_1 for BNNTs may arise due to the irregularity in the electric field at the nanotube-membrane surface junction.

The pore entrance configurations in experimental membranes built using chemical vapour deposition (CVD) are more likely to be one continuous membrane surface sheet that folds itself into the nanopore to form a nanotube, with some defects likely present at the location where the sheet folds into the tube. Any defects, if present, would bind functional groups while the membrane is being created such that there are no B-N atoms at the edges with unsatisfied covalent bonds. Both these artefacts, i.e., continuous sheets and functionalization, especially with hydrogen, would lead to smooth electric fields at the pore entrance in reality. For MD studies, this must be artificially ensured. Functionalization with charged species, such as those attempted by Zhang *et al.* (2019b), however, would recreate these irregularities of the electric field. For MD studies, nanotube membranes are typically modelled by cutting a hole in a 2D sheet of the same or different material as the nanotube itself, followed by the nanotube being placed with its ends flush with the hole in the 2D sheets. This is adequate for a system that consists of only LJ interactions between water molecules and the membrane. However, when electrostatic interactions are involved, especially with a material such as boron nitride, which has a structured arrangement of positive and negative partial charges on B and N atoms respectively, the irregularity of this arrangement created at the pore entrance creates pockets of strong electric fields that traps the water molecules. For MD studies, partial charges at the pore entrance therefore must be kept close to zero, especially if simulating BNNTs with high partial charges, as this ensures the correct pore entrance physics is simulated, as shown in Figures 4.2 and 4.3. While hydrogenation of pore edges has been shown to reduce flow rates (and therefore increase resistance) in CNTs, the opposite is observed here for BNNTs with high partial charges, as the extra geometrical resistance introduced by the protruding hydrogen

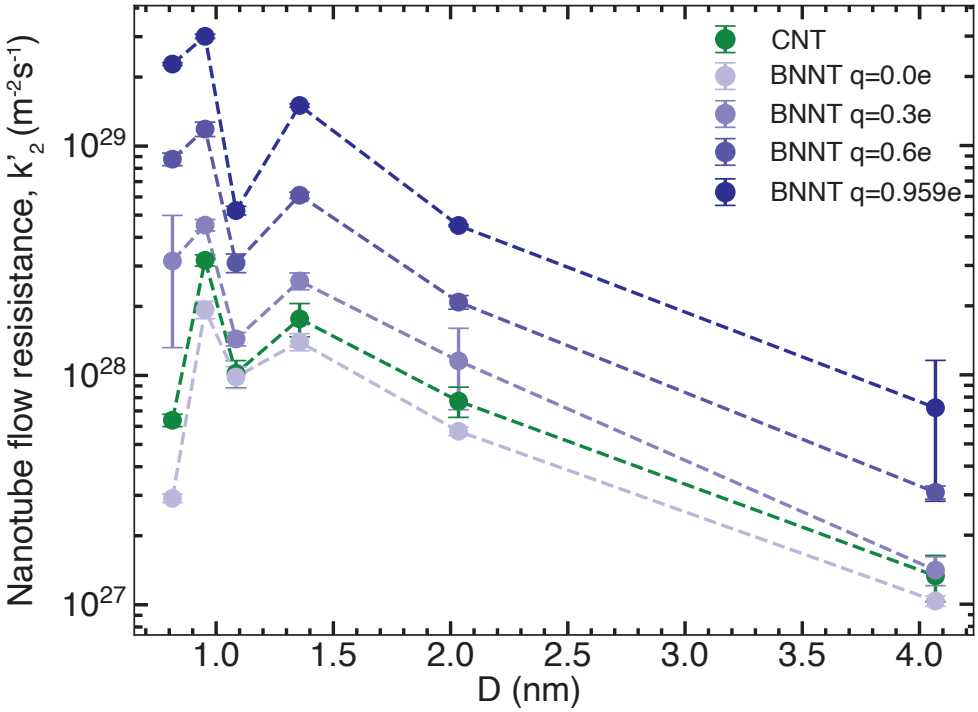

Figure 4.6: Variation of BNNT and CNT nanotube flow resistance k_2' against nanotube diameter and BNNT partial charge. Changing partial charge on the BNNT from 0.0e to $\pm$0.959e raises k_2' by one order of magnitude.

atoms is negated by the reduction in the part of the resistance which arises from electrostatic interactions.

4.3.2 Nanotube flow resistance

The role of the partial charges in determining nanotube flow resistance is estimated to be of particular importance. However, as mentioned previously in section 4.2.4, partial charges on BNNTs remains unclear in literature. The partial charges of the BN atoms on the nanotube were varied between 0.0 and $\pm$0.959e. This was only a theoretical exercise to determine the contribution of the electrostatic forces to k_2', as well as the sensitivity of k_2' to changes in the partial charges. To determine the effect of changing partial charges in the interaction parameters, droplet simulations were carried out. These droplets consisted of 17511 water molecules placed on a target surface, allowed to relax till they achieved an equilibrium contact angle. Contact angle was evaluated for all values of the partial charges used in this study were, and these did not show any appreciable change, remaining close to the experimentally observed values of the contact angle (see Figure 4.7). Interaction parameters between the solid and the liquid were therefore kept constant.

The effect of varying the partial charge of the BN atoms on the nanotube flow resistance k_2' is plotted in Figure 4.6. The k_2' for BNNTs at $\pm$0.959e is observed to be generally an order

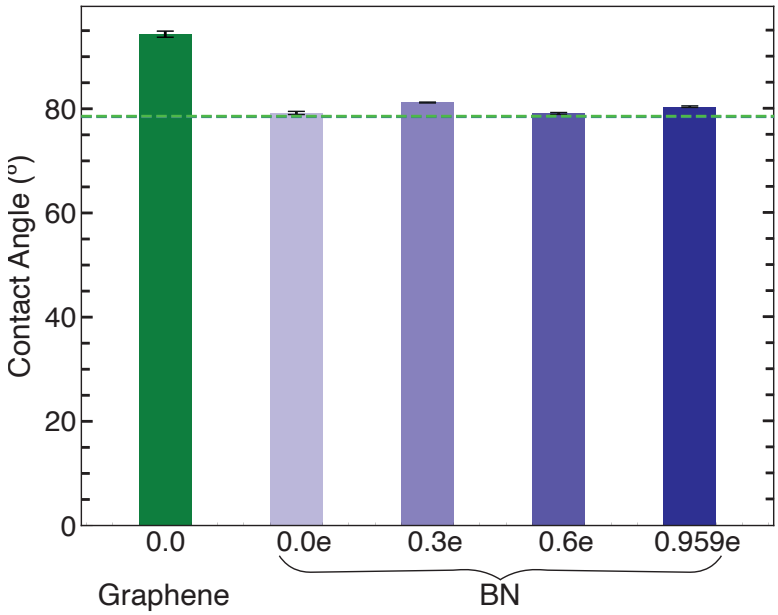

Figure 4.7: Contact angle does not change for BN surface with change in partial charge. Dashed line depicts experimentally observed contact angles for graphene and BN surfaces.

of magnitude higher than the corresponding k_2' for CNTs at all diameters. The nanotube flow resistance for BNNTs is generally seen to increase with an increase of the magnitude of the partial charge. An increase in nanotube flow resistance with increasing partial charge has been observed in literature for CNTs by Wei and Luo (2018), and for 2D hBN sheets by Govind Rajan *et al.* (2019). This is likely due to the deepening of the potential energy wells due to the electrostatic interactions as described by Wei and Luo (2018). This increases the energy required by the water molecules close to the surface to jump from one lattice point to another, increasing the local water-surface friction and overall flow resistance. The potential energy surface with and without the partial charges on the BN atoms has been plotted in Figure 4.8. As seen from Figure 4.6, at the smallest diameter, the change of partial charge from 0.0e to $\pm$0.959e results in a change of k_2' by two orders of magnitude, indicating the leading role of partial charges in determining k_2' especially for small diameter nanotubes which are likely to be used for molecular sieving and desalination applications. At zero partial charge, BNNTs do appear to show lower resistance compared to CNTs at all diameters. Implications of this finding are discussed in subsequent sections.

Figure 4.6 also shows that the trend of k_2' is disrupted by a sudden drop at a diameter of 1.08 nm for nanotubes of both materials and at all partial charges. This likely arises due to changes in the hydrogen bond network of water due to confinement effects alone as it is observed irrespective of the nanotube material. This effect has been previously observed in CNTs both experimentally and in simulations (Borg *et al.* (2018); Qin *et al.* (2011); Thomas and McGaughey (2009)).

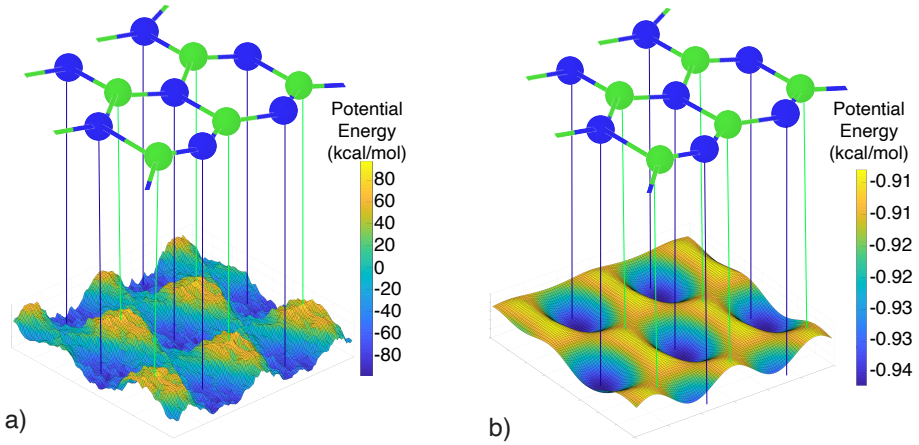

Figure 4.8: Variation in the potential energy landscape of (30,30) BNNTs with partial charge q = (a) ± 0.959e and (b) 0e. Zeroing charges makes the potential energy landscape much smoother, reducing the water-surface friction.

4.3.3 Slip length

Despite the varied and sometimes questionable assumptions needed for calculating the slip length of a nanotube from the primary variables of velocity, mass or volumetric flow rate, literature abounds with the slip lengths of various nanotubes in varying conditions calculated using different methods. Slip lengths are, therefore, a widely used measure which is directly available from literature to compare our studies against. Slip lengths taken from literature are compared with those obtained from the current set of simulations in Figure 4.9. Slip length was calculated from the simulations using the HP equation, which requires values of viscosity and density. Density was obtained by counting the number of molecules in setup 2 within a volume defined after subtracting the hydrodynamic diameter from the nanotube radius. The viscosity values used were obtained using the empirical formulation presented in Borg *et al.* (2018), with viscosity relating to the nanotube diameter as

$$\mu(D) = \mu_0 + \mu_1 exp\left(\frac{-(D_h - x^*)^2}{2\sigma_v^2}\right) \tag{4.2}$$

where μ_0 (= 0.855×10^{-3} Pa·s) is the bulk viscosity, μ_1 (= 0.945×10^{-3} Pa·s) is a fitting coefficient, x^* (= 0.781×10^{-9} m) is the location of the peak of viscosity relative to D_h and $\sigma_v = 0.1 \times 10^{-9}$ m. Partial charge of the BN atoms shows a large influence on the slip length, similar to its effect on the nanotube flow resistance. This can be traced to the inverse relationship between k_2' and L_s through the formulation provided in section 4.1. BNNTs with no charge show larger slip lengths compared to CNTs, which is comparable to the phenomenon observed for k_2'.

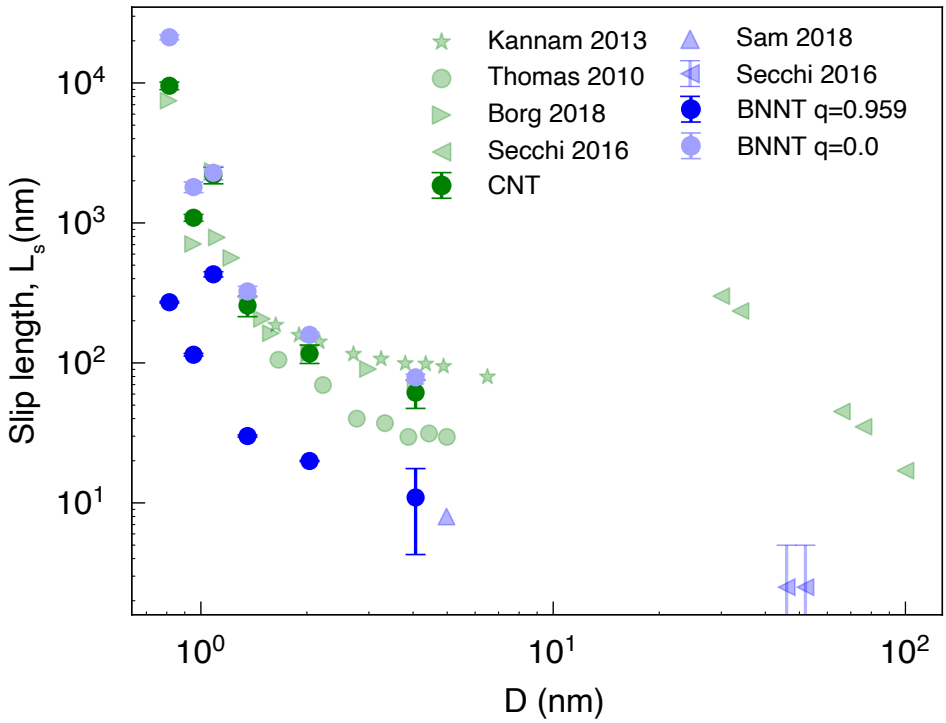

Figure 4.9: Slip length L_s for BNNTs and CNTs in this work, compared with the literature. BNNTs with high partial charge show much smaller L_s than CNTs, in line with the experimental observations of Secchi *et al.* (2016).

4.3.4 Experimental comparison

In this section, flow resistance between the present MD simulations is compared with results obtained from experiments. The experiments involve measuring the flow rate across different membranes made of aligned BNNT and CNT membranes kept in a crossflow setup, described in detail in section 5.4. The BNNT membranes used for the experiments had a thickness (nanotube length) of 50 μm, while the CNT membranes had differing lengths. The resistance of the experimental CNT membranes was therefore scaled to 50 μm by multiplying it with L/L_i, where L is the desired length of the nanotube (50 μm), and L_i is the actual length of the experimental CNT membrane. End resistances were ignored for this scaling as they are negligible for this length scale as demonstrated in the next section. Resistance for experimental BNNTs appears to be generally close to or higher than the experimental CNTs, shown in Figure 4.10. BNNT resistance also lies on and above the line predicted by the HP equation with no slip ($k_2' \sim 128\mu/\rho\pi D_h^4$, see section 4.1), indicating zero slip within the BNNT membranes. This is likely due to the presence of defects in the nanotubes, which are known to greatly reduce flow (and increase resistance) (Nicholls *et al.* (2012)).

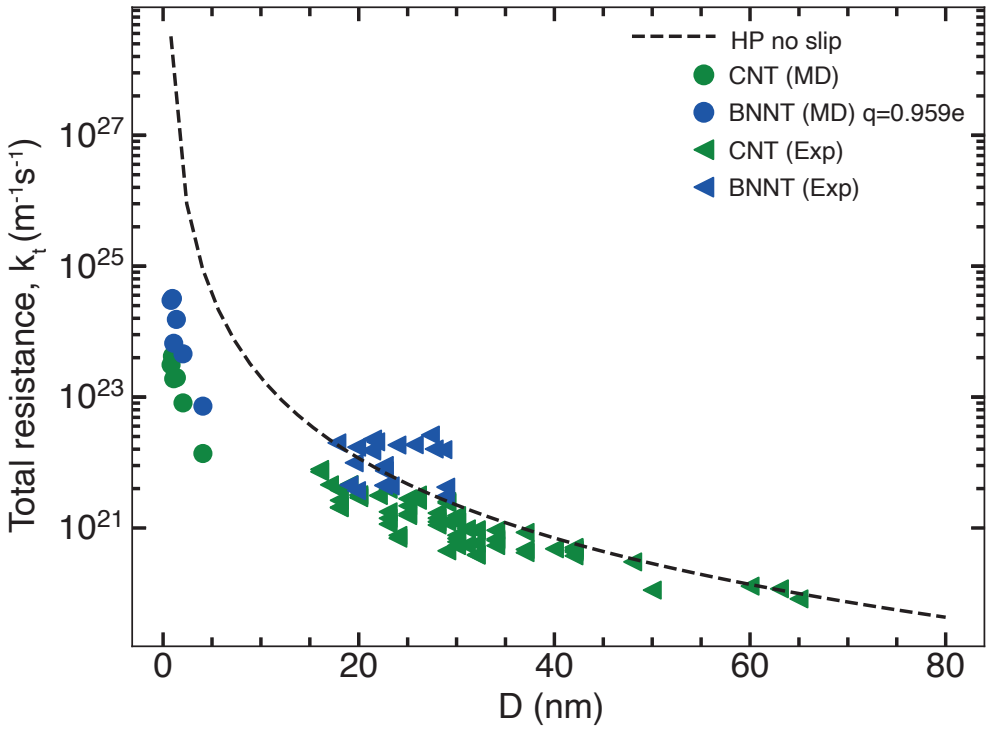

Figure 4.10: Experimental (triangles) variation of single nanotube resistance plotted against the nanotube diameter. Plotted alongside are the results from MD simulations (circles) of small diameter nanotubes, and the HP no-slip solution (black line). All membranes considered have been scaled to 50 μm. Entrance/exit resistances are negligible, and not considered in the theoretical prediction line.

Plotting the simulation results in the same graph shows a similar distribution of resistances,

with BNNTs ($q = \pm 0.959$e) providing slightly higher resistance than CNTs. Both BNNTs and CNTs show much lower resistance than that predicted by the no-slip HP equation, in contrast to experimental results, which lie close to the HP equation's predictions. This is likely due to two factors: the smoothening of the nanotubes potential energy surface due to increased curvature at lower diameters, as outlined by Falk *et al.* (2010), and the use of defect-free, pristine nanotubes for simulations.

4.3.5 Explaining disagreements in literature

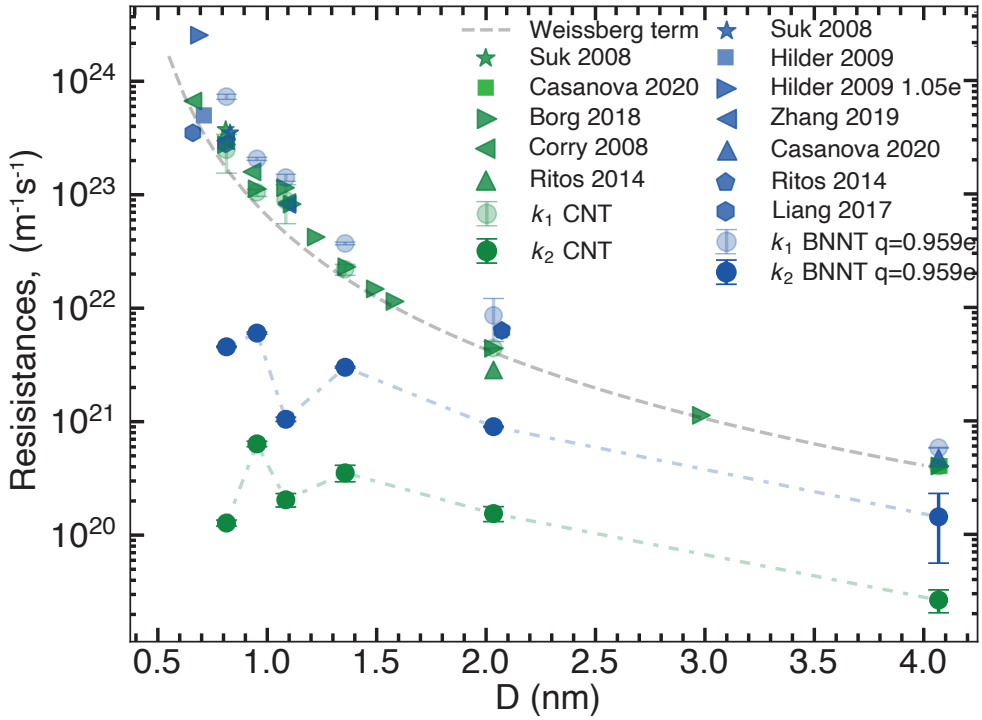

Figure 4.11: Comparison of total resistance (k_t) from literature, alongside end (k_1) and nanotube flow resistance (k_2) from the current simulations. k_t from literature is comparable to the k_1 from our simulations and to the Weissberg prediction. Most of the studies in literature have nanotube lengths shorter than 20 nm. k_2 from the current simulations are plotted for a nanotube length of 20 nm, using the equation $k_2 = k_2' \times L$. k_2 is shown to be an order of magnitude lower than k_1 at these nanotube lengths for both BNNTs and CNTs, despite k_2 for BNNTs being significantly higher than CNTs. This is evidence that measurements of k_1 cannot be used to define the nanotube flow resistance, k_2.

Having determined the magnitudes, as well as the various factors affecting both the major components of resistance in BNNT and CNT membranes, the discrepancies observed in literature in the relative performance of BNNTs and CNTs can now be explained. The end resistance k_1 obtained from the short membrane simulations described in section 4.2.2 have been plotted alongside the resistances obtained from literature in Figure 4.11. Both values of resistances from literature and MD simulations lie close to each other, and interestingly, all lie

on the line predicted by the Weissberg equation ($k_1 \sim 8\mu C/\rho D_h^3$, see section 4.1). Most MD simulations in literature tend to use nanotubes that are shorter than 20 nm in length to save computational cost, this influences the way results of simulations of different materials need to be interpreted. To elaborate, Figure 4.11 shows k_2 results for nanotubes of length 20 nm without any end resistance. For this nanotube length, representative of most literature studies, it can be seen that k_2 for BNNTs is an order of magnitude larger than for CNTs. However, both sets of k_2's for BNNTs and CNTs are an order of magnitude lower than the end resistances k_1. This tells us that, for transport measurements in membranes chosen in the literature, the total resistance k_t which determines the rate of transport is dominated by the end resistances k_1, while the nanotube flow resistance (i.e. k_2) is negligible. MD simulations of flows through nanotube membranes are essentially capturing two different kinds of flow physics: a) that of the nanotube ends, where resistance arises due to the need of the fluid to bend and enter the pore, and b) inside the nanotube, where resistance arises due to interactions of the fluid with the nanotube walls. Since the total resistance (k_t) in these thin MD membranes (with $L \leq 20$ nm) are dominated by the end resistance (k_1), which in turn can be dependent on pore-specific factors (e.g. partial charges, pore configuration, defects at the pore end etc.), comparisons of performance between different material nanotubes cannot be reliably achieved using this setup. For nanotubes which have low solid-liquid friction (and therefore low k_2) but high end resistance k_1, such an MD setup would indicate poor flow rates compared to another nanotube with high solid-liquid friction but low k_1, providing an inaccurate result, as laboratory-sale nanotubes would show the opposite to be true (as discussed below). Furthermore, the reason why it it is important to untangle the transport inside the nanotube from the end losses is because in experimental membranes, end losses no longer dominate, and it is the measurement of k_2 that is required to directly extrapolate to experiments, not k_1, which is the dominant influence over all measurables in the thin membrane MD simulations. The end resistance largely depends on the pore end configuration: the functional groups attached to the end, the shape of the pore end, the charges on the membrane surface surrounding the edge and as such, and these factors would likely have little influence on the resistance inside the nanotube. This is in contrast to the fluid-solid interaction inside the nanotube, which would have little influence on the end resistance. The components of resistance for flows through nanotubes must therefore be analysed separately, instead of considering a single metric such as the flow rate or slip length to characterise the resistance of the entire membrane. This is especially true for charged membranes such as BNNTs, where charges influence both k_1 and k_2 in different ways.

4.3.6 Answering the main questions

The two fundamental questions raised in the introductory section of this chapter, about whether BNNTs can offer higher flow rates compared to CNTs and under what conditions can this happen is now answered. BNNT-H has similar k_1 to CNTs as shown in Figure 4.2. Despite the slight differences at smaller diameters, k_1 for both CNTs and BNNT-H largely follows the prediction of the Weissberg equation. k_2 on the other hand depends on the partial charge of the BN atoms, and at zero partial charge, k_2 for BNNTs is lower than CNTs. The partial charge of BN atoms is the dominant factor that determines k_2 for BNNTs. The absence of any partial charge appears to show that BNNTs might provide lower k_2 than CNTs at any diameter. This, however, is unrealistic as the nature of the covalent bond between B and N atoms imparts a partial charge to the BN atoms. Experimental evidence from the work described in chapter 5 also shows that total resistance for BNNTs is higher than CNTs. This further lends credence to the partial charges on the BNNTs being on the higher side of the reported ranges between ± 0.3—± 1.05e.

The end resistance k_1 and nanotube resistance k_2 can then be added to determine the total resistance of laboratory-scale membranes of any thickness L. Figure 4.12 shows the total resistance of membranes plotted against the membrane length. At micrometre lengths, which is the most common for nanotube membranes fabricated in laboratory settings, k_2 is clearly shown as the dominating contributor to the total resistance k_t, with k_1 playing a negligible role.

For predicting flows through long, laboratory-scale membranes from MD simulations, greater weightage should therefore be given to nanotube flow resistance. This can be predicted through modelling infinitely long nanotubes using periodic boundary conditions on sufficiently long nanotubes. The density of water inside such nanotubes should ideally be obtained from short membrane simulations where reservoirs of water are used to fill the nanotube. Short membrane simulations are therefore useful for only priming the long nanotube simulations, but not for directly measuring mass transport and predicting the total membrane resistance as they are highly susceptible to changes in the end resistance. The lengths at which both k_1 and k_2 play a considerable role largely depends on the ratio of k_1 to k_2'. The slip length L_s might be used as a proxy for this measure, and therefore, nanotube materials with lower slip lengths (and higher k_2') would have k_2 start dominating at much smaller nanotube lengths against those with higher L_s. For CNTs, this transition from a k_1 dominated total resistance to a k_2 dominated one happens at around 500 nm. This is comparable to the 300 nm length reported by Walther *et al.* (2013) beyond which entrance/exit effects stop having an effect on flow rates for CNTs. For BNNTs, this transition happens much faster, at around 100 nm due to higher k_2' (and lower L_s). Full membrane MD studies would therefore be needed for CNTs less than 500 nm long, and BNNTs less than 100 nm long. In contrast, commercially available RO membranes are a few hundred nm thick, and lab-grown CNT and BNNT membranes have nanotubes usually a few

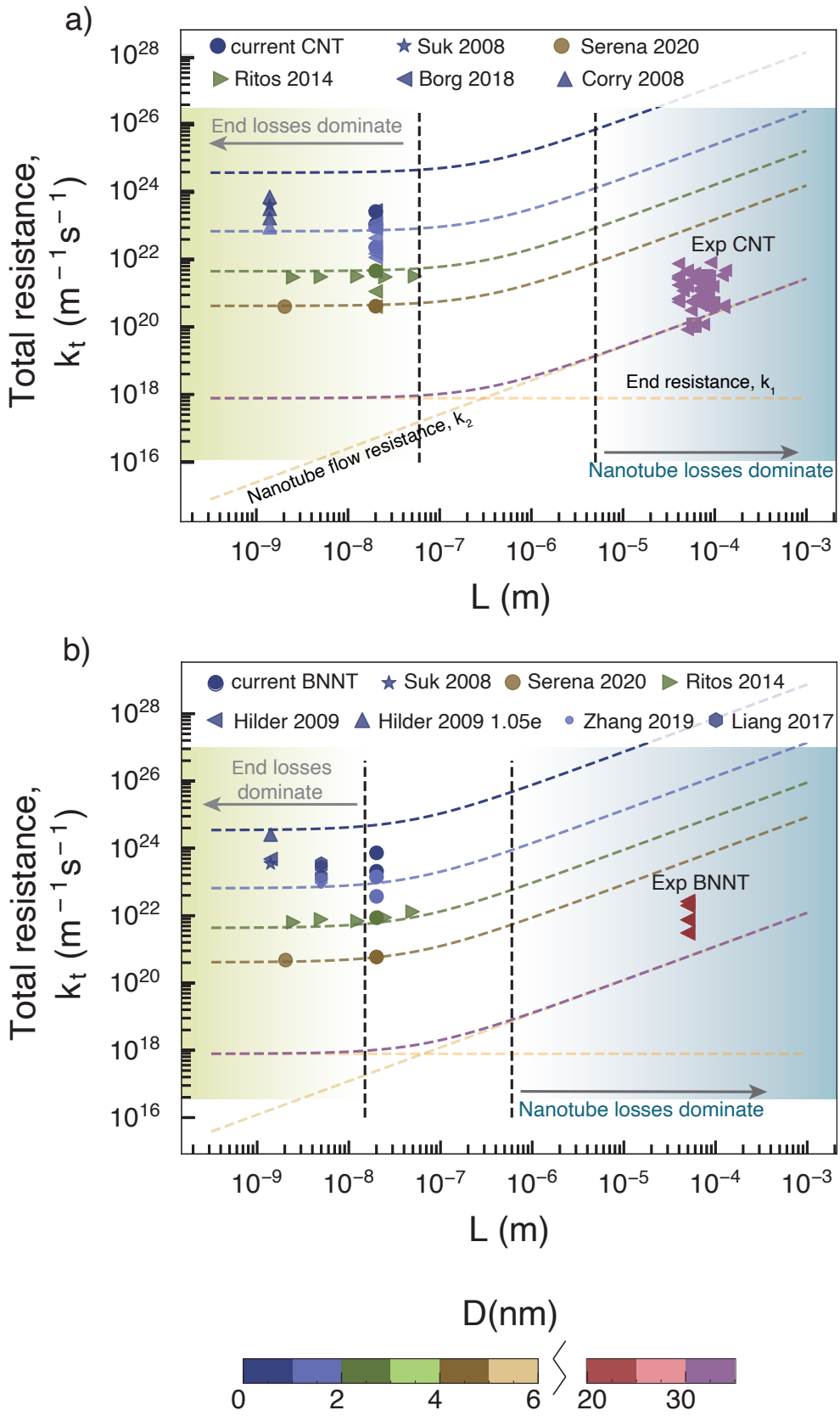

Figure 4.12: Variation of the total resistance with nanotube length L for (a) CNTs and (b) BNNTs. Most MD simulations use nanotubes with lengths of tens of nanometres, which lie in the region where k_1 dominates. Experimental studies use nanotubes of a few μm in length, where k_2 dominates and k_1 is insignificant in comparison. Theoretical predictions of the resistance are computed using slip lengths of 60 nm for CNTs and 10 nm for BNNTs.

micrometres long due to their fragility and handling issues.

4.4 Conclusion

Current literature on water flows through BNNTs presented confusing results, with some showing flow rates higher than CNTs while others showed lower flow rates compared to CNTs. This chapter demonstrates that these disagreements might have arisen due to the short nanotubes (< 20 nm) considered in MD studies, where the total resistance (and hence the flow rate in a typical comparison study using a membrane setup) would be dominated by the resistance k_1 at the nanotube ends alone. This has a masking effect of pinning down the actual nanotube flow resistance k_2, which starts to dominate over k_1 for laboratory-scale membranes. A (6,6) BNNT at 20 nm long has a k_2 of 4.57×10^{21} $m^{-1}s^{-1}$, but this is insignificant against the end resistance k_1 of 7.27×10^{23} $m^{-1}s^{-1}$, a two order of magnitude difference. Conversely, a (6,6) BNNT of length 50 μm has a k_2 of 3×10^{24} $m^{-1}s^{-1}$, which now dominates over k_1. In the presence of partial charges, end resistance is largely governed by the electric field close to the pore end — sharp discontinuities and strong electric fields are found to increase the end resistance drastically. The same also holds for the nanotube flow resistance, with the presence of charges increasing the resistance by an order of magnitude. Estimating the total resistance of nanotube membranes of any thickness, therefore, requires separate studies of both kinds of resistances, with k_2 depending on the nanotube length, before adding them up to get the total membrane resistance. In this chapter, estimates of resistance from the MD studies using this two-setup method show that BNNTs are likely to underperform CNTs for the flow of pure water, and this has also been backed up by experimental studies.

Chapter 5

Enhanced nanoparticle rejection in aligned boron nitride nanotube membranes

Parts of this chapter have been published in: Casanova, S., Mistry, S., Mazinani, S., Borg, M. K., Chew, Y. M., and Mattia, D. "Enhanced nanoparticle rejection in aligned boron nitride nanotube membranes". *Nanoscale*, 12(41):21138–21145, 2020b. Experimental work has been carried out by Serena Casanova and Davide Mattia at the University of Bath. CFD simulations have been carried out by Saeed Mazinani at the University of Bath.

Chapter 4 showed how BNNTs provided higher resistance to water flow compared to CNTs due to their charged structure. This chapter focusses on the advantages of having such a charged structure in BNNTs, in the form of high selectivity and rejection. The chapter explores electrostatic repulsion as an additional mechanism of selective filtration for charged particles, alongside size-based filtration. BNNT membranes naturally acquire a surface charge when in contact with water and therefore serve as an ideal candidate to exploit charge-based particle rejection.

5.1 Introduction

Nanotube filtration membranes largely remove foulants through the use of steric hindrance, i.e., having pore entrance geometries wide enough such that the foulants cannot enter the pore, while the desired fluid and other molecules can. The geometric constraints are often achieved by reducing the pore diameter below that of the foulant sizes. This causes several challenges – extremely small pore diameters of around a few nanometres are required for removing salts from solutions, severely restricting the amount of pure water that can flow through the membrane pores, and increasing the amount of energy required to push water through. If higher purity is desired in the filtrate, the membranes pores need to be further reduced in size, lowering the flow rate by the cube of the pore diameter. Furthermore, using geometric filtration alone

restricts species selectivity, as two particles of different types but identical size would both be restricted from entering the pore.

An alternative to geometry-based rejection is charge-based rejection. This is achieved when the filtration membrane acquires a charge, either due to its surface chemical properties, due to deposition of ions from the solution onto the surface, or due to induced charges on the surface from ions in solution next to the surface. This causes an electric potential to develop in front of the membrane, which is modulated by the counterions present in the solution, giving rise to an electric double layer and a potential which drops exponentially from the membrane surface. This electric potential then repels ions with like-charge as the membrane. Charge-based rejection overcomes many of the limitations of the traditional rejection mechanism – it works alongside geometry-based rejection and therefore, allows for the design of pores much larger than the foulant itself. This allows high flow rates of the desired fluid and reduces the pressure drop needed across the membrane. It also helps increase membrane selectivity as both foulant size and charge can be targetted.

CNTs can be modified with charged functional groups added to their pore entrances to effect charge-based rejection, but the addition of functional groups to CNTs have been shown to have a large reduction in the flow rate (Corry (2011); Majumder and Corry (2011)). BNNTs naturally have a high negative zeta potential (the electric potential measured near the surface of a charged membrane, defined in Chapter 3) when in contact with water (Lei *et al.* (2015)). BNNT membranes may therefore be better suited to the removal of charged species from a solution. In this chapter, rejection and permeance of charged species between BNNTs and CNTs have been investigated as a comparative study. MD simulations were used to identify and characterise the mechanisms which govern the rejection process, and experiments were used to help verify the findings of increased rejection of like-charged particles from BNNT membranes.

5.2 Simulation

In this section, the setup of the MD simulation is discussed, followed by the results on rejection and flow rates and the underlying mechanisms of the processes involved.

5.2.1 Simulation setup

The simulation setup consisted of a charged spherical particle in front of a single BNNT and CNT pore, as depicted in Figure 5.1. The pore diameter D_P was fixed and the diameter of the nanoparticle (D_{NP}) was varied, which also varied the pore-particle diameter ratio (D_{NP}/D_P). The pressure difference across the membrane was also varied. The behaviour of a charged membrane and particle in response to variations of both the enabling forces of flow into the membrane and the repulsive van der Waals and electrostatic forces was studied.

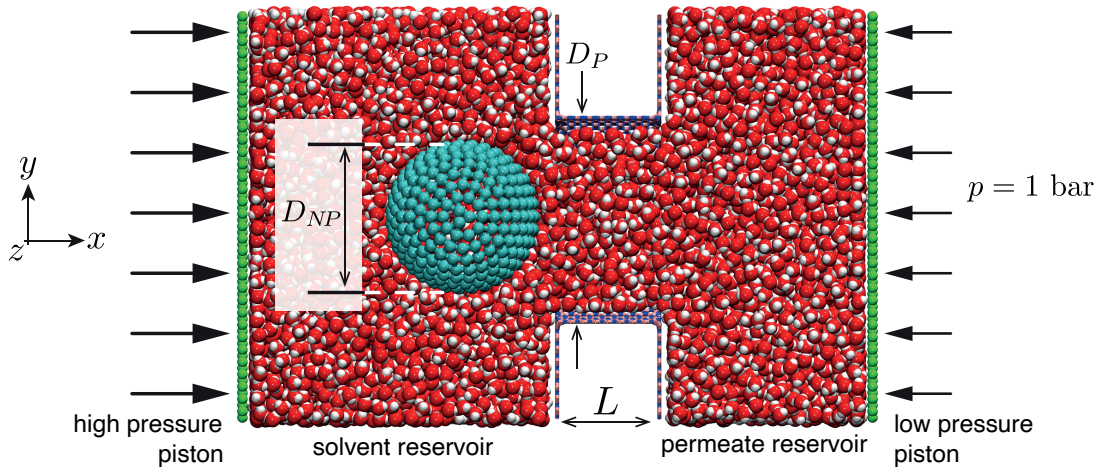

Figure 5.1: MD snapshot of case setup for BNNT membrane with particle placed in the solvent reservoir, with D_{NP}/D_P = 0.9.

MD can practically model systems the size of only a few nanometres across, as larger systems would require unfeasible computational costs. Experimentally, it is difficult to create nanotube membranes thinner than a few tens of nanometres. Despite these constraints, the experimental and simulation setups were made as close to each other as possible. For the simulations, this was achieved by replicating the experimental pore-particle diameter ratio, and using a nanotube large enough to replicate bulk fluid flow within it, as would be the case in experiments. Pressure-controlled reservoirs were placed on both sides of a single membrane pore. The charged particle was placed in the upstream reservoir. A (30,30) BNNT/CNT was used to model the pore, therefore keeping the pore diameter fixed at 4.068 nm. This pore diameter is small enough to be feasibly simulated using MD but large enough to have a bulk-like flow in the central region of the nanotube to simulate the flow in the much wider experimental nanotubes. The hydrodynamic diameter, which is the diameter after subtracting the inaccessible space due to repulsive van der Waals interactions, is therefore 3.254 nm. Since the physics of axial flow inside the nanotube was not the target area of this study, the nanotube length was kept as 2.04 nm, slightly more than the LJ cutoff distance to prevent the influence of one reservoir on the other. The membrane was constructed by placing the nanotube flush with sheets of the same material (BN or graphene) as the nanotube, on both ends of the nanotube. A hole is cut in the centre of the sheet according to the nanotube dimensions. Pore-particle diameter ratios of 0.6, 0.7, 0.8, 0.9 and 1.0 were studied. The particle diameters studied were 1.627 nm, 2.034 nm, 2.441 nm, 2.848 nm and 3.254 nm, respectively. The particle was constructed as a hollow spherical shell made of atoms which were fixed rigid. The number of atoms on the shell was kept consistent with an area number density of around 60 nm^{-2}. The upstream reservoir had the dimensions 6.0 nm $\times$ 8.11 nm $\times$ 8.09 nm in the x,y and z directions respectively, with x being the flow direction. The downstream reservoir was 4.0 nm in the x-direction and shared the y and z dimensions with the upstream reservoir. The upstream reservoir was kept slightly

larger in the x-direction to accommodate both the particle and a larger volume of water to simulate water flow for a desired amount of time without the need for replenishment. The y and z dimensions were chosen to be around twice the size of the pore, to allow for better capture of the flow dynamics, and provide a larger space for the unimpeded Brownian motion of the particle. The pressure was maintained on both reservoirs through the use of pistons. This was achieved by adding a uniform force to each molecule of the piston. The value of the force to be added was arrived at by multiplying the pressure desired with the area of the piston, divided by the number of atoms in the piston, which numbered 2508 for each piston. The downstream reservoir was maintained at atmospheric pressure, 0.1 MPa. Pressure on the upstream reservoir was kept at 0.5 MPa, 2.0 MPa, 6.0 MPa, 10.0 MPa and 100.0 MPa, respectively. The number of water molecules in both reservoirs and nanotube was set to an initial density of 1000 kg/m^3.

The charges on the carbon atoms of the CNT membranes were all kept zero, as the experiments have shown near-zero surface charge. For the BNNT membranes, charge equilibration using the ReaxFF parameterization was used to arrive at a partial charge of around $\pm$0.9e for the B and N atoms. A charge of 0.005e was then subtracted from the boron atoms to get a net surface charge density of -1.28 $\times 10^{-20}$ C/nm^2, which is the charge density for BNNT membranes obtained from experiments. A charge of -0.003e was applied to the atoms on the particle to provide a surface charge density of -6.99 $\times 10^{-21}$ C/nm^2, which was also obtained from experiments.

Runtime details

All flow cases were simulated in an NVT ensemble using the velocity-Verlet algorithm with a timestep of 2 fs. The temperature in both reservoirs was maintained at 300 K using a streamwise-velocity unbiased thermostat (Shinoda *et al.* (2004)). The system was allowed to equilibrate for around 0.5 ns for the pistons to apply steady pressure on the reservoirs, during which time the particle was kept fixed in its position. Once equilibrated, the particle was unfixed from its position, and the simulation was run for around 8 ns, with position and velocity sampling at every 1000 timesteps, or every 0.002 ns. A second set of MD simulations were conducted to investigate the equilibrium surface, constructed by joining the points of equilibrium, which are points in the space in front of the membrane where the water-particle and wall-particle forces cancel out each other. The further away the points of equilibrium are from the membrane surface, the higher is the probability of particle rejection. The location of the equilibrium surface was investigated by moving the particle in very small increments around the pore entrance and then freezing the particle at a location while applying a pressure drop of 2 MPa. The flow was allowed to reach a steady-state before force measurements were carried out. When a steady state was achieved, the force balance between the water-particle force pushing the particle into the pore, and the wall-particle force repulsing the particle away from the membrane, was calculated.

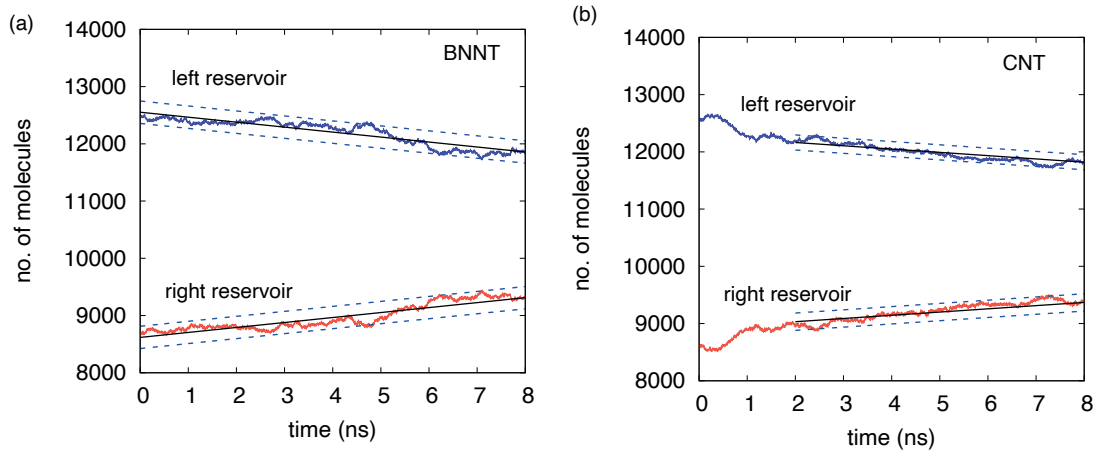

Figure 5.2: Number of molecules in the left and right reservoir as a function of time used to calculate the mass flow rate. (a) BNNT and (b) CNT. Pressure drop applied across the membrane is 2 MPa.

5.2.2 Results

Flow rates

The flow rates were calculated by measuring the number of water molecules in both the upstream and downstream reservoirs with respect to the runtime and then calculating the resulting slope of the linear fit, outlined in Figure 5.2. The flow rate was averaged from both reservoirs. The flow rate was calculated at a number of different pressures and the line of best fit between the pressure drop and the mass flow rate was plotted. As can be seen in Figure 5.3, the flow rate for CNT membranes is slightly higher than BNNT membranes when there is no particle impeding the flow, and this can be attributed to the reasons described in Chapter 4.

For the case with the particle present in the reservoir, a pronounced drop in flow rate is observed, but the comparative behaviour of the flow rates between BNNTs and CNTs depends on the pressure and the ratio D_{NP}/D_P. For the case where D_{NP}/D_P is equal to unity, the flow rates for the BNNT are always greater than for the CNT. For the case with D_{NP}/D_P equal to 0.9, at low pressures, BNNTs show slightly higher flow than CNTs, but this is reversed at higher pressures. While a large number of pressure drops were studied for $D_{NP}/D_P = 0.9$ to obtain general trends, studies at other D_{NP}/D_P ratios were limited to a few pressure drops to save on computational time.

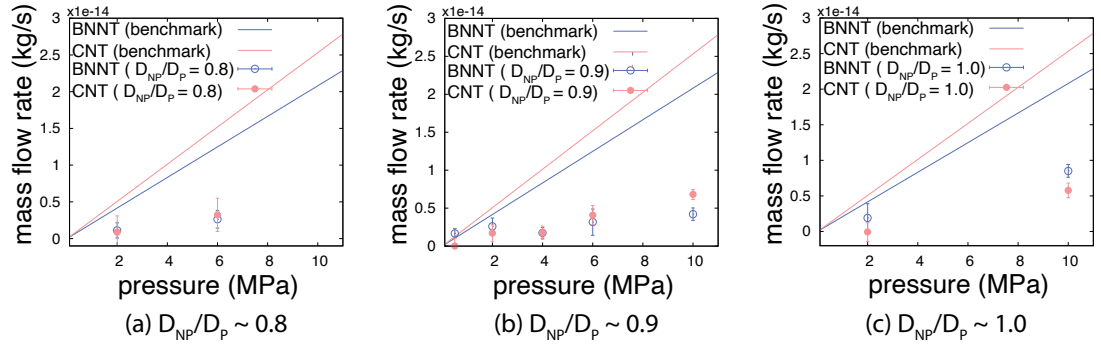

Figure 5.3: Mass flow rates against pressure drop for BNNT and CNT cases, and three D_{NP}/D_P ratios (a) 0.8, (b) 0.9 and (c) 1.0. Benchmark cases represent cases with no particles.

Pore-particle distance

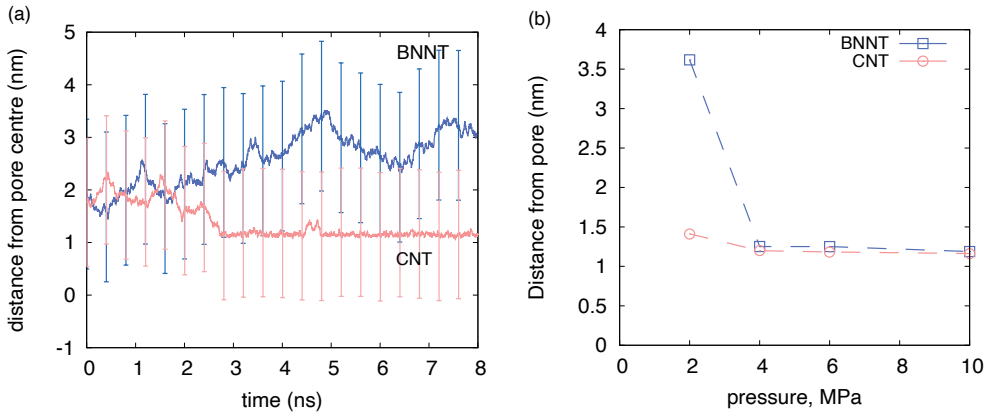

Figure 5.4: (a) Magnitude distance of particle from pore centre for D_{NP}/D_P = 0.9 at 2 MPa. The vertical lines indicate particle diameter. (b) Average pore-particle distance at different pressures for D_{NP}/D_P = 0.9.

To explain the comparative reversal of flow rates at D_{NP}/D_P = 0.9, the mean position of the particle in front of the membrane is plotted against the pressure drop. While the particle stays further away from the BNNT membrane than from the CNT membrane, this distance is greatly reduced at high pressures. At low pressures, the force from the fluid on the particle is weak, and this is therefore balanced by the electrostatic repulsion force at a distance much further away from the membrane surface. As the hydrostatic pressure increases, so does the water-particle force pushing the particle towards the pore. The repulsive wall-particle electrostatic force rises with decreasing pore-particle distance. Therefore, to counter the high water-particle force, the equilibrium surface at increased pressures shifts closer to the pore. This results in a pore that is more clogged, reducing the flow rate. At high pressures, the electrostatic interactions in the BNNT can keep the particle just slightly further apart from the membrane than the CNT, but the flow rate through the BNNT drops, (see Figure 5.3). The larger drop in flow rates in BNNTs

compared to CNTs when the particle is at an identical location relative to the pore may be attributed to two factors: the high end resistance of BNNTs due to the nature of the pore model, as explained in Chapter 4, and the mobility of the particle in front of the pore.

MSD

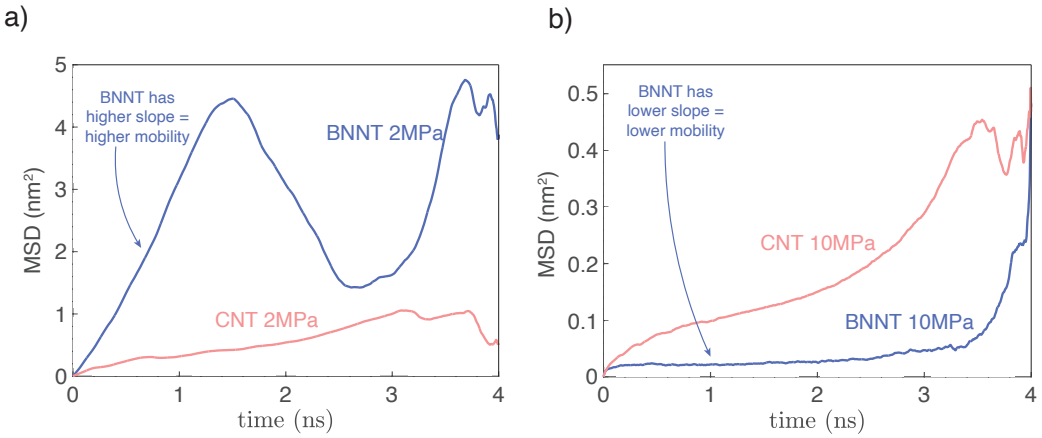

Figure 5.5: Mean squared displacement (MSD) plots for D_{NP}/D_P = 0.9 for (a) 2 MPa and (b) 10 MPa pressure drop.

To investigate the mobility of the particle in front of the pore, the mean squared displacement (MSD) of the particles is plotted for two different pressures (see Figure 5.5). The MSD was calculated by tracking the particle position every 0.002 ns, and the displacement for a given time delay was averaged for the entire duration of the production run. The MSD, therefore, tends to get noisier as the time increases, as the number of samples to average over reduces. At low pressures, the particle is much more mobile in front of the BNNT membrane, seen from the higher slope of the MSD. This is reversed for higher pressures, and the particle appears to drift very little in front of the BNNT, compared to the CNT membrane. This might lead to increased clogging at the entrance of the BNNT, even though the particle is marginally more distant from the pore.

Forces

The net force on the particle (see Figure 5.6) due to its interaction with water and the membrane was calculated separately. This was done by keeping only the target interaction (either particle-membrane or particle-water) on and turning off all other interactions. To estimate the contours of the net force felt by the particle in front of the pore entrance (see Figures 5.7 and 5.8), the particle was artificially moved through an imaginary "grid" of points in front of the pore, stopping at each grid point for 1 ps to average the force felt by the particle at that location. The grid points were separated from each other by 0.2 nm at the farthest from the membrane and by 0.05 nm close to the membrane surface and inside the nanotube. A pressure drop of 2 MPa was maintained during the force collection. Adequate amount of water was maintained in the

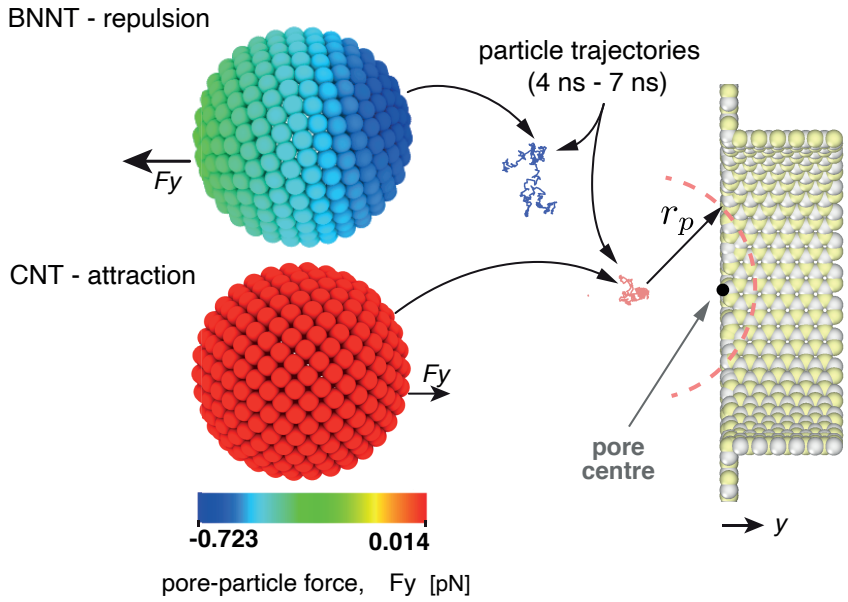

Figure 5.6: A net repulsive pore-particle force acts on the particle introduced in the BNNT system, whilst weaker van der Waals forces attract the particle to the neutrally charged CNT. As a result, silica particles enter the CNT but are repelled from the BNNT, as shown by their particle trajectories plotted for the time interval 4 ns–7 ns.

reservoir while the particle was moved between grid points by interrogating only a few grid points per simulation.

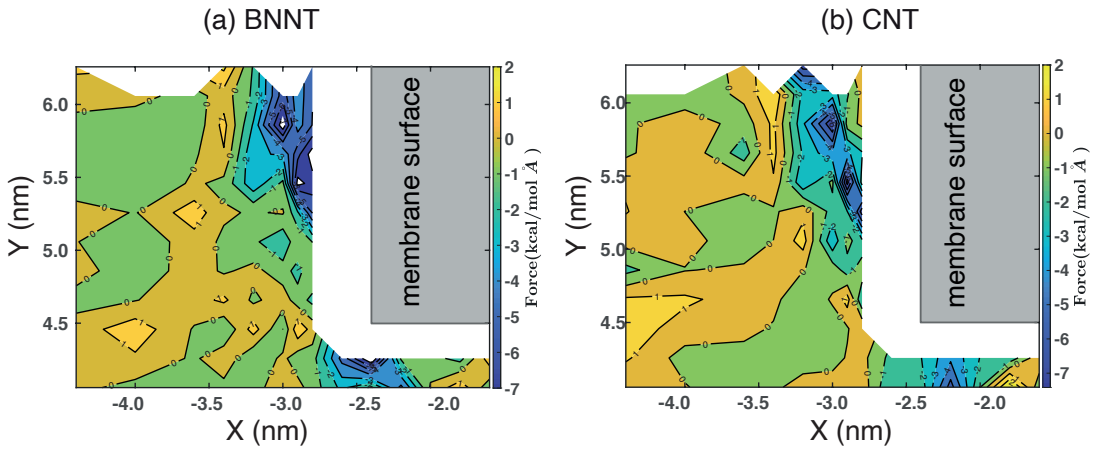

Figure 5.7: Contour plots for D_{NP}/D_P = 0.9, Δp = 2 MPa: (a) BNNT and (b) CNT; The membrane surface has been displaced by the particle radius (14.2 nm) in these figures for better clarity.

To better illustrate the difference in the force contours between BNNTs and CNTs, the contour lines of zero net force are joined and plotted in Figure 5.8. The isoline of zero net force lies further away from the surface for the BNNT pore, which indicates that the particle would prefer

to remain further away from the BNNT surface. The isoline of zero net force shows the locus of the points of equilibrium of the wall-particle and water-particle force.

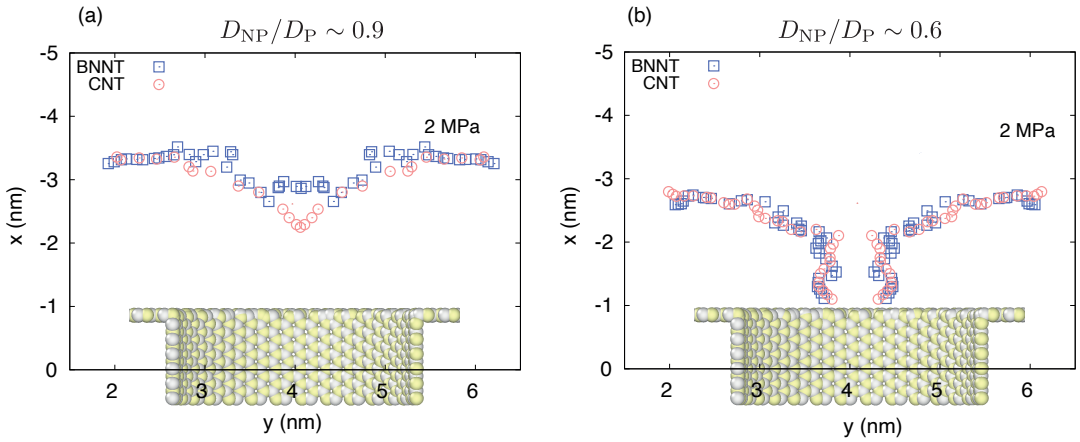

Figure 5.8: Isoline of zero force for BNNTs and CNTs obtained from Figure 5.7. (a) For D_{NP}/D_P = 0.9, the isolines lie closer pore for CNTs than for BNNTs. (b) For D_{NP}/D_P = 0.6, the isolines enter the pore for both BNNTs and CNTs.

5.2.3 Summary of MD simulations

BNNTs are shown to provide higher flow rates for D_{NP}/D_P of 0.9 and 1.0 at membrane pressure drops between 0.5 and 4 MPa. For $D_{NP}/D_P \sim 1.0$, higher flow rates in BNNTs were observed up to 10 MPa, which is the highest pressure we studied. The particle remained further away from the BNNT surface than from the CNT surface at low pressures of 2 MPa, aided by the electrostatic repulsion felt from the membrane. The electrostatic repulsion also pushed the equilibrium surface further away from the membrane surface for the BNNT. At higher pressures, however, the motion of the particle is restricted by the electrostatic forces as the equilibrium surface likely moves closer to the membrane, resulting in a drop in flow rate for BNNTs.

5.3 CFD studies

(Disclaimer: This part of the study has been carried out by Saeed Mazinani at the University of Bath)

A planar, 2D particle–pore system with D_{NP}/D_P=0.85 (D_{NP} = 19.2 nm) was simulated using a system of differential equations, and the equations were solved using the commercially available CFD package, COMSOL Multiphysics v5.4. The domain setup is depicted in Figure 5.9.

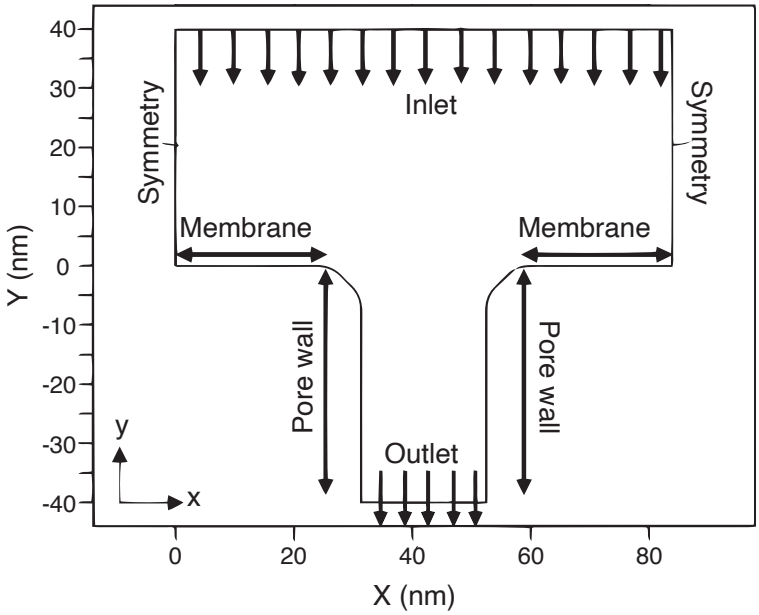

Figure 5.9: Simulation domain for CFD based study.

A pressure boundary condition was applied to the open end of the fluid reservoir, and the pore outlet velocity was set to match those obtained from the experiments in section 5.4. The fluid motion was solved using the continuity and Navier-Stokes equation. The particle motion was solved using the Langevin equation:

$$m_p \frac{du_p}{dt} = F_D + F_E + F_B, \tag{5.1}$$

where m_p is the mass of the particle, u_p is the particle velocity, and the forces are:

- Drag force F_D due to relative motion between particle and fluid:

$$F_D = 3\pi\mu D_{NP}[K_p u_p - K_f u_f], \tag{5.2}$$

  where K_p, K_f are hydrodynamic factors, μ is the fluid viscosity, u_f is the fluid velocity and u_p the particle velocity.
- Electrostatic force F_E due to the electric double layer present in front of the charged BNNT membrane modelled based on the work by Richard Bowen *et al.* (1999):

$$F_E = \frac{2\pi\kappa\varepsilon_r\varepsilon_0}{g}\left[\frac{2\zeta_c\zeta_m e^{k[h-\frac{D_{NP}}{2}]} - (\zeta_m^2+\zeta_c^2)}{e^{2k[h-\frac{D_{NP}}{2}]}-1}\right], \tag{5.3}$$

  where $\varepsilon_0\varepsilon_r$ is the electrical permittivity of water, k is the inverse of the Debye length, g is a steric factor, h is the distance between the particle and the pore, and ζ_m, ζ_c the zeta potential of the membrane and the particle, respectively, obtained from experiments.

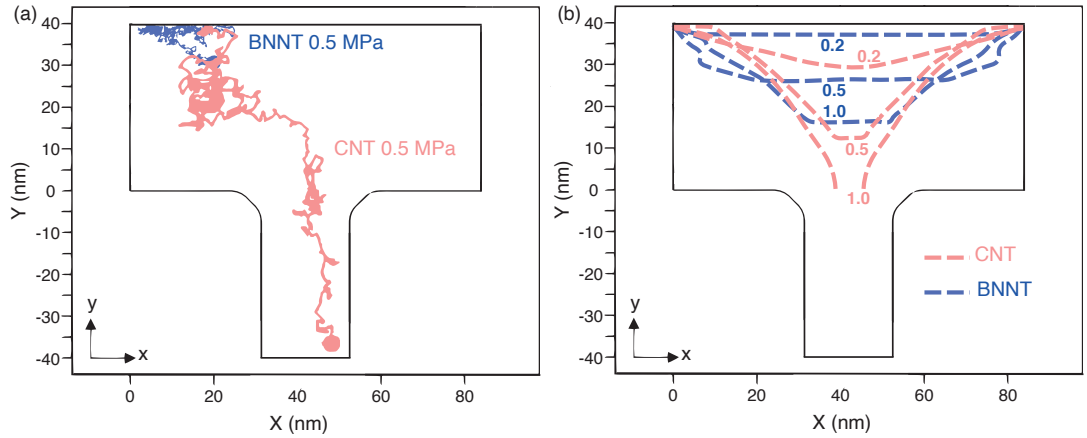

Figure 5.10: (a) Particle trajectories in front of BNNT and CNT membrane. The particle stays away from the BNNT membrane but enters the CNT membrane. (b) Isolines of zero net force with the random Brownian force removed. The lines are closer to the pore for CNTs at all pressures. Results from CFD studies.

- Brownian fore F_B was modelled using the Gaussian white noise method:

$$F_B = \iota \sqrt{\frac{6\pi\mu D_{NP} k_B T}{\Delta T}}, \tag{5.4}$$

  where ι is a unit vector generated randomly and ΔT is the timestep for the simulation, set as 10^{-7}s here.

The trajectories of the particle in front of the BNNT and CNT membrane is plotted in Figure 5.10 (a). By turning off F_B, a better estimate of the location of the isoline of zero net force is obtained and plotted in Figure 5.10 (b). It can be observed that the isoline lies further away from the membrane surface of BNNTs at all pressures studied, indicating the reduced likelihood of the particle coming closer to the pore and blocking it.

5.4 Experimental study

(Disclaimer: This part of the study has been carried out by Serena Casanova and Davide Mattia at the University of Bath)

Rejection characteristics of membranes made of CNTs, BNNTs and anodic alumina (AAMs) were studied experimentally to verify both rejection and permeation characteristics of the membranes in a laboratory setup. Anodic alumina served as a base template on which CNT and BNNTs were grown (see Figure 5.11). The AAM on its own (without any deposition that create the nanotubes) served as a benchmark for comparison.

5.4.1 Experimental setup

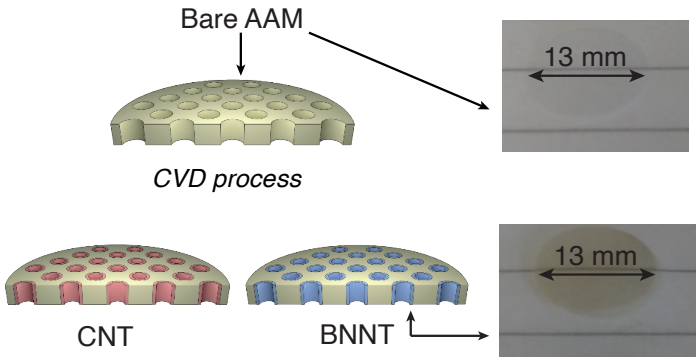

Figure 5.11: Schematic of the deposition of CNTs and BNNTs in AAMs, alongside optical pictures of the AAM template before and after BN deposition.

BNNT and CNT membranes were first grown on a circular porous disc-shaped template of anodic alumina through chemical vapour deposition (CVD). The base alumina disc had a radius of 13 mm, and pore diameters ranging from 10 nm to 30 nm. The disc thickness (and therefore the nanotube length) was 50 μm. The composition and structure of the membranes after deposition was verified through FESEM and EDX scans (see Figure 5.12), which showed that the membranes had a clean surface with open pores, and uniform deposition of atoms. High-resolution XPS spectroscopy (Figure 5.13(a) showed a BN stoichiometric ratio of 1.2, which is close to the theoretical value of 1. The FTIR peak (Figure 5.13(b) for the B-N in-plane bond in BNNT membranes was observed at 1375 cm^{-1} which is close to the value reported in the literature (Lei *et al.* (2015)).

The pH dependant zeta potential of the membranes was measured, and BNNT membranes showed a high negative zeta potential as expected, with zeta potential increasing at higher pH values. Silica and haematite nanoparticles were used for testing the rejection performance of the membranes. Silica particles had a negative zeta potential, indicating a negative surface charge while haematite particles had positive zeta potential and charges. Silica particles had diameters varying from 9.2 to 27 nm, while haematite particles had diameters between 15.8 and 37.3 nm. The zeta potential of the particles are outlined in Table 5.1 .

A custom-made dead-end filtration setup (Figure 5.14) was used to test the nanotube membranes. The pressure was applied through the use of a syringe pump with a controllable flow rate. The dead-end filtration cell was connected to a flow measurement apparatus, and the transmembrane pressure was recorded using pressure transducers with a resolution of ± 5 kPa. For each membrane, the permeance χ_p was calculated by taking the average of at least two measurements of volumetric flow rate Q and transmembrane pressure drop P using the following formula $\chi_p = Q/PA$, where A is the surface area of the membrane. Pure water permeance tests were carried out first, followed by rejection tests. Rejection performance was

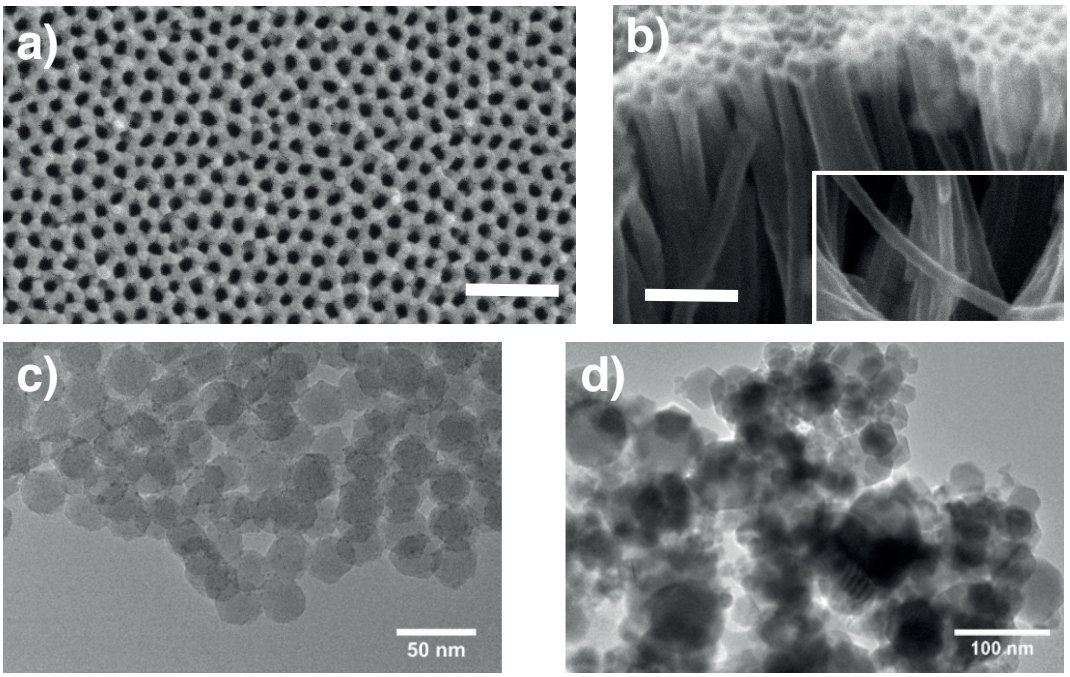

Figure 5.12: FESEM micrograph of (a) BNNT membrane surface, (b) individual nanotubes released from a cracked membrane after CVD. The scalebars represent 200 nm. (c) TEM micrograph of silica nanoparticles. (d) TEM micrograph of haematite nanoparticles

Table 5.1: Zeta potential of nanoparticles

$\mathbf{D}_{NP}$ **(nm)**	ζ_c **(mV)**
Silica	
9.2 ± 1.8	-12.7 ± 0.6
14.7 ± 1.8	-27.4 ± 1.9
19.2 ± 2.6	-18.5 ± 1.9
27.1 ± 3.2	-37.6 ± 4.1
Haematite	
15.8 ± 2.2	8.6 ± 1.5
17.2 ± 2.2	3.8 ± 1.6
37.3 ± 4.2	19.9 ± 0.2

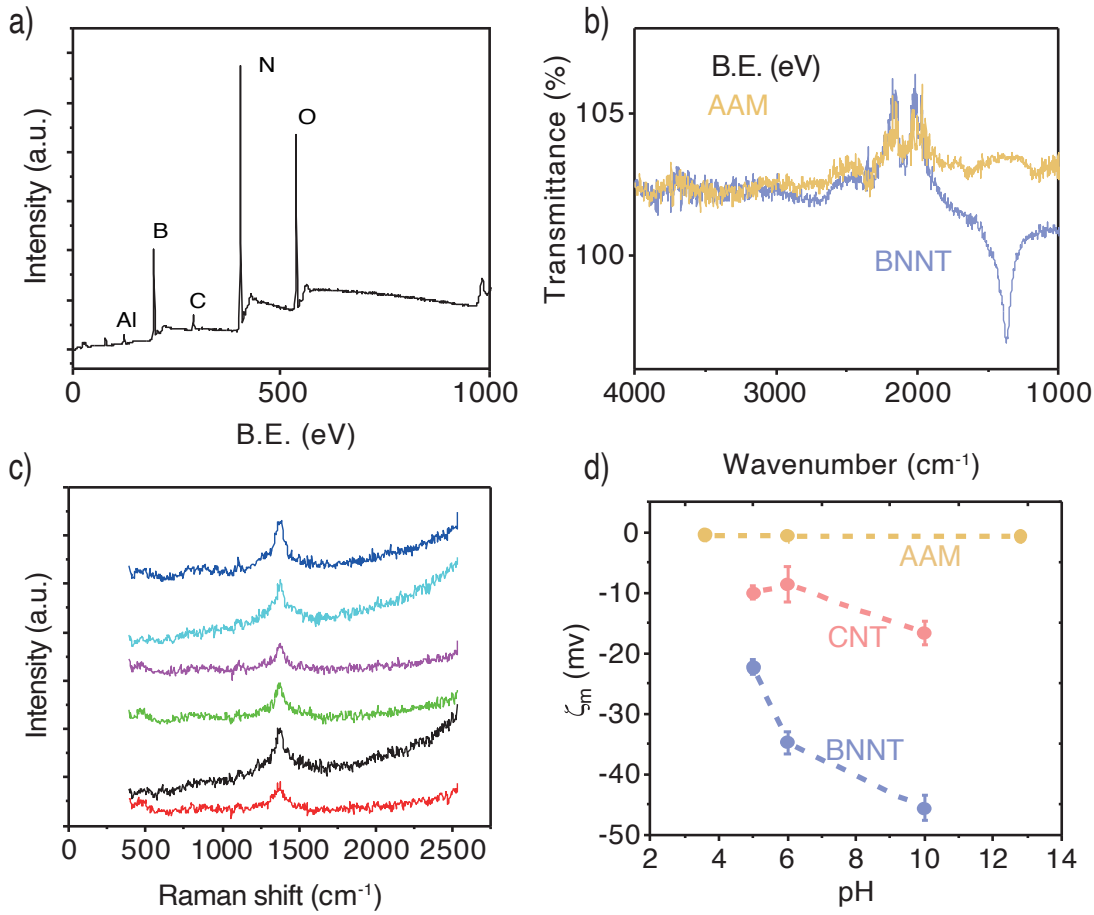

Figure 5.13: (a) XPS and (b) FTIR spectra of BNNTs. (c) Raman analysis of the BNNT membrane top and bottom surface at different locations on the sample. (d) Surface zeta potential (ζ_m) reported as a function of pH for the 3 membrane materials.

tested in a crossflow setup, based on a bored-through tee in a dead-end flow cell. The feed water was pumped in normal to the membrane surface and left through the sides after passing through the membrane. The retentate, or the part of the solution which did not go through the membrane, was removed by a tee bored in the side of the feed line. The feed line was thoroughly cleaned and dried after each experiment. The concentration of the particles in the permeate was calculated using UV-Vis spectroscopy on the first few drops of the permeate. The membranes were cleaned by slow backflushing after each rejection test. The rejection characteristics for silica nanoparticles was tested first, followed by those for haematite nanoparticles. Rejection R(%) was calculated using the equation

$$R(\%) = \left(1 - \frac{c_{permeate}}{c_{feed}}\right) \times 100, \tag{5.5}$$

where $c_{permeate}$ is the concentration of particles in the permeate solution while c_{feed} is the concentration of particles in the feed solution.

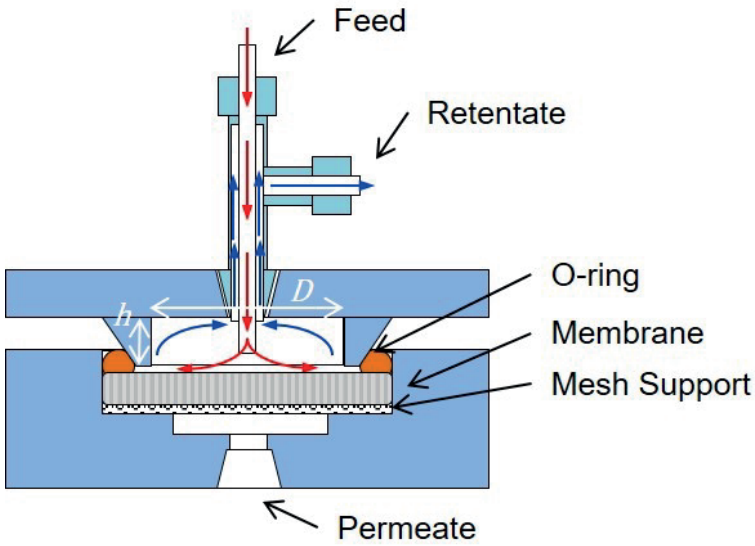

Figure 5.14: Cross flow filtration cell setup.

5.4.2 Experimental results

Contact angle

Optical micrographs of a droplet in contact with the membranes is shown in Figure 5.15. Contact angle measurements for both BNNTs and CNTs showed a macroscopic water contact angle of 78±2°, while the bare AAMs had a contact angle of 21±2°. The contact angles for CNTs are in good agreement with literature (Mattia and Gogotsi (2008)), but are slightly higher than the reported values for BNNTs (Wu *et al.* (2016)).

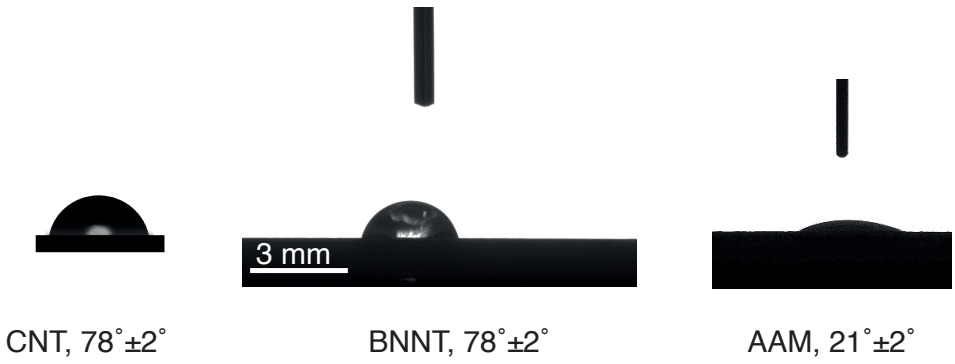

Figure 5.15: Optical micrograph of a water droplet and associated contact angle for each material.

Flow and rejection results

Tests with pure water show that the CNT membrane outperforms the BNNT membrane, with CNT membranes providing about 1.8 times the flow rate of BNNT membranes. This is roughly in line with experimental observations for single nanotubes (Secchi *et al.* (2016)) and with the MD results. The method of synthesis of the nanotubes, i.e. non-catalytic CVD on alumina template is prone to producing defects in the membrane. These defects are also responsible for the high zeta potential when the membrane is in contact with water. BNNTs show higher rejection of negatively charged silica particles than both CNTs and bare AAMs for all diameters of the particles tested, diameters both larger and smaller than the average membrane pore size (Figure 5.16). In contrast, AAMs and CNTs show appreciable rejection of silica nanoparticles only when the particle diameter D_P is larger than the nanopore diameter D_{NP}. BNNT membranes with $D_P = 21.2 \pm 3.7$ could reject 71% of silica nanoparticles with $D_{NP} = 19.2 \pm 2.6$ nm, with a permeance of 8.65 ± 0.06 Litres/m^2/hour/bar, whereas CNT membranes with a similar pore size showed a rejection of only 27% at a comparable permeation rate. AAMs show a slightly higher rejection rate at 38% for particles of this size, but the pore size for AAMs is slightly smaller than the particle itself. For particles with diameter $D_P = 14.7 \pm 1.8$ nm, which is smaller than the pore size of both AAMs and CNTs, CNTs show a rejection of 40% compared to only 18% for AAMs. Since BNNTs show a much higher rejection of silica compared to both CNTs and AAMs, increasing the pore diameter by up to 30% to match the rejection of CNTs would allow up to 70% increase in the permeation rates, since the mass flow rate through a membrane is directly proportional to the cube of the pore diameter.

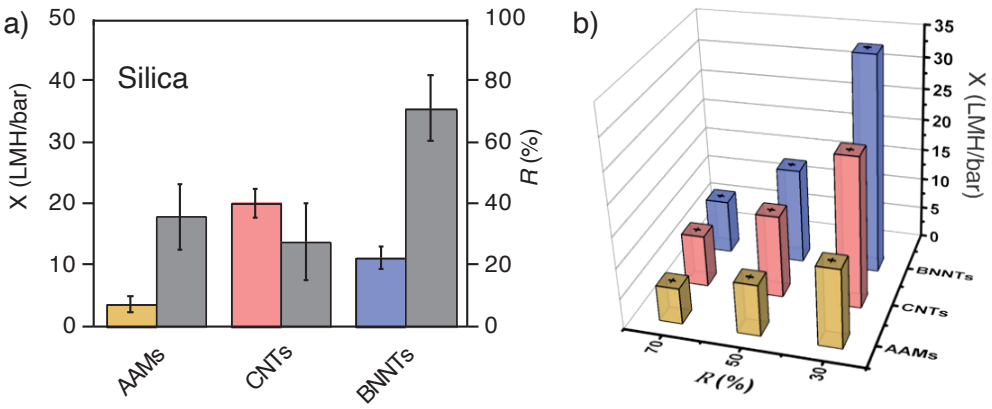

Figure 5.16: Experimental permeance χ and rejection R for negatively charged silica (pH = 5.5) nanoparticles with diameter smaller than the average CNT and BNNT and comparable with the AAM ($D_{NP} \leq D_P$). (b) Permeance vs rejection data for all three membranes against silica nanoparticles.

5.5 Conclusion

The choice of using BNNT membranes for the removal of negatively charged particles from water can result in up to 70% higher water flow through the membrane compared to CNTs. At D_{NP}/D_P ratio of 0.9 and applied pressure of 2 MPa, MD studies showed that BNNTs could offer a flow rate of 2.6×10^{-15} kg/s, compared to the 1.7×10^{-15} kg/s observed in CNTs. This is largely due to the added mechanism of electrostatic repulsion for particle rejection, which also allows for the usage of much wider BNNTs. Computational studies were used to show the mechanism of the charge-based rejection. MD studies identified higher flow rates through BNNTs at low pressures while the particle is rejected due to the particle being unable to come very close to the membrane pore and therefore present less pore-blocking as compared to the CNT membrane. For D_{NP}/D_P ratio of 0.9, the particle stayed 3.5 nm away from a BNNT pore, compared to the 1.5 nm distance maintained from a CNT pore at an applied pressure of 2 MPa. The mobility of the particle in front of the BNNT was also found to be higher than in front of the CNT under the conditions of low-pressure drop across the membrane. Finally, the shifting of the equilibrium surface away from the membrane surface was identified and also confirmed through CFD studies. Both experiments and simulation have shown that BNNTs can reject nanoparticles that are 30% smaller than their diameters for pressures of up to 6 MPa. This implies that BNNTs ought to be preferred in applications that require the selection of negatively charged particles from the water alongside high permeation rates.

Chapter 6

Nanoscale antifouling using direct membrane heating

6.1 Introduction

In section 2.4, the economic costs of fouling on desalination membranes were outlined, with biofouling alone resulting in additional costs of USD 15 billion annually (Abdul Azis *et al.* (2001)). Flemming (1994) and Ang *et al.* (2017) put the costs due to fouling and associated cleaning between 30–50% of the total membrane operating costs, while also decreasing membrane life by up to 66%. As noted by Elimelech and Phillip (2011) and Werber *et al.* (2016a), further improvements in membrane permeance are unlikely to bring down desalination costs substantially. Membrane fouling, therefore, could potentially be an area where substantial cost reductions can be made through investigations into antifouling and cleaning technologies, alongside the focus on selectivity described in the earlier chapters.

The reason foulants grow on membranes varies depending on the specific type of feedwater and membrane used for the filtration process. Some feedwater may be high in inorganic salts, while others may contain oils, or be rich in micro-organisms and naturally occurring organic matter. As explained in chapter 2, most fouling happens first through the deposition of seed particles, usually a few molecules of the foulant. These molecules can be a few nanometres across, as in the case of the most common organic foulants, or even smaller, as in the case of inorganic salts. Chemical cleaning of such varied types of fouling necessitates the use of different agents which target a few specific types of foulants. This non-generalizability of chemical cleaning agents adds to the multiple other drawbacks associated with it, such as the inability to remove the initial seed particles, the need to stop the desalination process, the degradation of the membrane due to harsh chemicals used and the chemical-laden wastewater disposal problem, outlined in section 2.4.2.

Physical cleaning of membranes, especially using ultrasonic vibrations (Bilad *et al.* (2013); Chai *et al.* (1998); Chen *et al.* (2006); Kobayashi *et al.* (1999); Kokugan *et al.* (1995); Li *et al.* (2002); Lim and Bai (2003); Masselin *et al.* (2001); Matsumoto *et al.* (1996); Zhao *et al.* (2018)) and heat-based membrane cleaning (Aumeier *et al.* (2018); Lohaus *et al.* (2020);

Miyoshi *et al.* (2009); Nguyen *et al.* (2020)) offer a way out of the problems associated with chemical cleaning. They can be applied frequently — as the desalination process need not be stopped during the cleaning, and they do not need the membrane to be flushed of chemicals before use. Heating has been shown to act both as a physical cleaning mechanism (Aumeier *et al.* (2018)) and as a biological deterrent (Lohaus *et al.* (2020)), thereby promising general cleaning ability against a wide range of foulants.

While heat-based antifouling and cleaning have been studied experimentally at the macroscale, its feasibility in removing nanoscale particles and a clear understanding of the mechanisms behind such removal is missing. Lohaus *et al.* (2020) has referred to induced shear flows, and Aumeier *et al.* (2018) refer to vapour expansion inside nanopores as possible mechanisms of cleaning, but the process of heating is likely to encourage a large number of phenomena, including bubble and vapour-film formation in addition to the above-mentioned processes. The possibilities of the rich dynamics of the interactions between the nanoscale pore and particle necessitate a molecular-level study on the feasibility and mechanisms of nanoscale particle removal using heated membranes.

6.2 Theoretical background

When a nanoparticle in a pressurised fluid nears a heated membrane pore, several forces may be acting on it. These include the attractive van der Waals forces (F_{vdW}) between the nanoparticle and the wall, and the pressure force from the fluid (F_{press}) as it is forced into the pore. These two forces collectively move the nanoparticle towards the wall. On the other hand, forces that might push the nanoparticle away from the pore include the repulsive van der Waals force at a very small wall-particle distance, the lubrication force (F_{lub}) as the fluid is squeezed between the nanoparticle and the pore, and the bubble force (F_{bubble}) due to the formation of expanding bubbles within the pore and on the membrane surface. In addition, the Brownian force ($F_{Brownian}$) arising due to the heated fluid surrounding the nanoparticle, and the drag force (F_{drag}) are also likely to be playing a role in its displacement. The forces and their directions are depicted in Figure 6.1. $F_{Brownian}$ and F_{drag} are not depicted since their directions are not constant.

The force components are dependent on several parameters: F_{lub} is dependent on the particle – pore distance and the flow rate of water around the nanoparticle, which itself is dependant on the particle-pore distance, F_{drag} is dependant on the relative velocity of the nanoparticle and the fluid surrounding it, which depends on F_{press}, the particle-pore distance, and other parameters. Thus, a majority of the forces are interdependent, and obtaining an analytical solution is difficult. $F_{Brownian}$ acting on the nanoparticle should be numerically zero only when averaged over a finite interval of time, indicating that the Brownian component of force may not be separable at a given instance of time when all other components of the force are also

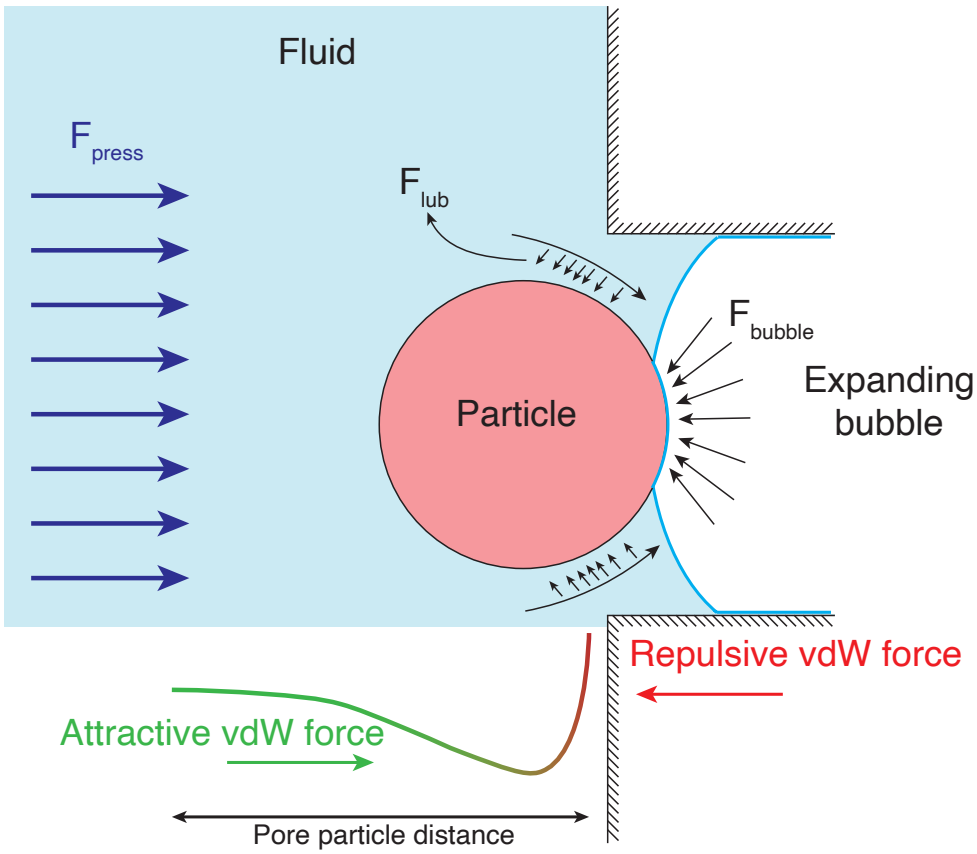

Figure 6.1: Depiction of forces acting on a nanoparticle near a heated pore.

changing over the time interval. While the fluid atoms exert forces on the nanoparticle through multiple different mechanisms, including F_{press}, F_{lub}, F_{bubble}, $F_{Brownian}$ and F_{drag}, it is impossible to retrieve all these force components individually from an MD simulation. Instead, the forces acting on the nanoparticle may be summarized as the water-nanoparticle force, F_{water}, and the nanoparticle-membrane force, $F_{membrane}$.

Estimates of force components

While it might be impossible to extricate the components of F_{water} from MD, certain assumptions about their order of magnitudes may be made.

- $F_{Brownian}$: The magnitude of $F_{Brownian}$ may be estimated by Equation 5.4 obtained from Casanova *et al.* (2020b). For a nanoparticle of $D = 4$ nm, $F_{brownian}$ is of the order of 10^{-9} N.
- F_{press}: The pressure force F_{press}, assuming a 10 MPa pressure acting uniformly on one side of the nanoparticle, is of the order of 10^{-11} N. Desalination plants typically pressurize water to a few MPa.
- F_{drag}: The drag force F_{drag} is of the order of 10^{-11} N at a nanoparticle velocity of 1 m/s and scales linearly with the velocity.
- F_{lub}: The lubrication force F_{lub} is expected to have a similar order of magnitude as F_{drag} (Vázquez-Quesada and Ellero (2016)).
- F_{bubble}: Assuming a bubble formed at 650 K and 22 MPa, the critical point of water, covering half the nanoparticle surface to maximize F_{bubble}, F_{bubble} is of the order of 10^{-10} N.
- F_{vdW}: For nanoparticle-membrane ε values of the order of 0.01 kcal/mol, the attractive component of F_{vdW} is of the order of 10^{-10} N. Stronger interactions at ε values of 0.1 kcal/mol and higher result in $F_{vdW} >$ the order of 10^{-9} N, and heating alone would be insufficient to dislodge the nanoparticle.

This makes it evident that among the components of F_{water}, $F_{Brownian}$ is the highest by an order of magnitude, followed by F_{bubble}. The dominance of $F_{Brownian}$ over all other forces from the order of magnitude analysis suggests that individual MD simulations of nanoparticle removal must be treated with caution, and ideally, a large ensemble average across multiple realisations of the same conditions must be considered to draw observations from MD. Since MD as a method is computationally expensive, it is not currently feasible to carry out large ensemble studies while varying all the parameters of interest. Larger-scale methods, such as Langevin solvers, which implement the Langevin equations of motion, might prove to be useful to study nanoparticle motion within a certain range of conditions. While they may not model bubble nucleation, they can model $F_{Brownian}$ and F_{vdW}, the two dominant forces on the nanoparticle. For cases where bubble formation is not expected, a Langevin solver could potentially be a useful tool to study the motion of the nanoparticle in an attractive nanoparticle-membrane well under the influence of high-temperature Brownian forces.

The process of nanoparticle removal due to heating may depend on a number of factors: the temperature of the fluid, the mass of the nanoparticle, the presence of expanding bubbles, the geometry of the pore and nanoparticle, and the nanoparticle-membrane, nanoparticle-water and water-membrane interaction strengths. For simplicity, the nanoparticle was chosen to be spherical, with the diameter kept equal to the pore diameter. The water-particle and water-membrane interactions were held fixed. The parameters which were varied were the temperature of the membrane and the nanoparticle-membrane interaction strength, as they are the largest contributors to F_{water} and $F_{membrane}$ respectively, the two principal forces acting on the nanoparticle. The temperature was varied from 300 K to 650 K, i.e., from room temperature to the critical point of water. Temperatures beyond the critical point were not considered due to the associated complexities. Furthermore, the dominance of $F_{Brownian}$ suggests that a definitive statement about whether a nanoparticle will be removed or not given a set of conditions cannot be made. This is due to the random nature of the Brownian force, which might remove or re-deposit the nanoparticle at any instant of time. A nanoparticle was considered removed if the distance of all of its atoms from the membrane was larger than the cutoff distance for LJ interactions. Rare events of high $F_{Brownian}$ could potentially remove the nanoparticle at any point in time, however, for this study, conclusions can only be drawn for the finite amount the simulations are carried out - usually a few nanoseconds, with an indicative probability drawn from a few realisations of the same initial conditions. It is to be noted that for the purposes of this study, heterogeneous bubble nucleation due to presence of dissolved gasses and other particulate matter is not considered. Such dissolved substances are likely to act as nucleation sites, resulting in higher bubble nucleation rates and therefore presenting a higher probabilty of particle removal.

6.3 Simulation setup

For the MD simulation, two setups were considered: The first one with a nanoparticle stuck in front of a membrane pore (Figure 6.2; Setup 1), and the second one with a nanoparticle on a wall, without any pore (Figure 6.2; Setup 2). For both setups, only the membrane is heated to the desired temperature. The membrane geometry is maintained by the use of the spring potential, described in section 3.2.3.

First setup:

The first setup consists of two reservoirs of water on either side of the membrane, each of lengths $7.0 \times 8.23 \times 8.23$ nm in the x,y and z directions, respectively. The reservoirs are each initially filled with 15880 TIP4P/2005 (Abascal and Vega (2005)) water molecules each at a temperature of 300 K and pressure of 10 MPa, with a few water molecules deleted to accommodate the nanoparticle. The membrane is modelled using an fcc lattice with a lattice constant of 0.392 nm. The membrane is given a thickness of 12 lattice units, with a pore of D = 4.068

nm constructed by deleting all atoms which occupied a cylindrical region of the same diameter passing through the centre of the membrane. This setup is more prone to bubble formation than setup 2, due to the large contact area between the liquid and the heated pore, and is more likely to have a complex flow field as the fluid flows past the nanoparticle inside the pore and is expelled out of the pore as it gets heated.

Second setup:

The second setup consists of a single reservoir with the dimensions $10.0 \times 8.23 \times 8.23$ nm in the x,y and z directions and is filled with 22686 water molecules initially. The initial temperature of the water molecules was set as 300 K, while the pressure was kept constant at 10 MPa. The membrane was also made of an fcc lattice with a lattice constant of 3.92 Å in the shape of a wall with a thickness of 2.5 lattice units. This setup avoids the complexities of flow into a heated pore past a nanoparticle and presents a simpler benchmark case.

A nanoparticle of D = 4.068 nm consisting of 790 atoms is placed at a distance of 1.8 nm from the pore (consequently partially inside the pore) for the first setup and at 2.4 nm from the membrane wall for the second setup. The atoms on the nanoparticle are uniformly spaced, creating a single-atom-thick spherical shell. The piston, consisting of a 2-D sheet made of 2508 atoms, is used to apply pressure on the water in its corresponding reservoir using the method described in section 3.7.1, with a force of 0.0033 kcal/mol Å applied to each atom on the piston, creating a pressure of 10 MPa. The interaction potentials used are listed in Table 6.1.

pair	ε **(kcal/mol)**	σ **(Å)**
O-O	0.1852	3.1589
O-particle	0.1912	3.4330
O-membrane	0.3000	2.8150
O-piston	0.3000	3.0000
particle-membrane	0.0100	3.7064
H-all	0.0000	0.0000

Table 6.1: Interaction parameters used in this study for nanoparticle removal at a heated membrane surface

Bubble formation in the water reservoirs is calculated by populating the simulation domain with pseudo-atoms in a uniform grid at the end of the simulation. Oxygen atom positions from the simulation output are then compared against the positions of the pseudo-atoms to generate a pseudo-atom-oxygen co-ordination number for each pseudo-atom at every timestep. This co-ordination number is akin to the local density at the location of a pseudo-atom. Water in the liquid state would have a larger number of oxygen atoms surrounding the pseudo-atom within a given radius, while water in the vapour phase will have a lower number of oxygen atoms. A coordination number cutoff corresponding to a density of 57 kg/m^3 is chosen as the cutoff for

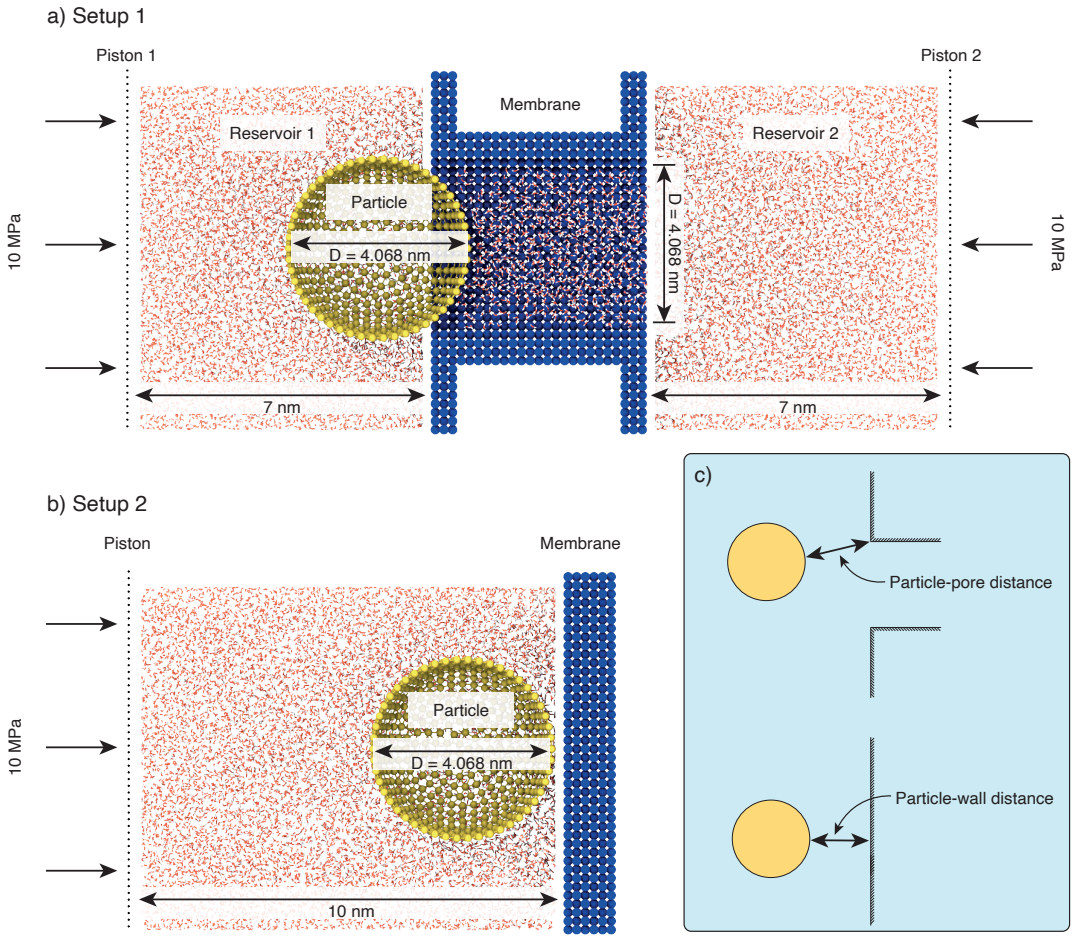

Figure 6.2: MD setup for nanoparticle removal using membrane heating. (a) Setup 1 consists of a nanoparticle stuck in a membrane pore. (b) Setup 2 consists of nanoparticle next to a membrane surface without any pore. (c) Parameters used to analyse nanoparticle removal. Particle-pore distance refers to the shortest distance between an atom on the nanoparticle and another on the rim of the membrane pore. Particle-wall distance refers to the closest distance between an atom of the nanoparticle and a membrane wall atom.

identifying whether the region around the particular pseudo atom is in liquid or vapour phase. The density cutoff chosen is close to the highest vapour density of water at 10 MPa pressure, at any given temperature.

6.4 Results

6.4.1 Modes of nanoparticle removal

For the setup with a membrane pore, MD studies at different membrane temperatures between 300 K and 650 K show three distinct modes of nanoparticle removal depending on whether a bubble forms or not (Figure 6.3a). At 650 K, a bubble starts forming within the pore and surface of the membrane near-instantaneously and expands across the lateral periodic boundaries to form a film on the surface, pulling the nanoparticle along with it (Figure 6.4a). At lower temperatures of up to 600 K, bubble formation inside the pore and around the nanoparticle is observed, resulting in the nanoparticle being pushed away from the surface (Figure 6.4b). At temperatures below 575 K, which is the saturation temperature at 10 MPa absolute pressure, bubble formation rarely occurs. Nanoparticle removal below 575 K is therefore dominated by Brownian forces, and in comparison take much longer to be removed. The distinct modes are not very evident for setup 2, where there is no pore, only the membrane wall (Figure 6.3b). This is likely due to the difficulty of bubble formation in the absence of the heated pore. The pore provides a heated region with a large surface area in a constricted volume and aids bubble formation, producing much larger bubbles. In contrast, the nanoparticle-membrane interfacial region is unable to support the formation of large bubbles, creating only small bubbles which therefore do not influence much the release of the nanoparticle from the energy field of the membrane wall (Figure 6.5). Not only are the bubbles in setup 2 smaller, the film which forms over the surface at 650 K also appears nearly two nanoseconds later compared to setup one, at 5.0 ns, against the 3.3 ns for setup 1 (Figure 6.3). However, for both setups, at practical temperatures that membranes may be able to withstand, bubble formation is rare and small, and the nanoparticle motion is likely to be dominated by Brownian forces alone. Nanoparticle removal for both setups was not observed at or below 500 K.

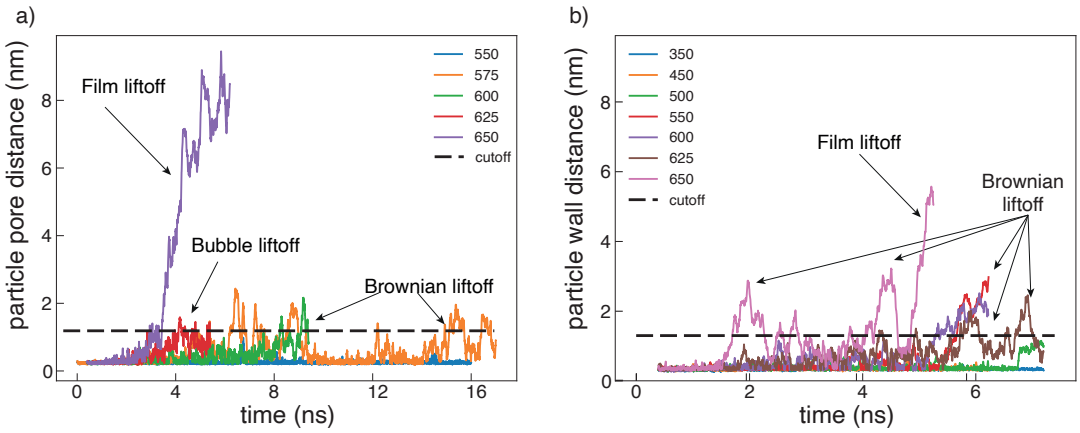

Figure 6.3: Modes of nanoparticle liftoff in (a) setup 1 and (b) setup 2. Setup 1 shows three distinct modes of liftoff, while setup 2 only shows two such modes. The horizontal black dashed line indicates the cutoff distance (= 1.3 nm) beyond which there is no LJ interaction between the membrane and the nanoparticle. Film formation in setup 2 occurs nearly a nanosecond later than for setup 1, by which time Brownian forces have already moved the nanoparticle away from the surface twice. At practical temperatures, nanoparticle removal for both setups is dominated by Brownian forces.

6.4.2 Role of Brownian forces

Brownian forces were seen to dominate the process of nanoparticle removal at lower, more easily accessible temperatures where there is little or no bubble formation. The dominating role of Brownian forces makes it difficult to predict whether a nanoparticle will be removed from a surface, and within what time. Multiple realisations of the same setup were carried out to establish the order of magnitude of the nanoparticle removal time, and to determine an estimate of the spread. A sample of the nanoparticle-membrane distance from such simulations at 450 K and 625 K is presented in Figure 6.6. As can be observed, the nanoparticle goes beyond the limit of the nanoparticle-membrane LJ interactions in only a few of the simulations at 450 K, while at 625 K, all of them do. The large role played by $F_{Brownian}$ shows up not only in the probability of nanoparticle removal but also in the wide spread of the time taken to remove the nanoparticle for both cases, which makes quantitative predictions about the rate of nanoparticle removal difficult. The probability of removal, which is the ratio of the simulations which show nanoparticle removal to the total simulations carried out, is presented in Figure 6.7. The increase in temperature results in an increased probability of the nanoparticle being removed, with all nanoparticles being removed at temperatures at and beyond 600 K, at which bubble formation takes place. Figure 6.6 (a) also clearly shows the importance of rare Brownian events — while Brownian forces largely make the nanoparticle move about a mean near the membrane wall, rare occurrences of high $F_{Brownian}$ directed away from the membrane remove the nanoparticle in a few concerted moves. The probability of removal is calculated

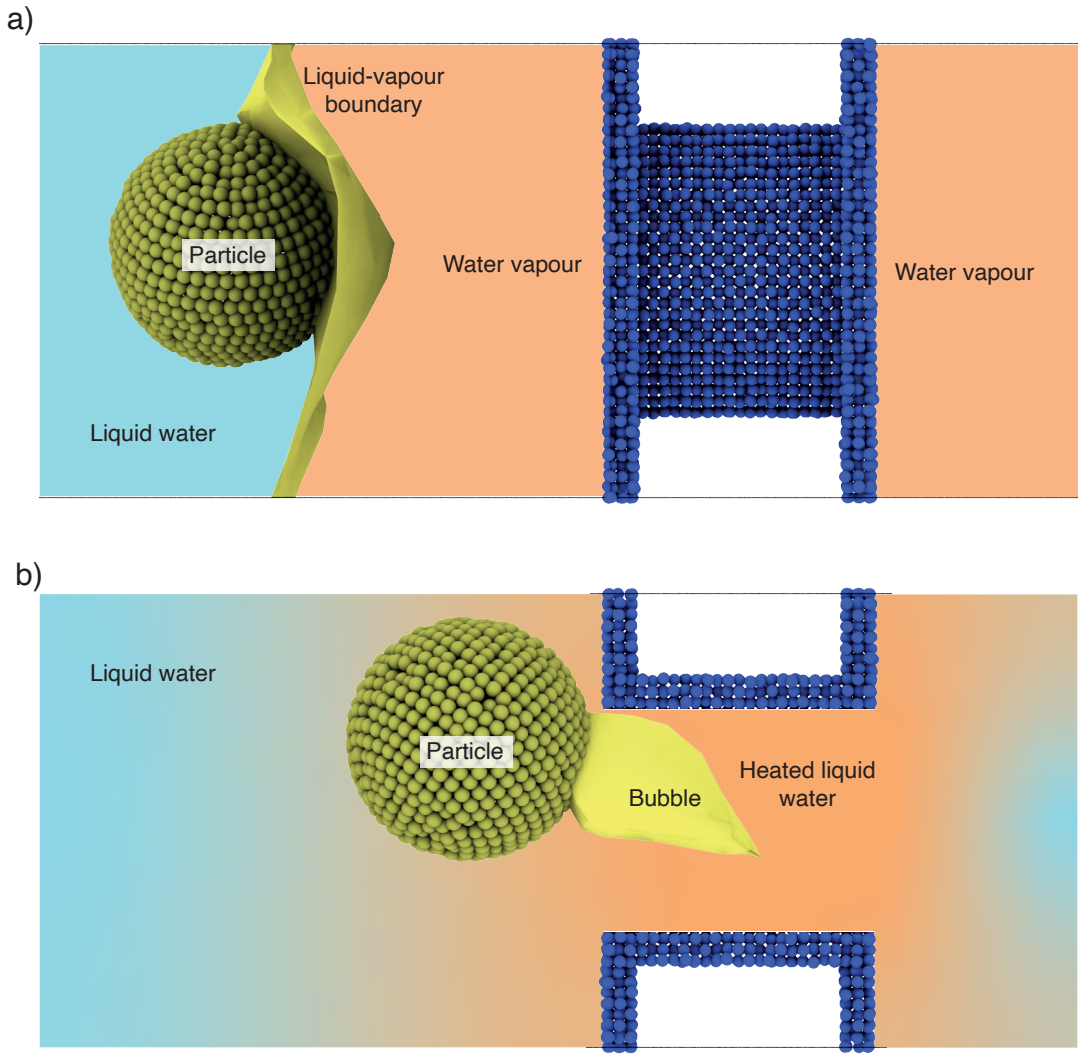

Figure 6.4: (a) nanoparticle removal due to vapour film formation over the membrane surface across the periodic boundary at 650 K. (b) Bubble formation inside the pore assists nanoparticle removal at 625 K.

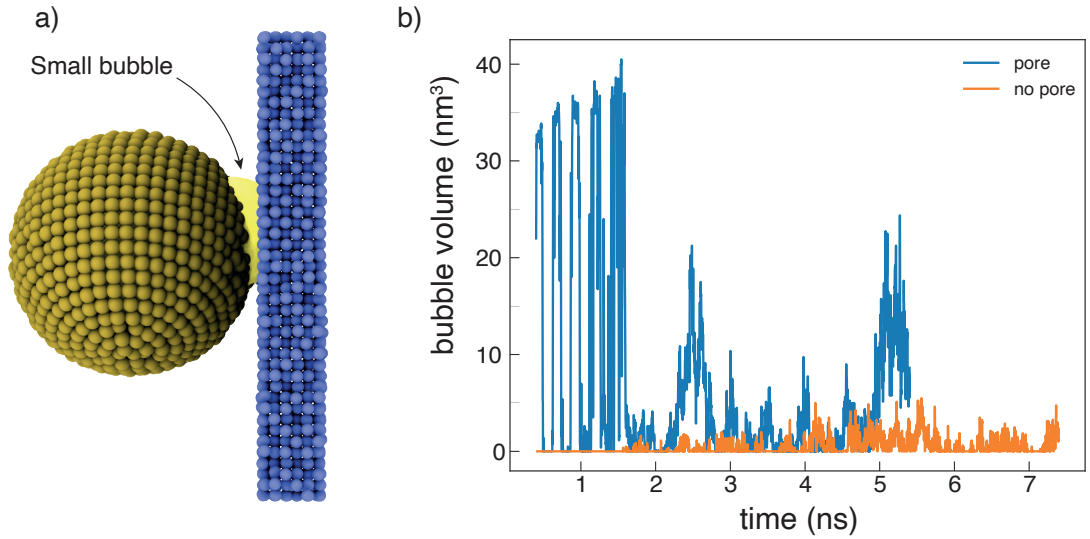

Figure 6.5: (a) A small bubble is formed in the region between the nanoparticle and the membrane wall with no pore. (b) The bubble volume for setup 1 (with a pore) is much larger than for setup 2 (without a pore). The small bubbles formed in setup 2 are unlikely to push the nanoparticle away from the surface. Membranes in both setups are heated to 625 K.

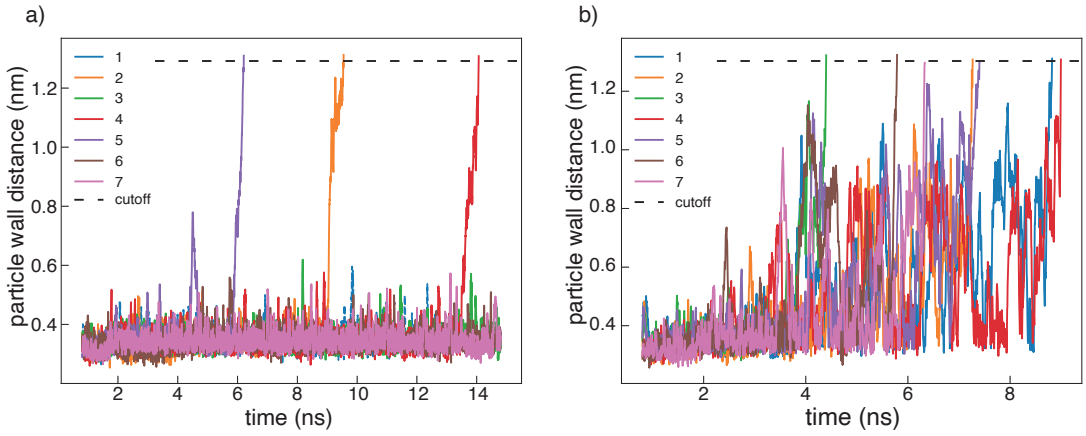

Figure 6.6: Particle-membrane wall distance vs time for (a) 450 K and (b) 625 K for setup 2. The different colours indicate different realisations of the same setup, initialised with different seeds. Only 3 nanoparticles are removed at 450 K, while all nanoparticles are removed at 625 K. Nanoparticle removal at 625 K is also faster than at 450 K.

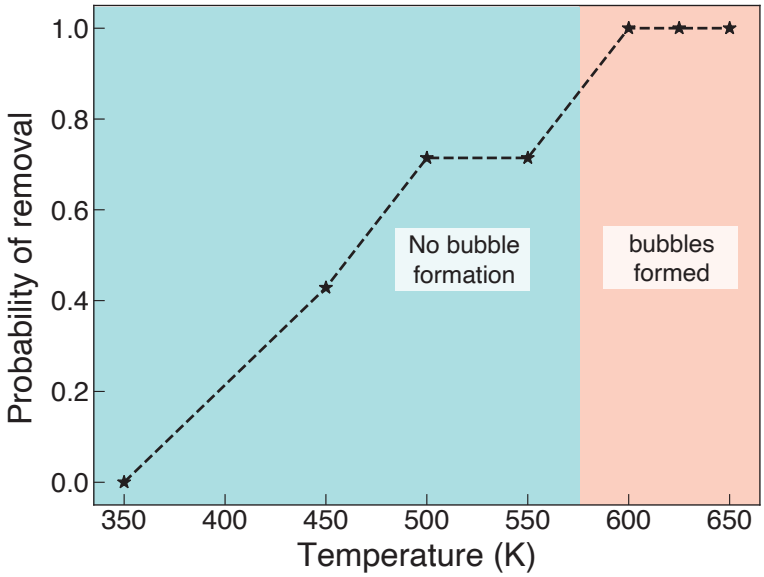

Figure 6.7: Probability of nanoparticle removal against membrane temperature for setup 2. Regions where bubbles formed or not are also indicated.

for only 15 ns of simulation time. This is likely to change if the simulation is run for longer, as more rare Brownian events are captured, which push the nanoparticle beyond the reach of the membrane's force field. However, the trend is expected to remain the same, with lower temperatures resulting in lower probabilities of removal. For those simulations which saw the nanoparticle being removed, increasing temperatures generally showed a decrease in the mean time it took for the nanoparticle to be removed, shown in Figure 6.8. At temperatures of 600 K and above, where bubbles form, a step change is visible both in the probability of nanoparticle removal and the mean time of removal. This likely indicates the diminishing role of the $F_{Brownian}$ and the increasing role of F_{bubble} in removing the nanoparticle at these temperatures.

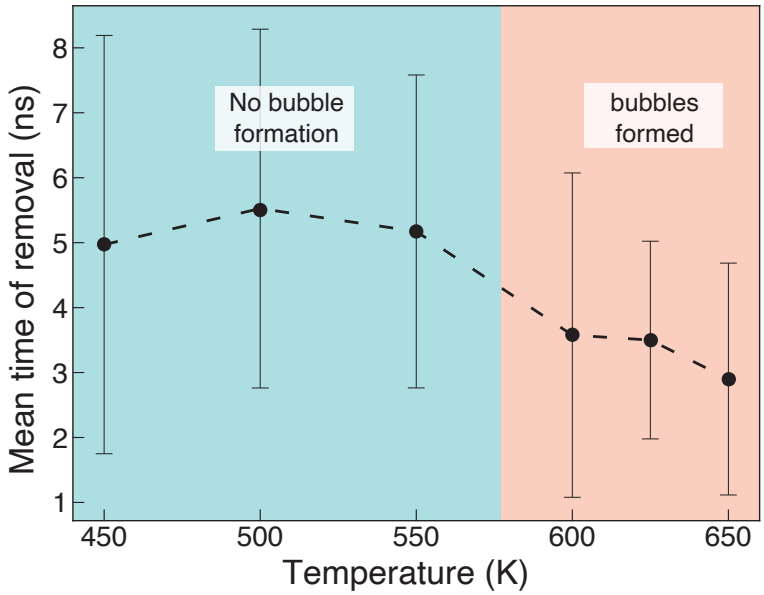

Figure 6.8: Mean time of nanoparticle removal against temperature. Times for nanoparticles which were not removed are excluded from the calculation of the mean.

6.5 Conclusions

Direct heating of a membrane is shown to be able to remove nanoparticles under pressure from the membrane surface through three different mechanisms — vapour film formation, bubble expansion and Brownian motion, with the contributory fraction of each of these processes depending on the temperature of the membrane. While bubble and film formation only happen beyond 575 K at an applied pressure of 10 MPa, Brownian forces play a role at all temperatures. The general nature of unpredictability of Brownian forces over short periods makes it difficult to establish conclusively whether a nanoparticle will be removed from a membrane surface or not. Only probabilities of removal within a finite time (of the order of nanoseconds) may be drawn from repeated realisations of the same simulation setup. The simulations showed that at 450 K, the probability of particle removal within 15 ns was 40%, while beyond 575 K, the probability was 100%. The mean time for particle removal between 450 K and 550 K was about 5.5 ns, and this dropped down to 3 ns beyond 575 K, likely due to bubble formation. The classification of F_{water} into its major constitutive components of $F_{Brownian}$ and F_{bubble} is difficult due to the arbitrary nature of the classification of a water molecule as belonging to a bubble or liquid depending on the density around it. The continuous formation and collapse of bubbles around the nanoparticle depends on the nanoparticle-membrane distance, alongside the finite time the nanoparticle takes to respond to the bubble, making it difficult to track and generalise the effect of F_{bubble} over long timescales and separate it from $F_{Brownian}$. While MD simulations have shown that direct membrane heating can remove nanoparticles stuck to the membrane surface, predicting the probability of nanoparticle removal given initial conditions

likely remains outside its purview. This would require very long simulation runtimes of up to a few seconds, to sample Brownian events which would be rare on a nanosecond scale but which are more likely to drive the nanoparticle away from the surface.

Chapter 7

Summary and Concluding Remarks

7.1 Summary

Chapter 1 and 2 introduced the increasing need for water desalination and filtration, driven by the ever reducing quantities of freshwater due to overuse and change in climate patterns. Water from the oceans appears as an attractive source for future needs, currently unattainable due to the high costs associated with desalination. Part of this cost arises due to basic thermodynamics — separation of salt ions from water requires a high input of energy. The total costs associated with desalination, should it replace our current sources of freshwater, would see the price of water increase by an order of magnitude (see Section 2.3). The largest consumer of energy in the desalination process has been the RO membrane, where feed water pressure is required to be raised to very high pressures to overcome the osmotic pressure and the pressure losses within the membrane. While osmotic pressure cannot be changed easily, pressure reduction is sought by reducing pressure losses within the membrane. This is done through the usage of novel nanomaterials, including zeolites, MOFs, 2-D materials like graphene, CNTs and BNNTs.

The focus on improved permeability resulted in the proposition of a large number of nanomaterial membrane candidates which offered orders of magnitude higher permeation compared to the currently used thin film composite (TFC) membranes, but it only resulted in a considerable decrease in the membrane sizes required, not operating costs. This was largely due to TFC membranes already operating close to the thermodynamic minimum of energy required to desalinate seawater, and the orders of magnitude increase in permeability could offer only a few percentage points decrease in energy consumption. Furthermore, smaller membranes with higher water flow through them, as nanomaterial membranes are likely to be, are more prone to fouling due to a larger volume of foulants accumulating over a smaller area. This highlighted the need to focus away from permeability and onto other avenues where membrane costs may be reduced. Apart from reverse osmosis at the membrane, other significant processes involved in desalination include pre and post-treatments. Both these steps are required due to the inability of the generic desalination membrane to effectively counter different kinds of feed waters and the solutes in them. Pre-treatment is needed where the feed water is heavily laden with foulants which might clog or damage the membrane fast, while post-treatment is required to either remove foulants that the membrane failed to remove or to add essential minerals

to drinking water which the membranes removed due to their inability to selectively remove only unwanted species. Better antifouling and cleaning techniques are expected to reduce costs associated with pre-treatment, while increased membrane selectivity is expected to help with post-treatment costs.

Chapter 3 introduces molecular dynamics (MD), the primary simulation technique used in this thesis. For simulation studies of novel nanomaterials such as BNNTs and CNTs, atomic-level details need to be considered. Molecular dynamics becomes the tool of choice, since it is faster than first principle methods like density functional theory (DFT), yet retains all the necessary atomic-level granularity needed to simulate processes that occur at the nanoscale. The pre and post-processing techniques used to create the simulation setups and then analyse the data from the MD simulations are also discussed.

Of the novel nanomaterials, BNNTs had already shown promise of providing water permeation as fast or even better than CNTs, but have only recently been brought to the fore through the resolution of manufacturing difficulties that hindered their usage. Very few experiments have therefore been carried out using BNNTs, and the MD studies on them provided contradictory results. Some showed permeability better than CNTs, while others showed the opposite. Chapter 4 resolves the discrepancy caused due to the short nanotubes used in the MD studies, and the uncertainty about the partial charges on the BN atoms. The membrane was characterised in terms of the resistance it provided to water flowing through it, allowing the total membrane resistance to be broken down to end resistance and nanotube flow resistance. Simulations of periodic, infinitely long nanotubes and very short nanotubes connected to reservoirs were run to measure the components of resistance. The end resistance of the short membranes was shown to be hiding the intrinsic high resistance within BN nanotubes, which only became evident at laboratory scale membranes. The partial charges on BN atoms were also shown to be playing a large role in determining the nanotube flow resistance. Experimental evidence favoured high partial charges as well as high resistance in BNNTs, which supported the conclusions from the study of membrane resistances. Permeability of BNNTs was therefore shown to be lower than CNTs, although their charged structure provides other advantages, as discussed in chapter 5.

The charged structure of BNNTs results in the development of a high negative zeta potential near the membrane surface when BNNTs are in contact with water. This greatly improves selectivity in BNNT membranes, as the solute charges can be effectively used to discriminate between solute species. This charge-based selectivity acts in addition to size-based selectivity, the dominant mechanism of particle selection and rejection. Using a combination of experiments, MD and CFD simulations, chapter 5 shows how BNNTs reject negatively charged silica particles. The charge-based rejection also allows the usage of BNNTs with pores larger than the particles to be rejected, allowing up to 70% higher water permeance while having the same rejection as a CNT of comparable diameter. MD studies resolve the force balance on the particle which determines whether a negatively charged particle is rejected or allowed into

the pore depending on the ratio of the particle diameter to the pore diameter. BNNTs are thus shown as a more promising desalination membrane candidate, especially with the new focus on high selectivity instead of high permeability.

Alongside high selectivity, the other avenue of significant cost reductions is in the field of membrane cleaning. The costs associated with fouled membranes and related cleaning comes close to the energy costs of the membrane, signifying the importance of focussing on this aspect of membrane operation. The most commonly used method of membrane cleaning involves stopping the filtration process and flushing the membrane with different chemicals depending on the foulant mix, followed by flushing the membrane to remove the chemicals. Chemical cleaning cannot be used on the membrane frequently, and can also degrade the membrane. Foulant deposition on the membrane surface, on the other hand, is a continuous process, ensuring lower membrane performance and reducing membrane life and permanent fouling builds up inside it. Physical cleaning methods, such as direct membrane heating or vibrations may present a way to effectively and frequently clean the membrane surface. Chapter 6 explores the question of whether direct heating of the membrane can remove nanoscale particles deposited on the membrane, and what possible mechanisms could govern such a process. Heating is shown to remove the particle from the membrane surface using a combination of bubble and film formation and increased Brownian motion of the particle itself. The large role played by Brownian forces in this process is established, which also sets the limits of the study, since quantifying effects due to Brownian motion would require a large number of realisations of longer timescales for the same simulation setup to establish probabilities of occurrence.

7.2 Future outlook

The charged nature of BNNTs, along with radius dependant ion selectivity, may be further leveraged to design membranes that deliver specific concentrations of essential minerals and salts after only a single pass through the membrane, greatly reducing remineralization (and therefore, overall) costs. This requires further research into methods of manipulating the partial charge of the BN atoms and studies into the rejection characteristics of such altered membranes. A reduction in the partial charges leads to a decrease in flow resistance, allowing for another potentially controllable parameter to optimize between flow rate and membrane rejection ability. Finally, the antifouling characteristics of such charged membranes, especially their ability to repulse organic foulants, such as negatively charged humic acids and bovine serum albumin, is a promising direction for further research. Antifouling operations through direct membrane heating also appear to hold promise but cannot be simulated for adequately long time scales using classical MD alone. Langevin solvers may be able to help overcome the short simulation times associated with MD and predict nanoparticle removal over practical timescales of seconds or minutes. The underlying assumptions of the Langevin equations, however, do not hold

for small nanoparticles with densities about the same as water (Pomeau and Résibois (1975)). As the relaxation time of the flow field around the nanoparticle approaches the relaxation time of the nanoparticle, the assumption of Brownian forces being uncorrelated in time breaks down, and memory effects must be considered (Pomeau and Résibois (1975)). Furthermore, bubble nucleation is a nanoscale probabilistic phenomenon, which might not be captured well within the framework of Langevin solvers. The presence of other substances, such as dissolved gases, salts, minerals and other particulate matter could potentially serve as bubble nucleation sites, further increasing the probability of particle removal from the surface. Where Langevin solvers might help is the simulation of removal of heavy nanoparticles at temperatures below the saturation temperature at which bubble formation might take place in the fluid. Additional methods which adequately include homogeneous and heterogeneous bubble nucleation, as well as Brownian forces in wider regimes need to be developed to provide predictability in the study of direct membrane heating based antifouling.

Thus, this thesis explores questions in the three verticals associated with desalination membranes: high permeability, high selectivity, and better membrane cleaning techniques. The questions about the permeability of BNNTs is now settled, and BNNTs are shown to have lower permeance compared to CNTs. However, the charged structure of BNNTs makes them favourable candidates for high selectivity membranes, the direction where most of the future cost reductions are expected. On the aspect of membrane cleaning, direct membrane heating is explored as a possible technique for particle removal, providing a method of continuous membrane cleaning which might be better than the current chemical cleaning of membranes. The limitations of the MD method, however, prevent a detailed exploration into the role of Brownian forces in this process, due to the probabilistic nature of the Brownian forces. Custom-built implementations of Langevin solvers, which can model bubble nucleation and account for Brownian motion at nanoscales are likely required to further explore this phenomenon.

References

Abascal, J. L. and Vega, C. "A general purpose model for the condensed phases of water: TIP4P/2005". *Journal of Chemical Physics*, 123(23):234505, 2005.

Abdul Azis, P. K., Al-Tisan, I., and Sasikumar, N. "Biofouling potential and environmental factors of seawater at a desalination plant intake". *Desalination*, 135(1-3):69–82, 2001.

Aktulga, H. M., Fogarty, J. C., Pandit, S. A., and Grama, A. Y. "Parallel reactive molecular dynamics: Numerical methods and algorithmic techniques". *Parallel Computing*, 38(4-5): 245–259, 2012.

Al-Amoudi, A. and Lovitt, R. W. "Fouling strategies and the cleaning system of NF membranes and factors affecting cleaning efficiency". *Journal of Membrane Science*, 303(1-2):4–28, 2007.

Alder, B. J. and Wainwright, T. E. "Studies in molecular dynamics. I. General method". *The Journal of Chemical Physics*, 31(2):459–466, 1959.

Andersen, H. C. "Rattle: A "velocity" version of the shake algorithm for molecular dynamics calculations". *Journal of Computational Physics*, 52(1):24–34, 1983.

Ang, W. L., Nordin, D., Mohammad, A. W., Benamor, A., and Hilal, N. "Effect of membrane performance including fouling on cost optimization in brackish water desalination process". *Chemical Engineering Research and Design*, 117:401–413, 2017.

Ang, W. S. and Elimelech, M. "Protein (BSA) fouling of reverse osmosis membranes: Implications for wastewater reclamation". *Journal of Membrane Science*, 296(1-2):83–92, 2007.

Aumeier, B. M., Yüce, S., and Wessling, M. "Temperature Enhanced Backwash". *Water Research*, 142:18–25, 2018.

Aumeier, B. M., Vollmer, F., Lenfers, S., Yüce, S., and Wessling, M. "Polymeric Membranes With Sufficient Thermo-Mechanical Stability to Deploy Temperature Enhanced Backwash". *Chemie-Ingenieur-Technik*, 93(9):1417–1422, 2021.

Avraham, N., Dosoretz, C., and Semiat, R. "Osmotic backwash process in RO membranes". *Desalination*, 199(1-3):387–389, 2006.

Azamat, J. and Khataee, A. "Removal of nitrate ion from water using boron nitride nanotubes: Insights from molecular dynamics simulations". *Computational and Theoretical Chemistry*, 1098:56–62, 2016.

Azamat, J., Khataee, A., and Joo, S. W. "Molecular dynamics simulations of trihalomethanes removal from water using boron nitride nanosheets". *Journal of Molecular Modeling*, 22(4): 1–8, 2016.

Baker, R. J., Fane, A. G., Fell, C. J., and Yoo, B. H. "Factors affecting flux in crossflow filtration". *Desalination*, 53(1-3):81–93, 1985.

Bayley, H. and Cremer, P. S. "Stochastic sensors inspired by biology". *Nature*, 413(6852): 226–230, 2001.

Berendsen, H. J., Postma, J. P., Van Gunsteren, W. F., Dinola, A., and Haak, J. R. "Molecular dynamics with coupling to an external bath". *The Journal of Chemical Physics*, 81(8):3684–3690, 1984.

Bernal, J. D. and Fowler, R. H. "A theory of water and ionic solution, with particular reference to hydrogen and hydroxyl ions". *The Journal of Chemical Physics*, 1(8):515–548, 1933.

Bethune, D. S., Klang, C. H., De Vries, M. S., Gorman, G., Savoy, R., Vazquez, J., and Beyers, R. "Cobalt-catalysed growth of carbon nanotubes with single-atomic-layer walls". *Nature*, 363(6430):605–607, 1993.

Bilad, M. R., Discart, V., Vandamme, D., Foubert, I., Muylaert, K., and Vankelecom, I. F. "Harvesting microalgal biomass using a magnetically induced membrane vibration (MMV) system: Filtration performance and energy consumption". *Bioresource Technology*, 138: 329–338, 2013.

Bitzek, E., Koskinen, P., Gähler, F., Moseler, M., and Gumbsch, P. "Structural relaxation made simple". *Phys. Rev. Lett.*, 97:170201, 2006.

Blanpain-Avet, P., Migdal, J. F., and Benezech, T. "Chemical cleaning of a tubular ceramic microfiltration membrane fouled with a whey protein concentrate suspension-Characterization of hydraulic and chemical cleanliness". *Journal of Membrane Science*, 337(1-2):153–174, 2009.

Bocquet, L. and Charlaix, E. "Nanofluidics, from bulk to interfaces". *Chemical Society Reviews*, 39(3):1073–1095, 2010.

Borg, M. K., Lockerby, D. A., Ritos, K., and Reese, J. M. "Multiscale simulation of water flow through laboratory-scale nanotube membranes". *Journal of Membrane Science*, 567: 115–126, 2018.

Bowen, W. R. and Sharif, A. O. "Prediction of optimum membrane design: Pore entrance shape and surface potential". *Colloids and Surfaces A: Physicochemical and Engineering Aspects*, 201(1-3):207–217, 2002.

Burn, S., Hoang, M., Zarzo, D., Olewniak, F., Campos, E., Bolto, B., and Barron, O. "Desalination techniques - A review of the opportunities for desalination in agriculture". *Desalination*, 364:2–16, 2015.

Casanova, S., Liu, T. Y., Chew, Y. M. J., Livingston, A., and Mattia, D. "High flux thin-film nanocomposites with embedded boron nitride nanotubes for nanofiltration". *Journal of Membrane Science*, 597, 2020a.

Casanova, S., Mistry, S., Mazinani, S., Borg, M. K., Chew, Y. M., and Mattia, D. "Enhanced nanoparticle rejection in aligned boron nitride nanotube membranes". *Nanoscale*, 12(41): 21138–21145, 2020b.

Chai, X., Kobayashi, T., and Fujii, N. "Ultrasound effect on cross-flow filtration of polyacrylonitrile ultrafiltration membranes". *Journal of Membrane Science*, 148(1):129–135, 1998.

Chan, W. F., Marand, E., and Martin, S. M. "Novel zwitterion functionalized carbon nanotube nanocomposite membranes for improved RO performance and surface anti-biofouling resistance". *Journal of Membrane Science*, 509:125–137, 2016.

Chen, D., Weavers, L. K., and Walker, H. W. "Ultrasonic control of ceramic membrane fouling by particles: Effect of ultrasonic factors". *Ultrasonics Sonochemistry*, 13(5):379–387, 2006.

Chen, X., Wu, P., Rousseas, M., Okawa, D., Gartner, Z., Zettl, A., and Bertozzi, C. R. "Boron nitride nanotubes are noncytotoxic and can be functionalized for interaction with proteins and cells". *Journal of the American Chemical Society*, 131(3):890–891, 2009.

Cheng, W., Liu, C., Tong, T., Epsztein, R., Sun, M., Verduzco, R., Ma, J., and Elimelech, M. "Selective removal of divalent cations by polyelectrolyte multilayer nanofiltration membrane: Role of polyelectrolyte charge, ion size, and ionic strength". *Journal of Membrane Science*, 559:98–106, 2018.

Cheryan, M. *Ultrafiltration and Microfiltration Handbook*. CRC Press, 1998.

Chogani, A., Moosavi, A., Bagheri Sarvestani, A., and Shariat, M. "The effect of chemical functional groups and salt concentration on performance of single-layer graphene membrane in water desalination process: A molecular dynamics simulation study". *Journal of Molecular Liquids*, 301:112478, 2020.

Chong, T. H., Wong, F. S., and Fane, A. G. "Implications of critical flux and cake enhanced osmotic pressure (CEOP) on colloidal fouling in reverse osmosis: Experimental observations". *Journal of Membrane Science*, 314(1-2):101–111, 2008.

Chopra, N. G., Luyken, R. J., Cherrey, K., Crespi, V. H., Cohen, M. L., Louie, S. G., and Zettl, A. "Boron nitride nanotubes". *Science*, 269(5226):966–967, 1995.

Cohen-Tanugi, D., McGovern, R. K., Dave, S. H., Lienhard, J. H., and Grossman, J. C. "Quantifying the potential of ultra-permeable membranes for water desalination". *Energy and Environmental Science*, 7(3):1134–1141, 2014.

Corry, B. "Water and ion transport through functionalised carbon nanotubes: Implications for desalination technology". *Energy Environ. Sci.*, 4:751–759, 2011.

Corry, B. "Designing carbon nanotube membranes for efficient water desalination". *Journal of Physical Chemistry B*, 112(5):1427–1434, 2008.

Creber, S. A., Vrouwenvelder, J. S., van Loosdrecht, M. C., and Johns, M. L. "Chemical cleaning of biofouling in reverse osmosis membranes evaluated using magnetic resonance imaging". *Journal of Membrane Science*, 362(1-2):202–210, 2010.

Crimp, M. J., Oppermann, D. A., and Krehbiel, K. "Suspension properties of hexagonal BN powders: Effect of pH and oxygen content". *Journal of Materials Science*, 34(11):2621–2625, 1999.

Dana, A., Hadas, S., and Ramon, G. Z. "Potential application of osmotic backwashing to brackish water desalination membranes". *Desalination*, 468:114029, 2019.

Darre, N. C. and Toor, G. S. "Desalination of Water: a Review". *Current Pollution Reports*, 4 (2):104–111, 2018.

Daw, M. S., Foiles, S. M., and Baskes, M. I. "The embedded-atom method: a review of theory and applications". *Materials Science Reports*, 9(7-8):251–310, 1993.

De Grooth, J., Reurink, D. M., Ploegmakers, J., De Vos, W. M., and Nijmeijer, K. "Charged micropollutant removal with hollow fiber nanofiltration membranes based on polycation/polyzwitterion/polyanion multilayers". *ACS Applied Materials and Interfaces*, 6(19): 17009–17017, 2014.

Dersoir, B., Schofield, A. B., Robert de Saint Vincent, M., and Tabuteau, H. "Dynamics of pore fouling by colloidal particles at the particle level". *Journal of Membrane Science*, 573: 411–424, 2019.

Donnan, F. G. "Theorie der membrangleichgewichte und membranpotentiale bei vorhandensein von nicht dialysierenden elektrolyten. ein beitrag zur physikalisch-chemischen physiologie.". *Zeitschrift für Elektrochemie und angewandte physikalische Chemie*, 17(14): 572–581, 1911.

D'Souza, N. M. and Mawson, A. J. "Membrane cleaning in the dairy industry: A review". *Critical Reviews in Food Science and Nutrition*, 45(2):125–134, 2005.

Dujardin, E., Ebbesen, T. W., Hiura, H., and Tanigaki, K. "Capillarity and wetting of carbon nanotubes". *Science*, 265(5180):1850–1852, 1994.

Ebbesen, T. W. "Wetting, filling and decorating carbon nanotubes". *Journal of Physics and Chemistry of Solids*, 57(6-8):951–955, 1996.

Ebrahim, S. "Cleaning and regeneration of membranes in desalination and wastewater applications: State-of-the-art". *Desalination*, 96(1-3):225–238, 1994.

Elimelech, M. and Phillip, W. A. "The future of seawater desalination: Energy, technology, and the environment". *Science*, 333(6043):712–717, 2011.

Epsztein, R., DuChanois, R. M., Ritt, C. L., Noy, A., and Elimelech, M. "Towards single-species selectivity of membranes with subnanometre pores". *Nature Nanotechnology*, 15 (6):426–436, 2020.

Eyring, H. "Viscosity, plasticity, and diffusion as examples of absolute reaction rates". *The Journal of Chemical Physics*, 4(4):283–291, 1936.

Fabris, R., Lee, E. K., Chow, C. W., Chen, V., and Drikas, M. "Pre-treatments to reduce fouling of low pressure micro-filtration (MF) membranes". *Journal of Membrane Science*, 289(1-2): 231–240, 2007.

Fairbanks, H. and Chen, W. "Ultrasonic Acceleration of Liquid Flow Through Porous Media". In *AICHE Syposium Series 63rd National Meeting*, 1970.

Falk, K., Sedlmeier, F., Joly, L., Netz, R. R., and Bocquet, L. "Molecular origin of fast water transport in carbon nanotube membranes: Superlubricity versus curvature dependent friction". *Nano Letters*, 10(10):4067–4073, 2010.

Flemming, H. C. "Microbial deterioration of materials - fundamentals economical and technical overview". *Werkstoffe und Korrosion*, 45(1):5–9, 1994.

Flemming, H.-C. *Microbial Biofouling: Unsolved Problems, Insufficient Approaches, and Possible Solutions*, pages 81–109. Springer Berlin Heidelberg, 2011.

Freeman, B. D. "Basis of permeability/selectivity tradeoff relations in polymeric gas separation membranes". *Macromolecules*, 32(2):375–380, 1999.

Frenkel, D. and Smit, B. *Understanding molecular simulation: From algorithms to applications*. Academic Press, San Diego, second edition, 2002.

Gao, W., Liang, H., Ma, J., Han, M., lin Chen, Z., shuang Han, Z., and bai Li, G. "Membrane fouling control in ultrafiltration technology for drinking water production: A review". *Desalination*, 272(1-3):1–8, 2011.

Gibbs, H. and Smith, A. "On the equilibrium of heterogeneous substances". *Transactions of the Connecticut Academy of Arts and Sciences*, 3:108–248, 1878.

Gilbert, P., McBain, A., and Rickard, A. "Formation of microbial biofilm in hygienic situations: a problem of control". *International Biodeterioration and Biodegradation*, 51(4):245–248, 2003.

Goh, P. S. and Ismail, A. F. "A review on inorganic membranes for desalination and wastewater treatment". *Desalination*, 434:60–80, 2018.

Gohil, J. M. and Suresh, A. K. "Chlorine attack on reverse osmosis membranes: Mechanisms and mitigation strategies". *Journal of Membrane Science*, 541:108–126, 2017.

Govind Rajan, A., Strano, M. S., and Blankschtein, D. "Liquids with Lower Wettability Can Exhibit Higher Friction on Hexagonal Boron Nitride: The Intriguing Role of Solid-Liquid Electrostatic Interactions". *Nano Letters*, 19(3):1539–1551, 2019.

Guo, T., Englehardt, J., and Wu, T. "Review of cost versus scale: Water and wastewater treatment and reuse processes". *Water Science and Technology*, 69(2):223–234, 2014.

Guo, W., Ngo, H. H., and Li, J. "A mini-review on membrane fouling". *Bioresource Technology*, 122:27–34, 2012.

Gupta, K. M., Zhang, K., and Jiang, J. "Water Desalination through Zeolitic Imidazolate Framework Membranes: Significant Role of Functional Groups". *Langmuir*, 31(48):13230–13237, 2015.

Hamilton, E. J., Dolan, S. E., Mann, C. M., Colijn, H. O., McDonald, C. A., and Shore, S. G. "Preparation of amorphous boron nitride and its conversion to a turbostratic, tubular form". *Science*, 260(5108):659–661, 1993.

Han, S. S., Kang, J. K., Lee, H. M., Van Duin, A. C., and Goddard, W. A. "Theoretical study on interaction of hydrogen with single-walled boron nitride nanotubes. ii. collision, storage, and adsorption". *The Journal of Chemical Physics*, 123(11):114704, 2005.

Hibbs, M. R., McGrath, L. K., Kang, S., Adout, A., Altman, S. J., Elimelech, M., and Cornelius, C. J. "Designing a biocidal reverse osmosis membrane coating: Synthesis and biofouling properties". *Desalination*, 380:52–59, 2016.

Hilder, T. A., Yang, R., Ganesh, V., Gordon, D., Bliznyuk, A., Rendell, A. P., and Chung, S. H. "Validity of current force fields for simulations on boron nitride nanotubes". *Micro and Nano Letters*, 5(2):150–156, 2010.

Hilder, T. A., Gordon, D., and Chung, S. H. "Salt rejection and water transport through boron nitride nanotubes". *Small*, 5(19):2183–2190, 2009a.

Hilder, T. A., Gordon, D., and Chung, S. H. "Boron nitride nanotubes selectively permeable to cations or anions". *Small*, 5(24):2870–2875, 2009b.

Hinds, B. J., Chopra, N., Rantell, T., Andrews, R., Gavalas, V., and Bachas, L. G. "Aligned Multiwalled Carbon Nanotube Membranes". *Science*, 303(5654):62–65, 2004.

Hockney, R. W. and Eastwood, J. W. *Computer Simulation Using Particles*. A. Hilger, 1988.

Hoek, E. M. and Elimelech, M. "Cake-Enhanced Concentration Polarization: A New Fouling Mechanism for Salt-Rejecting Membranes". *Environmental Science and Technology*, 37 (24):5581–5588, 2003.

Holt, J. K., Park, H. G., Wang, Y., Stadermann, M., Artyukhin, A. B., Grigoropoulos, C. P., Noy, A., and Bakajin, O. "Fast mass transport through sub-2-nanometer carbon nanotubes". *Science*, 312(5776):1034–1037, 2006.

Hong, S. and Elimelech, M. "Chemical and physical aspects of natural organic matter (NOM) fouling of nanofiltration membranes". *Journal of Membrane Science*, 132(2):159–181, 1997.

Hoslett, J., Massara, T. M., Malamis, S., Ahmad, D., van den Boogaert, I., Katsou, E., Ahmad, B., Ghazal, H., Simons, S., Wrobel, L., and Jouhara, H. "Surface water filtration using granular media and membranes: A review". *Science of the Total Environment*, 639:1268–1282, 2018.

Howell, J., Sanchez, V., and Field, R. *Membranes in Bioprocessing: Theory and Applications*. Springer Science and Business Media LLC, 1993.

Hu, H., Bao, L., Priezjev, N. V., and Luo, K. "Identifying two regimes of slip of simple fluids over smooth surfaces with weak and strong wall-fluid interaction energies". *Journal of Chemical Physics*, 146(3):034701, 2017.

Hummer, G., Rasaiah, J. C., and Noworyta, J. P. "Water conduction through the hydrophobic channel of a carbon nanotube". *Nature*, 414(6860):188–190, 2001.

Iijima, S. "Helical microtubules of graphitic carbon". *Nature*, 354(6348):56–58, 1991.

Iijima, S. and Ichihashi, T. "Single-shell carbon nanotubes of 1-nm diameter". *Nature*, 363 (6430):603–605, 1993.

Jiang, S., Li, Y., and Ladewig, B. P. "A review of reverse osmosis membrane fouling and control strategies". *Science of the Total Environment*, 595:567–583, 2017.

Joni, I. M., Balgis, R., Ogi, T., Iwaki, T., and Okuyama, K. "Surface functionalization for dispersing and stabilizing hexagonal boron nitride nanoparticle by bead milling". *Colloids and Surfaces A: Physicochemical and Engineering Aspects*, 388(1-3):49–58, 2011.

Jorgensen, W. L., Chandrasekhar, J., Madura, J. D., Impey, R. W., and Klein, M. L. "Comparison of simple potential functions for simulating liquid water". *The Journal of Chemical Physics*, 79(2):926–935, 1983.

Ju, S. P., Wang, Y. C., and Lien, T. W. "Tuning the electronic properties of boron nitride nanotube by mechanical uni-axial deformation: A DFT study". *Nanoscale Research Letters*, 6(1):1–11, 2011.

Kalogirou, S. A. "Seawater desalination using renewable energy sources". *Progress in Energy and Combustion Science*, 31(3):242–281, 2005.

Kalra, A., Garde, S., and Hummer, G. "Osmotic water transport through carbon nanotube membranes". *Proceedings of the National Academy of Sciences of the United States of America*, 100(18):10175–10180, 2003.

Kang, G. D., Gao, C. J., Chen, W. D., Jie, X. M., Cao, Y. M., and Yuan, Q. "Study on hypochlorite degradation of aromatic polyamide reverse osmosis membrane". *Journal of Membrane Science*, 300(1-2):165–171, 2007.

Kannam, S. K., Todd, B. D., Hansen, J. S., and Daivis, P. J. "How fast does water flow in carbon nanotubes?". *Journal of Chemical Physics*, 138(9):094701, 2013.

Karagiannis, I. C. and Soldatos, P. G. "Water desalination cost literature: review and assessment". *Desalination*, 223(1-3):448–456, 2008.

Kennedy, M. D., Muñoz Tobar, F. P., Amy, G., and Schippers, J. C. "Transparent exopolymer particle (TEP) fouling of ultrafiltration membrane systems". *Desalination and Water Treatment*, 6(1-3):169–176, 2009.

Kim, K. S., Kim, M. J., Park, C., Fay, C. C., Chu, S.-H., Kingston, C. T., and Simard, B. "Scalable manufacturing of boron nitride nanotubes and their assemblies: a review". *Semiconductor Science and Technology*, 32(1):013003, 2016.

Kobayashi, T., Chai, X., and Fujii, N. "Ultrasound enhanced cross-flow membrane filtration". *Separation and Purification Technology*, 17(1):31–40, 1999.

Kokugan, T., Kaseno, Fujiwara, S., and Shimizu, M. "Ultrasonic Effect on Ultrafiltration Properties of Ceramic Membrane.". *Membrane*, 20(3):213–223, 1995.

Kroner, K. H., Nissinen, V., and Ziegler, H. "Improved dynamic filtration of microbial suspensions". *Bio/Technology*, 5(9):921–926, 1987.

Lee, B., Baek, Y., Lee, M., Jeong, D. H., Lee, H. H., Yoon, J., and Kim, Y. H. "A carbon nanotube wall membrane for water treatment". *Nature Communications*, 6:7109, 2015.

Lee, E. K., Chen, V., and Fane, A. G. "Natural organic matter (NOM) fouling in low pressure membrane filtration - effect of membranes and operation modes". *Desalination*, 218(1-3): 257–270, 2008.

Lee, K. P., Arnot, T. C., and Mattia, D. "A review of reverse osmosis membrane materials for desalination-Development to date and future potential". *Journal of Membrane Science*, 370 (1-2):1–22, 2011.

Lee, S. and Elimelech, M. "Relating organic fouling of reverse osmosis membranes to intermolecular adhesion forces". *Environmental Science and Technology*, 40(3):980–987, 2006.

Lei, W., Mochalin, V. N., Liu, D., Qin, S., Gogotsi, Y., and Chen, Y. "Boron nitride colloidal solutions, ultralight aerogels and freestanding membranes through one-step exfoliation and functionalization". *Nature Communications*, 6:8849, 2015.

Lemmon, E., McLinden, M., and Friend, D. "Thermophysical Properties of Fluid Systems". In Linstrom, P. and Mallard, W., editors, *NIST Chemistry WebBook, NIST Standard Reference Database*, number 69. National Institute of Standards and Technology, Gaithersburg MD, 20899, 2017.

Li, J., Sanderson, R. D., and Jacobs, E. P. "Ultrasonic cleaning of nylon microfiltration membranes fouled by Kraft paper mill effluent". *Journal of Membrane Science*, 205(1-2): 247–257, 2002.

Liang, L., Li, J. C., Zhang, L., Zhang, Z., Shen, J. W., Li, L., and Wu, J. "Computer simulation of water desalination through boron nitride nanotubes". *Physical Chemistry Chemical Physics*, 19(44):30031–30038, 2017.

Lim, A. L. and Bai, R. "Membrane fouling and cleaning in microfiltration of activated sludge wastewater". *Journal of Membrane Science*, 216(1-2):279–290, 2003.

Loeb, S. "Loeb-Sourirajan Membrane: How It Came About.". In *ACS Symposium Series*, pages 1–9, 1981.

Lohaus, T., Beck, J., Harhues, T., de Wit, P., Benes, N. E., and Wessling, M. "Direct membrane heating for temperature induced fouling prevention". *Journal of Membrane Science*, 612: 118431, 2020.

Low, Z. X., Ji, J., Blumenstock, D., Chew, Y. M., Wolverson, D., and Mattia, D. "Fouling resistant 2D boron nitride nanosheet – PES nanofiltration membranes". *Journal of Membrane Science*, 563:949–956, 2018.

Lyster, E., man Kim, M., Au, J., and Cohen, Y. "A method for evaluating antiscalant retardation of crystal nucleation and growth on RO membranes". *Journal of Membrane Science*, 364 (1):122–131, 2010.

Majumder, M. and Corry, B. "Anomalous decline of water transport in covalently modified carbon nanotube membranes". *Chemical Communications*, 47:7683–7685, 2011.

Majumder, M., Chopra, N., Andrews, R., and Hinds, B. J. "Enhanced flow in carbon nanotubes". *Nature*, 438(7064):44–44, 2005.

Manchanda, H. and Kumar, M. "A comprehensive decade review and analysis on designs and performance parameters of passive solar still". *Renewables: Wind, Water, and Solar*, 2(17), 2015.

Mao, Z. and Sinnott, S. B. "Separation of organic molecular mixtures in carbon nanotubes and bundles: Molecular dynamics simulations". *Journal of Physical Chemistry B*, 105(29): 6916–6924, 2001.

Marchetti, P., Jimenez Solomon, M. F., Szekely, G., and Livingston, A. G. "Molecular separation with organic solvent nanofiltration: A critical review". *Chemical Reviews*, 114 (21):10735–10806, 2014.

Masselin, I., Chasseray, X., Durand-Bourlier, L., Lainé, J. M., Syzaret, P. Y., and Lemordant, D. "Effect of sonication on polymeric membranes". *Journal of Membrane Science*, 181(2): 213–220, 2001.

Matsumoto, K., Katsuyama, S., and Ohya, H. "Separation of yeast by cross-flow filtration with backwashing". *Journal of Fermentation Technology*, 65(1):77–83, 1987.

Matsumoto, K., Kawahara, M., and Ohya, H. "Cross-flow filtration of yeast by microporous ceramic membrane with backwashing". *Journal of Fermentation Technology*, 66(2):199–205, 1988.

Matsumoto, Y., Miwa, T., Nakao, S. I., and Kimura, S. "Improvement of membrane permeation performance by ultrasonic microfiltration". *Journal of Chemical Engineering of Japan*, 29 (4):561–567, 1996.

Mattia, D. and Gogotsi, Y. "Review: Static and dynamic behavior of liquids inside carbon nanotubes". *Microfluidics and Nanofluidics*, 5:289–305, 2008.

Mattia, D., Leese, H., and Lee, K. P. "Carbon nanotube membranes: From flow enhancement to permeability". *Journal of Membrane Science*, 475:266–272, 2015.

Mehta, A. and Zydney, A. L. "Permeability and selectivity analysis for ultrafiltration membranes". *Journal of Membrane Science*, 249(1-2):245–249, 2005.

Mistry, S., Pillai, R., Mattia, D., and Borg, M. K. "Untangling the physics of water transport in boron nitride nanotubes". *Nanoscale*, 13(43):18096–18102, 2021.

Miyoshi, T., Tsuyuhara, T., Ogyu, R., Kimura, K., and Watanabe, Y. "Seasonal variation in membrane fouling in membrane bioreactors (MBRs) treating municipal wastewater". *Water Research*, 43(20):5109–5118, 2009.

Moritz, T., Benfer, S., Árki, P., and Tomandl, G. "Influence of the surface charge on the permeate flux in the dead-end filtration with ceramic membranes". *Separation and Purification Technology*, 25(1-3):501–508, 2001.

Mulder, M. H. "Polarization phenomena and membrane fouling". *Membrane Science and Technology*, 2(C):45–84, 1995.

Nguyen, H., Ohannesian, N., Bandara, P. C., Ansari, A., Deleo, C. T., Rodrigues, D., Martirosyan, K. S., and Shih, W. C. "Magnetic Active Water Filter Membrane for Induced Heating to Remove Biofoulants". *ACS Applied Materials and Interfaces*, 12(9):10291–10298, 2020.

Ni, L., Meng, J., Li, X., and Zhang, Y. "Surface coating on the polyamide TFC RO membrane for chlorine resistance and antifouling performance improvement". *Journal of Membrane Science*, 451:205–215, 2014.

Nicholls, W. D., Borg, M. K., Lockerby, D. A., and Reese, J. M. "Water transport through carbon nanotubes with defects". *Molecular Simulation*, 38(10):781–785, 2012.

Nipkow, A., Zeikus, J. G., and Gerhardt, P. "Microfiltration cell-recycle pilot system for continuous thermoanaerobic production of exo-β-amylase". *Biotechnology and Bioengineering*, 34(8):1075–1084, 1989.

Nosé, S. "A unified formulation of the constant temperature molecular dynamics methods". *The Journal of Chemical Physics*, 81(1):511–519, 1984.

Ochando-Pulido, J. M., Victor-Ortega, M. D., and Martínez-Ferez, A. "On the cleaning procedure of a hydrophilic reverse osmosis membrane fouled by secondary-treated olive mill wastewater". *Chemical Engineering Journal*, 260:142–151, 2015.

Park, H. B., Kamcev, J., Robeson, L. M., Elimelech, M., and Freeman, B. D. "Maximizing the right stuff: The trade-off between membrane permeability and selectivity". *Science*, 356 (6343):1138–1148, 2017.

Peeters, J. M., Mulder, M. H., and Strathmann, H. "Streaming potential measurements as a characterization method for nanofiltration membranes". *Colloids and Surfaces A: Physicochemical and Engineering Aspects*, 150(1-3):247–259, 1999.

Peng, H. and Tremblay, A. Y. "Membrane regeneration and filtration modeling in treating oily wastewaters". *Journal of Membrane Science*, 324(1-2):59–66, 2008.

Pollock, E. L. and Glosli, J. "Comments on P3M, FMM, and the Ewald method for large periodic Coulombic systems". *Computer Physics Communications*, 95(2-3):93–110, 1996.

Pomeau, Y. and Résibois, P. "Time dependent correlation functions and mode-mode coupling theories". *Physics Reports*, 19(2):63–139, 1975.

Qin, J.-J., Liberman, B., A. Kekre, K., and Gossan, A. "Direct Osmosis for Reverse Osmosis Fouling Control: Principles, Applications and Recent Developments". *The Open Chemical Engineering Journal*, 3(1):8–16, 2009.

Qin, X., Yuan, Q., Zhao, Y., Xie, S., and Liu, Z. "Measurement of the rate of water translocation through carbon nanotubes". *Nano Letters*, 11(5):2173–2177, 2011.

Rana, D., Narbaitz, R. M., Garand-Sheridan, A. M., Westgate, A., Matsuura, T., Tabe, S., and Jasim, S. Y. "Development of novel charged surface modifying macromolecule blended PES membranes to remove EDCs and PPCPs from drinking water sources". *Journal of Materials Chemistry A*, 2(26):10059–10072, 2014.

Rappé, A. K. and Goddard, W. A. "Charge equilibration for molecular dynamics simulations". *Journal of Physical Chemistry*, 95(8):3358–3363, 1991.

Rezakazemi, M., Dashti, A., Riasat Harami, H., Hajilari, N., and Inamuddin. "Fouling-resistant membranes for water reuse". *Environmental Chemistry Letters*, 16(3):715–763, 2018.

Richard Bowen, W., Filippov, A. N., Sharif, A. O., and Starov, V. M. "Model of the interaction between a charged particle and a pore in a charged membrane surface". *Advances in Colloid and Interface Science*, 81(1):35–72, 1999.

Riesmeier, B., Kroner, K. H., and Kula, M. R. "Tangential filtration of microbial suspensions: filtration resistances and model development". *Journal of Biotechnology*, 12(2):153–171, 1989.

Ritos, K., Mattia, D., Calabrò, F., and Reese, J. M. "Flow enhancement in nanotubes of different materials and lengths". *Journal of Chemical Physics*, 140(1):014702, 2014.

Ritos, K., Borg, M. K., Lockerby, D. A., Emerson, D. R., and Reese, J. M. "Hybrid molecular-continuum simulations of water flow through carbon nanotube membranes of realistic thickness". *Microfluidics and Nanofluidics*, 19(5):997–1010, 2015.

Ritos, K., Borg, M. K., Mottram, N. J., and Reese, J. M. "Electric fields can control the transport of water in carbon nanotubes". *Philosophical Transactions of the Royal Society A: Mathematical, Physical and Engineering Sciences*, 374(2060):20150025, 2016.

Robeson, L. M. "Correlation of separation factor versus permeability for polymeric membranes". *Journal of Membrane Science*, 62(2):165–185, 1991.

Roy, S., Bhadra, M., and Mitra, S. "Enhanced desalination via functionalized carbon nanotube immobilized membrane in direct contact membrane distillation". *Separation and Purification Technology*, 136:58–65, 2014.

Rubio, A., Corkill, J. L., and Cohen, M. L. "Theory of graphitic boron nitride nanotubes". *Physical Review B*, 49(7):5081–5084, 1994.

Ruckenstein, E. and Rajora, P. "On the no-slip boundary condition of hydrodynamics". *Journal of Colloid And Interface Science*, 96(2):488–491, 1983.

Ryckaert, J. P., Ciccotti, G., and Berendsen, H. J. "Numerical integration of the cartesian equations of motion of a system with constraints: molecular dynamics of n-alkanes". *Journal of Computational Physics*, 23(3):327–341, 1977.

Saad, M. A. "Early discovery of RO membrane fouling and real-time monitoring of plant performance for optimizing cost of water". *Desalination*, 165(SUPPL.):183–191, 2004.

Sagiv, A. and Semiat, R. "Parameters affecting backwash variables of RO membranes". *Desalination*, 261(3):347–353, 2010.

Sam, A., Hartkamp, R., Kannam, S. K., and Sathian, S. P. "Prediction of fluid slip in cylindrical nanopores using equilibrium molecular simulations". *Nanotechnology*, 29(48):485404, 2018.

Sarkar, S., Sengupta, A. K., and Prakash, P. "The Donnan membrane principle: Opportunities for sustainable engineered processes and materials". *Environmental Science and Technology*, 44(4):1161–1166, 2010.

Saxena, A., Tripathi, B. P., Kumar, M., and Shahi, V. K. "Membrane-based techniques for the separation and purification of proteins: An overview". *Advances in Colloid and Interface Science*, 145(1-2):1–22, 2009.

Secchi, E., Marbach, S., Niguès, A., Stein, D., Siria, A., and Bocquet, L. "Massive radius-dependent flow slippage in carbon nanotubes". *Nature*, 537(7619):210–213, 2016.

Seidel, A., Waypa, J. J., and Elimelech, M. "Role of charge (Donnan) exclusion in removal of arsenic from water by a negatively charged porous nanofiltration membrane". *Environmental Engineering Science*, 18(2):105–113, 2001.

Shenvi, S. S., Isloor, A. M., and Ismail, A. F. "A review on RO membrane technology: Developments and challenges". *Desalination*, 368:10–26, 2015.

Shinoda, W., Shiga, M., and Mikami, M. "Rapid estimation of elastic constants by molecular dynamics simulation under constant stress". *Physical Review B - Condensed Matter and Materials Physics*, 69(13):134103, 2004.

Shirazi, S., Lin, C. J., and Chen, D. "Inorganic fouling of pressure-driven membrane processes - A critical review". *Desalination*, 250(1):236–248, 2010.

Shu, J. J., Teo, J. B. M., and Chan, W. K. "A new model for fluid velocity slip on a solid surface". *Soft Matter*, 12(40):8388–8397, 2016.

Siria, A., Poncharal, P., Biance, A. L., Fulcrand, R., Blase, X., Purcell, S. T., and Bocquet, L. "Giant osmotic energy conversion measured in a single transmembrane boron nitride nanotube". *Nature*, 494(7438):455–458, 2013.

Skoulidas, A. I., Ackerman, D. M., Johnson, J. K., and Sholl, D. S. "Rapid Transport of Gases in Carbon Nanotubes". *Physical Review Letters*, 89(18):185901, 2002.

Sokhan, V. P., Nicholson, D., and Quirke, N. "Fluid flow in nanopores: An examination of hydrodynamic boundary conditions". *Journal of Chemical Physics*, 115(8):3878–3887, 2001.

Sokhan, V. P., Nicholson, D., and Quirke, N. "Fluid flow in nanopores: Accurate boundary conditions for carbon nanotubes". *Journal of Chemical Physics*, 117(18):8531–8539, 2002.

Srivastava, A., Srivastava, O. N., Talapatra, S., Vajtai, R., and Ajayan, P. M. "Carbon nanotube filters". *Nature Materials*, 3(9):610–614, 2004.

Su, J. and Guo, H. "Control of unidirectional transport of single-file water molecules through carbon nanotubes in an electric field". *ACS Nano*, 5(1):351–359, 2011.

Subramani, A. and Jacangelo, J. G. "Emerging desalination technologies for water treatment: A critical review". *Water Research*, 75:164–187, 2015.

Subramani, A., Badruzzaman, M., Oppenheimer, J., and Jacangelo, J. G. "Energy minimization strategies and renewable energy utilization for desalination: A review". *Water Research*, 45 (5):1907–1920, 2011.

Suk, M. E., Raghunathan, A. V., and Aluru, N. R. "Fast reverse osmosis using boron nitride and carbon nanotubes". *Applied Physics Letters*, 92(13):133120, 2008.

Suk, M. E. and Aluru, N. R. "Suk and Aluru reply". *Physical Review Letters*, 105(20):435, 2010.

Tarleton, E. S. and Wakeman, R. J. "Electro-acoustic crossflow microfiltration". *Filtration and Separation*, 29(5):425–432, 1992.

Teow, Y. H. and Mohammad, A. W. "New generation nanomaterials for water desalination: A review". *Desalination*, 451:2–17, 2019.

Thomas, J. A. and McGaughey, A. J. "Reassessing fast water transport through carbon nanotubes". *Nano Letters*, 8(9):2788–2793, 2008.

Thomas, J. A. and McGaughey, A. J. "Water flow in carbon nanotubes: Transition to subcontinuum transport". *Physical Review Letters*, 102(18):184502, 2009.

Thomas, M. and Corry, B. "A computational assessment of the permeability and salt rejection of carbon nanotube membranes and their application to water desalination". *Philosophical Transactions of the Royal Society A: Mathematical, Physical and Engineering Sciences*, 374: 20150020, 2016.

Thurman, E. M. and Malcolm, R. L. "Humic Substances in Groundwater.". *National Meeting - American Chemical Society, Division of Environmental Chemistry*, 23(2):242–244, 1983.

Tocci, G., Joly, L., and Michaelides, A. "Friction of water on graphene and hexagonal boron nitride from Ab initio methods: Very different slippage despite very similar interface structures". *Nano Letters*, 14(12):6872–6877, 2014.

Tran, T. T. V., Kumar, S. R., and Lue, S. J. "Separation mechanisms of binary dye mixtures using a PVDF ultrafiltration membrane: Donnan effect and intermolecular interaction". *Journal of Membrane Science*, 575:38–49, 2019.

Van Duin, A. C., Dasgupta, S., Lorant, F., and Goddard, W. A. "ReaxFF: A reactive force field for hydrocarbons". *Journal of Physical Chemistry A*, 105(41):9396–9409, 2001.

Van Reis, R. D. "WO2001008792A2 - Charged filtration membranes and uses therefor - Google Patents", 2001.

Vatanpour, V., Safarpour, M., Khataee, A., Zarrabi, H., Yekavalangi, M. E., and Kavian, M. "A thin film nanocomposite reverse osmosis membrane containing amine-functionalized carbon nanotubes". *Separation and Purification Technology*, 184:135–143, 2017.

Vázquez-Quesada, A. and Ellero, M. "Analytical solution for the lubrication force between two spheres in a bi-viscous fluid". *Physics of Fluids*, 28(7):073101, 2016.

Verlet, L. "Computer "experiments" on classical fluids. I. Thermodynamical properties of Lennard-Jones molecules". *Physical Review*, 159(1):98–103, 1967.

Walther, J. H., Ritos, K., Cruz-Chu, E. R., Megaridis, C. M., and Koumoutsakos, P. "Barriers to superfast water transport in carbon nanotube membranes". *Nano Letters*, 13(5):1910–1914, 2013.

Wang, F. C. and Zhao, Y. P. "Slip boundary conditions based on molecular kinetic theory: The critical shear stress and the energy dissipation at the liquid-solid interface". *Soft Matter*, 7 (18):8628–8634, 2011.

Wang, G. J. and Hadjiconstantinou, N. G. "Universal molecular-kinetic scaling relation for slip of a simple fluid at a solid boundary". *Physical Review Fluids*, 4:064201, 2019.

Wang, Z., Ma, J., Tang, C. Y., Kimura, K., Wang, Q., and Han, X. "Membrane cleaning in membrane bioreactors: A review". *Journal of Membrane Science*, 468:276–307, 2014.

Wei, X. and Luo, T. "Effects of Electrostatic Interaction and Chirality on the Friction Coefficient of Water Flow Inside Single-Walled Carbon Nanotubes and Boron Nitride Nanotubes". *Journal of Physical Chemistry C*, 122(9):5131–5140, 2018.

Weissberg, H. L. "End correction for slow viscous flow through long tubes". *Physics of Fluids*, 5(9):1033–1036, 1962.

Werber, J. R., Deshmukh, A., and Elimelech, M. "The Critical Need for Increased Selectivity, Not Increased Water Permeability, for Desalination Membranes". *Environmental Science and Technology Letters*, 3(4):112–120, 2016a.

Werber, J. R., Osuji, C. O., and Elimelech, M. "Materials for next-generation desalination and water purification membranes". *Nature Reviews Materials*, 1:16018, 2016b.

Won, C. Y. and Aluru, N. R. "Water permeation through a subnanometer boron nitride nanotube". *Journal of the American Chemical Society*, 129(10):2748–2749, 2007.

Won, C. Y. and Aluru, N. R. "Structure and dynamics of water confined in a boron nitride nanotube". *Journal of Physical Chemistry C*, 112(6):1812–1818, 2008.

Won, C. Y., Joseph, S., and Aluru, N. R. "Effect of quantum partial charges on the structure and dynamics of water in single-walled carbon nanotubes". *Journal of Chemical Physics*, 125(11):114701, 2006.

Woodhouse, G., King, L., Wieczorek, L., Osman, P., and Cornell, B. "The ion channel switch biosensor". *Journal of Molecular Recognition*, 12(5):328–334, 1999.

Wu, Y., Wagner, L. K., and Aluru, N. R. "Hexagonal boron nitride and water interaction parameters". *Journal of Chemical Physics*, 144(16):164118, 2016.

Xu, P., Drewes, J. E., Kim, T. U., Bellona, C., and Amy, G. "Effect of membrane fouling on transport of organic contaminants in NF/RO membrane applications". *Journal of Membrane Science*, 279(1-2):165–175, 2006.

Yang, F. "Slip boundary condition for viscous flow over solid surfaces". *Chemical Engineering Communications*, 197(4):544–550, 2010.

Yang, Z., Ma, X. H., and Tang, C. Y. "Recent development of novel membranes for desalination". *Desalination*, 434:37–59, 2018.

Yu, Y., Lee, S., and Hong, S. "Effect of solution chemistry on organic fouling of reverse osmosis membranes in seawater desalination". *Journal of Membrane Science*, 351(1-2): 205–213, 2010.

Zhang, L., Jia, L., Zhang, J., Li, J., Liang, L., Kong, Z., Shen, J. W., Wang, X., Zhang, W., and Wang, H. "Understanding the effect of chemical modification on water desalination in boron nitride nanotubes via molecular dynamics simulation". *Desalination*, 464:84–93, 2019a.

Zhang, M., Guan, K., Ji, Y., Liu, G., Jin, W., and Xu, N. "Controllable ion transport by surface-charged graphene oxide membrane". *Nature Communications*, 10(1):1–8, 2019b.

Zhao, F., Zhang, Y., Chu, H., Jiang, S., Yu, Z., Wang, M., Zhou, X., and Zhao, J. "A uniform shearing vibration membrane system reducing membrane fouling in algae harvesting". *Journal of Cleaner Production*, 196:1026–1033, 2018.

Zhao, H., Qiu, S., Wu, L., Zhang, L., Chen, H., and Gao, C. "Improving the performance of polyamide reverse osmosis membrane by incorporation of modified multi-walled carbon nanotubes". *Journal of Membrane Science*, 450:249–256, 2014.

Zhao, S. and Zou, L. "Effects of working temperature on separation performance, membrane scaling and cleaning in forward osmosis desalination". *Desalination*, 278(1-3):157–164, 2011.

Zhao, S., Liao, Z., Fane, A., Li, J., Tang, C., Zheng, C., Lin, J., and Kong, L. "Engineering antifouling reverse osmosis membranes: A review". *Desalination*, 499:114857, 2021.

Zsirai, T., Qiblawey, H., Buzatu, P., Al-Marri, M., and Judd, S. J. "Cleaning of ceramic membranes for produced water filtration". *Journal of Petroleum Science and Engineering*, 166:283–289, 2018.